Bottle microresonators for applications in quantum optics and all-optical signal processing

Dissertation

zur Erlangung des Grades
„Doktor
der Naturwissenschaften"
am Fachbereich Physik, Mathematik und Informatik
der Johannes Gutenberg-Universität
in Mainz

Michael Pöllinger
geb. in Erding

Mainz, den 15. Dezember 2010.

Dekan: Prof. Dr. Manfred Lehn

1. Gutachter: Prof. Dr. Arno Rauschenbeutel
2. Gutachter: Prof. Dr. Jochen Walz
3. Gutachter: Prof. Dr. Oliver Benson

Tag der Promotion: 01.03.2011

D77

Für meine Familie, Nelly, Gerard, Maria und Christina

Para mi polola, Cristina

Zusammenfassung

Inhalt dieser Arbeit ist die Realisierung, Charakterisierung und Anwendung eines neuartigen Mikroresonators. Der sogenannte „Flaschenresonator" ist eine mikroskopische, monolithische Struktur aus Silikatglas. In ihm treten „Flüstergaleriemoden" auf, in denen Licht nahe der Oberfläche durch kontinuierliche Totalreflektion eingeschlossen wird. Dieses Einschlussprinzip ermöglicht extrem lange Speicherzeiten, erschweren aber im Gegenzug die Abstimmbarkeit der Resonanzfrequenz. Die ausgeprägte prolate Form des Flaschenresonators hingegen erlaubt flexible Kontrolle über die Modenstruktur und ermöglicht damit volle Durchstimmbarkeit – eine Grundvoraussetzung für Experimente zur „Resonator-Quantenelektrodynamik".

Kapitel I gibt einen kurzen Überblick über gebräuchliche Typen von Mikroresonatoren. Wichtige Größen, wie der Gütefaktor Q und das Modenvolumen V, die den zeitlichen und räumlichen Einschluss des Lichtfeldes beschreiben, werden hier eingeführt.

Kapitel II enthält eine theoretische Beschreibung der Lichtpropagation in Flaschenmoden und ultradünnen Glasfasern. Letztere ermöglichen die effiziente Einkopplung von Licht in Mikroresonatoren. Als wesentliche Ergebnisse erhält man die Intensitätsverteilung der Flaschenmoden, aus der sich das Modenvolumen berechnet. Das Kapitel schließt mit der Beschreibung des Herstellungsprozesses beider Strukturen.

In Kapitel III präsentiere ich experimentelle Ergebnisse zur hocheffizienten, nahezu verlustlosen Einkopplung von Licht in Flaschenmoden sowie deren räumliche und spektrale Charakterisierung. Es werden ultrahohe Gütefaktoren von 360 Millionen und vollständige Durchstimmbarkeit der Resonanzfrequenz demonstriert.

Kapitel IV untersucht die Eigenschaften eines Flaschenresonators in der sogenannten „add-drop filter" Konfiguration, in der zwei ultradünne Glasfasern an das Lichtfeld einer Flaschenmode gekoppelt sind. Diese Konfiguration ermöglicht einen resonanten Lichttransfer zwischen beiden Fasern mit einer Effizienz von über 90%. Des Weitern lässt sich in Flaschenresonatoren aufgrund des günstigen Verhältnisses von Absorption und nichtlinearem Brechungsindex optische Kerr-Bistabilität bei extrem kleinen Leistungen von etwa 50 μW beobachten. Dies erlaubt Signale zwischen den Ausgängen beider ultradünner Glasfasern zu dirigieren und zwar lediglich durch Variation der Eingangsleistung und ermöglicht damit Anwendungen im Bereich der optischen Signalverarbeitung.

Kapitel V diskutiert die Eignung von Flaschenresonatoren für Experimente zur Resonator-Quantenelektrodynamik mit einzelnen Atomen. Der hier realisiert Quotient Q/V, der dem maßgeblichen Verhältnis der Koppelrate zwischen Atom und Resonator zu den dissipativen Verlustraten der Subsysteme entspricht, ermöglicht eine Wechselwirkung von Atom und Resonator im Bereich der starken Kopplung. In Kombination mit der vollen Durchstimmbarkeit, und der hocheffizienten Faserkopplung stellt der Flaschenresonator somit ein einzigartiges Werkzeug zur Kopplung von Licht und Materie dar.

Resumen

En esta tesis se presentan la realización experimental, caracterización y aplicación de un nuevo tipo de microrresonador óptico. El llamado "microrresonador de botella" genera "modos de galería de susurros" (MGS). Así, en esta estructura microscópica de cuarzo, el campo electromagnético está confinado cerca de la superficie por reflexión total interna. En general, los microrresonadores basados en MGSs poseen unas propiedades excelentes con respecto al confinamiento espacial y temporal de la luz. Sin embargo, la estructura monolítica del microrresonador hace complicado el ajuste de su frequencia de resonancia. Esto dificulta su uso, por ejemplo, en experimentos de electrodinámica cuántica de cavidades (EDCC), donde se investiga la interacción de un emisor cuántico de frequencia de resonancia predeterminada con un modo del microrresonador. Por el contrario, la forma elongada del microrresonador de botella produce una estructura de los modos ajustable y por tanto permite el ajuste ilimitado de cualquier frequencia de resonancia.

En el capítulo I, presento una idea general sobre los distintos tipos de microrresonadores ópticos. Introduzco parámetros importantes como el factor de calidad Q y el volumen de los modos V, que caracterizan el encerramiento temporal y espacial de la luz respectivamente.

El capítulo II se dedica a una descripción teórica de la propagación de la luz en microrresonadores de botella basada en las ecuaciones de Maxwell. Se calcula la distribución de la intensidad de la luz dentro del microrresonador. Además, hago una breve descripción de la propagación de la luz en fibras ópticas de diámetros comparables a la longitud de onda óptica. Estas fibras ultrafinas se utilizan para acoplar la luz en el microrresonador de botella. Finalmente, describo la fabricación de ambas estructuras.

En el capitulo III presento resultados experimentales del acoplamiento de la luz en microrresonadores de botella con una eficiencia muy alta. Además investigo las propiedades espaciales y espectrales de los modos. Demuestro factores de calidad que exceden los 360 millones así como la posibilidad de ajuste de cualquier frequencia de resonancia predeterminada.

En el capítulo IV se describen los experimentos en los que el microrresonador de botella es utlizado en la llamada "configuración add-drop" (inserción-extracción), para la cual dos fibras ultrafinas se acoplan a un modo del microrresonador. El acople de la luz de eficiencia alta junto con el elevado factor de calidad, permiten la transferencia resonante de la potencia óptica entre las dos fibras con una eficacia de más de un 90 por ciento. Además la ratio favorable de la absorción al índice de refracción no lineal de cuarzo, hace posible la observación de biestabilidad óptica causado por efecto Kerr a potencias ópticas muy bajas del orden de 50 μW. En combinación con la configuración add-drop, abre la posibilidad de dirigir señales ópticas entre las dos salidas de las fibras ultrafinas variando simplemente la potencia óptica. De esta manera se facilita la aplicación en el área de procesamiento de señales ópticas.

Finalmente, el capítulo V, discute el potencial de los microrresonadores de botella para experimentos EDCC con átomos individuales. Su ratio Q/V, que determina la relación entre el acoplo átomo-modo y las tasas de disipación de los subsistemas, es comparable

a los valores obtenidos con los mejores microrresonadores optimizados tecnológicamente para experimentos para EDCC. Además, las posibilidades de ajustar la frequencia de resonancia a un valor arbitrario y de acoplar y extraer la luz de los modos del microrresonador con una eficiencia alta, convierten al microrresonador de botella en una herramienta única para aplicaciones en el área de la óptica cuántica.

Abstract

This thesis reports on the experimental realization, characterization and application of a novel microresonator design. The so-called "bottle microresonator" sustains whispering-gallery modes in which light fields are confined near the surface of the micron-sized silica structure by continuous total internal reflection. While whispering-gallery mode resonators in general exhibit outstanding properties in terms of both temporal and spatial confinement of light fields, their monolithic design makes tuning of their resonance frequency difficult. This impedes their use, e.g., in cavity quantum electrodynamics (CQED) experiments, which investigate the interaction of single quantum mechanical emitters of predetermined resonance frequency with a cavity mode. In contrast, the highly prolate shape of the bottle microresonators gives rise to a customizable mode structure, enabling full tunability. The thesis is organized as follows:

In chapter I, I give a brief overview of different types of optical microresonators. Important quantities, such as the quality factor Q and the mode volume V, which characterize the temporal and spatial confinement of the light field are introduced.

In chapter II, a wave equation calculation of the modes of a bottle microresonator is presented. The intensity distribution of different bottle modes is derived and their mode volume is calculated. A brief description of light propagation in ultra-thin optical fibers, which are used to couple light into and out of bottle modes, is given as well. The chapter concludes with a presentation of the fabrication techniques of both structures.

Chapter III presents experimental results on highly efficient, nearly lossless coupling of light into bottle modes as well as their spatial and spectral characterization. Ultra-high intrinsic quality factors exceeding 360 million as well as full tunability are demonstrated.

In chapter IV, the bottle microresonator in add-drop configuration, i.e., with two ultra-thin fibers coupled to one bottle mode, is discussed. The highly efficient, nearly lossless coupling characteristics of each fiber combined with the resonator's high intrinsic quality factor, enable resonant power transfers between both fibers with efficiencies exceeding 90%. Moreover, the favorable ratio of absorption and the nonlinear refractive index of silica yields optical Kerr bistability at record low powers on the order of 50 μW. Combined with the add-drop configuration, this allows one to route optical signals between the outputs of both ultra-thin fibers, simply by varying the input power, thereby enabling applications in all-optical signal processing.

Finally, in chapter V, I discuss the potential of the bottle microresonator for CQED experiments with single atoms. Its Q/V-ratio, which determines the ratio of the atom-cavity coupling rate to the dissipative rates of the subsystems, aligns with the values obtained for state-of-the-art CQED microresonators. In combination with its full tunability and the possibility of highly efficient light transfer to and from the bottle mode, this makes the bottle microresonator a unique tool for quantum optics applications.

Publications

Parts of this thesis have been published in the following reviewed journal articles:

1. M. Pöllinger, D. O'Shea, F. Warken and A. Rauschenbeutel,
   "Ultrahigh-Q Tunable Whispering-Gallery-Mode Microresonator,"
   Physical Review Letters **103,** 053901 (2009).

2. M. Pöllinger and A. Rauschenbeutel,
   "All-optical signal processing at ultra-low powers in bottle microresonators using the Kerr effect,"
   Optics Express, Vol. **18,** 17764 (2010).

Contents

Contents

Introduction

Optical microresonators hold great potential for many fields of research and technology [Vah03]. They are used for filters and switches in optical communications [Chu99, Djo02, Alm04b], bio(chemical) sensing [Arm07], microlasers [San96, Kli00, Cai00a], as well as for cavity quantum electrodynamics applications such as single-photon sources [Mic00, McK04, Hij07] and interfaces for quantum communication [Boo07, Wil07]. All these applications rely on the spatial and temporal confinement of light by the microresonator. More quantitatively, these light-confining properties are characterized by the resonator's mode volume V and its quality factor Q. For a given in-coupled power, the resulting intra-cavity intensity is then proportional to the ratio of Q/V. This ratio also defines a key figure relating the coupling strength between light and matter in the resonator to the dissipation rates of the coupled system. The highest values of Q/V to date have been reached with whispering-gallery mode (WGM) microresonators [Kip04a]. WGM microresonators are monolithic, micron-sized, dielectric structures in which the light is guided near the surface by continuous total internal reflection [Mat06]. This extremely lossless mechanism of confinement enables their ultra-high quality factors exceeding 10^8. Standard WGM microresonators, like dielectric microspheres, microdisks, and microtoroidal resonators, typically confine the light in a narrow ring along the equator of the structure by continuous total internal reflection at the resonator surface [Mat06]. While such equatorial WGMs have the advantage of a small mode volume they also exhibit a large frequency spacing between consecutive modes, which scales inversely with the resonator diameter. In conjunction with the limited tuning range due to their monolithic design, tuning of modes which combine ultra-high quality factors and small mode volumes in equatorial WGM microresonators to an arbitrary frequency has therefore not been realized to date. This impedes their use in a large class of applications which require a resonance of the microcavity to coincide with a predetermined frequency. For this reason, the WGM "bottle microresonator" has recently received considerable attention [Kak01, War06, War08, Str08] because it promises a customizable mode structure while maintaining a favorable Q/V-ratio [Sum04, Lou05]. In this work highly prolate shaped bottle microresonators are fabricated from standard optical glass fibers. As I will show in the following, these devices combine an ultra-high quality factor of 360 million, a small mode volume, and nearly lossless fiber coupling, characteristic of whispering-gallery mode resonators, with a simple and customizable mode structure enabling full tunability, which makes them ideal candidates for CQED experiments.

Due to the strong enhancement of the intracavity intensity, microresonators are often used for non-linear optics applications. As an example they are employed for third harmonic generation [Car07] and the creation of frequency combs [Hay07]. Moreover, they are very interesting in the field of "all-optical switching", i.e., the control or redirection of the flow of light using a second light field . If the resonator material exhibits a third-order susceptibility $\chi^{(3)}$, its refractive index n depends on the intracavity intensity via the Kerr effect $n = n_1 + n_2 \times I$, where n_1 is the linear refractive index, $n_2 \propto \chi^{(3)}$ is the nonlinear refractive index, and I is the intensity of the light field. A variation of the intra-cavity intensity then modifies the cavity's optical path length

and thus changes the transmission properties of the microresonator. In this work, I present all optical switching via the Kerr effect at record-low powers using bottle microresonators. [Sum04,Lou05,Mur09,Poe09]. For a given input power, the nonlinear shift of the resonance frequency in units of the resonator linewidth is proportional to $n_2 Q^2/V$. The bottle microresonator combines ultra-high quality factors of up to $Q > 10^8$ with mode volumes in the range of 1000 μm^3. The resulting Q^2/V-ratio is among the highest realized for optical microresonators and allows us to observe bistable behavior at very low powers. Single-wavelength all-optical switching via the Kerr effect at a record-low threshold of 50 μW is demonstrated. In addition, using the evanescent field of sub-micron diameter tapered fiber couplers, the bottle microresonator allows one to couple light into and out of its modes with high efficiency by frustrated total internal reflection [Kni97,Cai00b,Spi03]. Finally, the mode geometry offers simultaneous access to the resonator's light field with two coupling fibers without the spatial constraints inherent to equatorial WGMs typically employed in microspheres and microtoroidal resonators. This facilitates the use of the bottle microresonator as a four-port device in a so-called "add-drop configuration". In combination with the bottle microresonator's nonlinear properties a CW optical signal can therefore be routed between both fiber outputs with high efficiency by varying its power level.

1 Basics – optical microresonators

In the following, a brief overview of common microresonator designs and their applications is given. Moreover, the novel concept of the "bottle microresonator", which is subject of this work, is presented.

1.1 Fabry-Pérot microresonators

A typical Fabry-Pérot (FP) microresonator (also, microcavity) consists of two millimeter-sized mirrors with a separation of $L = 10 - 160$ μm [Hoo00, Khu08]. The light field of the cavity is described by an Gaussian standing wave profile as shown in Fig. 1.1. The divergence of the Gaussian mode can be neglected because the mirror spacing is usually much smaller than their radius of curvature. For the fundamental TEM_{00} mode the intracavity intensity is then given by

$$I(r, z) = I_0 \exp\left(-2r^2/w_0^2\right) \sin\left(2\pi z/\lambda\right)^2 \ , \tag{1.1}$$

where w_0 is the waist diameter, z is the cavity axis, defined by the direction of light propagation, r is the radial coordinate, perpendicular to z, and I_0 is the maximum intensity for $r = 0$. In order to obtain small mode volumes, the curvature of the mirrors is chosen to obtain a waist diameter of few tens of microns. However, the maximum curvature is limited by spatial constraints. The mode volume V for a given set of cavity
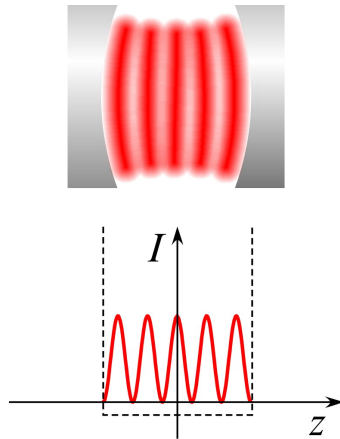

Figure 1.1: Basic principle of a Fabry-Pérot resonator consisting of two highly reflecting mirrors. The cavity mode is a Gaussian beam exhibiting a standing wave structure.

parameters is calculated by integration over the resonator's intensity distribution

$$V = \int_{\mathbb{R}^3} n^2 (\vec{r}) \frac{I(\vec{r})}{I_{\max}} dr^3 \ , \tag{1.2}$$

where $n(\vec{r})$ is the refractive index. The intensity distribution is normalized to unity by dividing by its maximum value $I_{\max}$ in order to make the mode volume independent of the power coupled into the cavity. For the intensity distribution given above, and neglecting the propagating light fields outside the cavity caused by the finite reflectivity of the cavity mirrors, this formula yields $V = \pi w_0^2 L/4$. The mirror's multi-layer dielectric coatings have a transmission t in the ppm range in order to enable a maximum storage time of the light. Losses result from leakage of photons from the cavity due to the finite reflectivity r of the coatings as well as from absorption and scattering losses a (the coefficients t, r and a describe the change in intensity due to transmission, reflection and absorption by the cavity's mirrors). Therefore, in the absence of a driving light field, the intracavity energy W decays exponentially with a time constant τ. The first loss mechanism enables coupling of propagating light fields to the cavity mode and is therefore inevitable. The latter are referred to as intrinsic losses resulting from imperfections in the resonator material and fabrication. The temporal confinement can be quantitatively described by the storage time τ in units of the optical period $T = \nu_0^{-1}$, with the optical resonance frequency ν_0. It is convenient to use the "so-called" quality factor Q which is defined as

$$Q = 2\pi \frac{\tau}{T} \ . \tag{1.3}$$

Using the angular resonance frequency $\omega_0 = 2\pi\nu_0$, the quality factor writes as $Q = \omega_0\tau$. In order to characterize both the spatial and temporal confinement of the intracavity light field, the ratio Q/V is used. This ratio determines the enhancement of the intracavity intensity for a given input power P_{in} and thus is an important figure of merit for optical microresonators. Since in Fabry Pérot resonators, unlike as in monolithic resonators, the losses almost exclusively occur at each reflection, it is convenient to characterize these devices by the cavity's finesse $\mathcal{F}$, which is related to the number of round trips N of the light within the storage time τ by

$$\mathcal{F} = 2\pi N \ . \tag{1.4}$$

Optical power can only be efficiently coupled into the cavity if the incident light field constructively interferes with the intra-cavity field. This condition is fulfilled only for distinct wave numbers $k = 2\pi/\lambda$, for which the cavity round trip phase δ is an integer multiple i of 2π. The transmitted power P_{tr}, which is proportional to the intracavity intensity, is then given by an Airy function [Mes04]

$$P_{\text{tr}} = \frac{4t^2(1-a)}{(2t+a)^2} \frac{P_{\text{in}}}{1 + F_A \sin^2(\delta/2)} \ , \tag{1.5}$$

with the generalized finesse coefficient $F_A = 4r\sqrt{1-a}/(1-r\sqrt{1-a})^2$. Figure 1.2 shows P_{tr} as a function of the optical frequency of the input wave. The frequency spacing
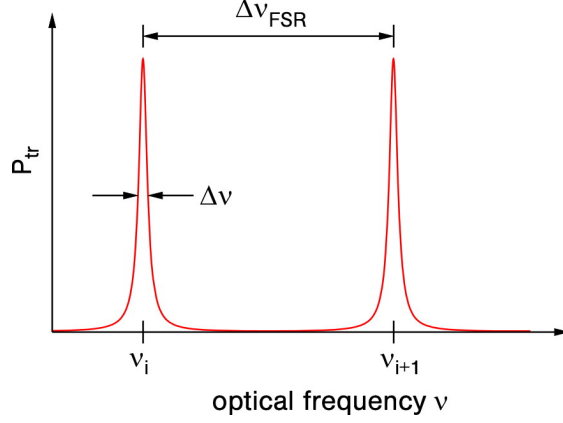
Figure 1.2: Mode spectrum of a Fabry-Pérot resonator. The power transmitted through the cavity P_{tr} as a function of the optical frequency of the input light field is given by an Airy function. The signal transmitted through the cavity is proportional to the intracavity intensity. The individual peaks of FWHM $\Delta\nu$, corresponding to the modes of the resonator, are separated by the free spectral range $\Delta\nu_{FSR}$.

between adjacent modes of orders i and $i+1$, is called free spectral range $\Delta\nu_{\mathrm{FSR}} = \nu_{i+1} - \nu_i$. The FWHM of the resonances is denoted by $\Delta\nu$. It can be shown that the finesse is given by the ratio of both quantities [Mes04]

$$\mathcal{F} = \frac{\Delta\nu_{\mathrm{FSR}}}{\Delta\nu} \ . \tag{1.6}$$

As a consequence, the quality factor can be expressed as the ratio of linewidth to optical frequency of the resonance ν_0

$$Q = \frac{\nu_0}{\Delta\nu} \ . \tag{1.7}$$

The transmission through the cavity, determined by the intrinsic losses rate a, on resonance reaches a maximum value of $T = P_{\mathrm{tr}}/P_{\mathrm{in}} = 4t^2(1-a)/(2t+a)^2 \approx t^2/(t+a)^2$ [Dot07].

FP cavities have been intensively used in the field of cavity quantum electrodynamics, in which they enable to observe the interaction between a single atom and the cavity light field deep within the so-called strong coupling regime. Here, the coupling rate g, which describes the energy transfer between the cavity light field and the atom, clearly exceeds the dissipation rates of the system, given by the cavity field decay rate $\kappa = \omega_0/(2Q)$ and the transverse atomic dipole decay rate $\gamma_\perp$, caused by spontaneous emission. The figure of merit for CQED experiments in the regime of strong coupling is $g^2/(\kappa\gamma_\perp) \propto Q/V$ [Rem95, Mab96, Boc04].

1.2 Whispering-gallery mode resonators

Light confinement in WGM resonators is based on total internal reflection. Moreover, frustrated total internal reflection enables efficient coupling of propagating light field to

WGMs. Therefore these phenomena will be reviewed in detail, followed by an overview of different realizations of WGM resonators, including the bottle microresonator.

1.2.1 Total internal reflection

The refraction of an electromagnetic wave, propagating in a medium of refractive index n_1 at an interface with another medium of refractive index n_2 is described by Snell's law [Hec89]

$$n_1 \sin(\Theta_1) = n_2 \sin(\Theta_2) \ , \tag{1.8}$$

where Θ_1, Θ_2 are the angles between the wave vectors $\vec{k}_1$ and $\vec{k}_2$ of the incident and refracted light fields and the surface's normal vector, as illustrated in Fig. 1.3 (a). At an interface between an optically dense medium and an optically thinner medium, i.e., for $n_2 < n_1$, a reflected wave only exists for angles Θ_1 smaller than the critical angle $\Theta_c = \sin^{-1}(n_2/n_1)$. Otherwise, the incident wave is totally reflected from the interface, as shown in Fig. 1.3 (b) At a glass–air interface with $\Delta n \approx 0.5$ the critical angle is $42°$. In the following, the electromagnetic field in the optically thinner medium in the case of total internal reflection will be examined in detail, following the analysis in [Hec89, Mes04]. In the following, the electric field in the optically thinner medium is treated as a scalar field of the form

$$E_2 = E_{02} \exp\left(i\left(\vec{k}_2 \cdot \vec{r} - \omega t\right)\right) \ . \tag{1.9}$$

The wave vector $\vec{k}_2$ with an absolute value of $|\vec{k}_2| = n_2 2\pi/\lambda_0$ can be split in a component k_x that describes the propagation along the interface and a component k_y describing the propagation normal to the interface. Using Snell's law one finds a relation for $k_y = k_2 \cos(\Theta_2)$

$$k_y = k_2 \left(1 - \frac{n_1^2 \sin^2(\Theta_1)}{n_2^2}\right)^{1/2} \ . \tag{1.10}$$
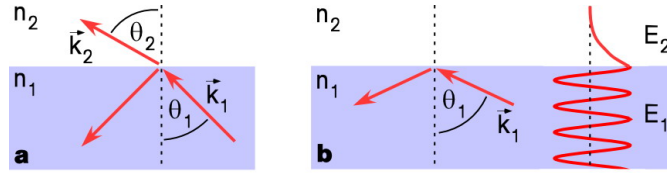
Figure 1.3: (a) Reflection and refraction at an interface between two media with refractive indices n_1 and n_2. The wave vector of the incident wave and the refracted wave are denoted by $\vec{k}_1$ and $\vec{k}_2$, respectively. The relation between their angles with the normal vector of the interface, Θ_1 and Θ_2, is described by Snell's law. (b) For $n_2 < n_1$ and angles larger than the critical angle Θ_c the light field is completely reflected by the interface. A detailed analysis shows that the electromagnetic field decays exponentially beyond the interface. The penetration depth of this evanescent field into the optically thinner medium is typically on the order of the wavelength.

If $\sin(\Theta_1) > n_2/n_1$,

$$k_y = ik_2 \left(\frac{n_1^2 \sin^2(\Theta_1)}{n_2^2} - 1 \right)^{1/2} = i\beta \tag{1.11}$$

becomes complex, while $k_x = (n_1 k_2/n_2) \sin(\Theta_1)$ is real. The electric field strength in the optically thinner medium is given by

$$E_2 = E_{02} \exp(-\beta y) \exp i(k_x x - \omega t) \ . \tag{1.12}$$

This so-called "evanescent field" exponentially decays with increasing distance y from the interface. Its penetration depth

$$\frac{1}{\beta} = \frac{\lambda_0}{2\pi \sqrt{n_1^2 \sin^2(\Theta_1) - n_2^2}} \tag{1.13}$$

is typically on the order of the wavelength. The normal component of the pointing vector that describes the transport of energy by the electric field is purely imaginary. A second interface, located within the penetration depth of the evanescent field, gives rise to a propagating light field beyond the second interface. This phenomenon, called "frustrated total internal reflection", is used in beam splitters, in which two glass substrates are separated by a defined air gap. A wave hitting the interface at an angle of $45°$ is partially transmitted due to frustrated total internal reflection. The ratio of the optical power coupled to the second substrate and thus transmitted through the beam splitter can be adjusted by varying the width of the gap. The phenomenon of frustrated total internal reflection can also be employed for coupling light to WGMs of monolithic microresonators. In prism coupling [Bra89] the evanescent field created by total internal reflection in the prism is spatially overlapped with the evanescent field of a WGM. The distance has to be chosen on the order of the penetration depth, which, e.g., for a prism with $n = 1.5$ and $\Theta = 45°$ is $1/\beta = 380$ nm. By choosing an appropriate refractive index of the prism and reflection angle, the wave vectors of the WGM and the incident light field can be matched resulting in efficient coupling of optical power to the WGM. Other approaches for coupling light to WGMs use the evanescent fields of side-polished optical fibers [Dub95] and of ultra-thin tapered optical fibers [Kni97].

1.2.2 Microspheres and microtoroidal resonators

The first monolithic microresonators based on WGMs were realized by melting the tip of a silica fiber [Bra89]. The molten glass forms a sphere due to surface tension. The spherical shape and a surface with minimal roughness are maintained after solidification. In large microspheres with diameters of several $100 \ \mu$m, quality factors among the highest ever realized with optical microresonators were measured, only limited by the residual absorption of silica. For example, a sphere $750 \ \mu$m in diameter, yielded a loaded quality factor of 8×10^9 at a wavelength of 633 nm [Gor96]. However, an optimal Q/V-ratio is achieved for resonators with much smaller radii in the range of some tens of micrometers [Buc03, Kip04a]. Such resonators exhibit a more pronounced evanescent field, related

to the stronger curvature of the resonator surface. This leads to a strong intensity enhancement at the surface of the resonator, providing excellent accessibility, but also induces surface-related losses. The resonator radius can be decreased to around 15 μm while maintaining quality factors in the $10^8 - 10^9$ range. Quality factors $Q \geq 10^8$ are referred to as ultra-high quality factors (UHQ). For a given radius of the resonator, the mode volume can be further decreased by changing the shape of the structure. In a toroidal structure the mode is further compressed in the polar direction [Spi05]. Microtoroidal resonators are produced in two steps from a silicon substrate with a silica layer of several μm thickness. First, a disc-shaped silica structure with a massive silicon stem is created by lithography and etching. Next, the structure is heated with a CO_2 laser. Due to the relatively high thermal conductivity of silicon, only the edges of the silica disc that are not in contact with the silicon stem are molten and form a toroidal structure [Arm03]. In this type of resonator some of the highest values of Q/V have been reached to date [Kip04a].

1.2.3 Bottle microresonators

The WGM resonator concepts described above typically employ modes in which the light field propagates along the equator of the structure. While these equatorial WGMs, have the advantage of a small mode volume they also exhibit a large frequency spacing between consecutive modes, which scales inversely with the resonator diameter. In conjunction with the limited tuning range due to their monolithic design, tuning of modes which combine ultra-high quality factors and small mode volumes in equatorial WGM microresonators to an arbitrary frequency has therefore not been realized to date. For this reason, the novel concept of a WGM "bottle microresonator" has recently received considerable attention [Kak01, War06, War08, Str08, Mur09] because it promises a customizable mode structure while maintaining a favorable Q/V-ratio [Sum04, Lou05]. Due to its highly prolate shape, the bottle microresonator gives rise to a class of whispering-gallery modes (WGMs) with advantageous properties, see Fig. 1.4. The parabolic radius profile of the bottle resonator $R(z) = R_0 \cdot \left(1 - 1/2\left(\Delta k \cdot z\right)^2\right)$ causes a harmonic effective potential for the light field along the resonator axis. The light in these "bottle modes" harmonically oscillates back and forth along the resonator axis between two turning points which are defined by an angular momentum barrier [Lou05]. The resulting axial standing wave structure exhibits a significantly enhanced intensity at the so-called "caustics" of the bottle mode, located at the turning points of the harmonic motion. The caustics therefore form two well separated coupling ports for coupling light or matter to the bottle mode. Moreover, the bottle microresonator possesses an equidistant spectrum of eigenmodes, labelled by the "azimuthal quantum number" m, which counts the number of wavelengths that fit into the circumference of the resonator, and the "axial quantum number" q, which counts the number of axial intensity nodes [Sum04, Lou05]. The frequency spacing between modes with consecutive quantum numbers q (m) is called the axial (azimuthal) free spectral range and will be denoted $\Delta\nu_q$ $(\Delta\nu_m)$ in the following. As in equatorial resonators, the azimuthal free spectral range is fixed by the resonator radius. However, the axial mode spacing only depends on the curvature of
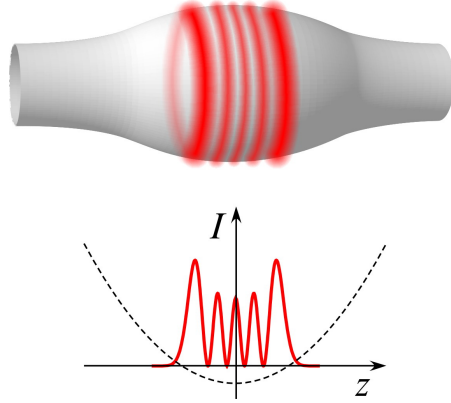
Figure 1.4: Concept of the bottle microresonator. In addition to the radial confinement by continuous total internal reflection at the resonator surface, the axial confinement of the light is caused by a harmonic effective potential (dashed line) fixed by the curvature of the resonator profile. The resulting intensity distribution is therefore given by the eigenfunctions of the quantum mechanical harmonic oscillator [Lou05].

the resonator profile and can thus be made much smaller than $\Delta\nu_m$ without significantly affecting the resonator's mode volume. This should enable tuning of the bottle microresonator by one azimuthal free spectral range which enables coupling of any arbitrary frequency to the resonator [Lou05]. Up to now, few groups realized bottle microresonators [Kak01, War06, Poe06, War07, Mur09], but neither quality factors exceeding 5×10^5 nor fully tunability has experimentally been demonstrated.

1.3 Photonic crystal microresonators

A completely different approach is chosen in photonic crystal microresonators. In photonic crystals light confinement is achieved by a spatially periodic modulation of the refractive index. One distinguishes between one-, two- and three-dimensional photonic crystals, depending on the dimensionality of the periodic structure. For one- and two-dimensional photonic crystals the light confinement in the remaining dimension(s) is achieved by employing the structure that bears the periodic pattern as a waveguide, in which the light is guided by total internal reflection at its surface. One-dimensional photonic crystals are well known from dielectric Bragg mirrors, which consist of multiple layers with a thickness of $\lambda/4$ and alternating refractive index. In a certain frequency band the light is reflected form such a dielectric stack. In a "micropost" cavity, two highly reflective dielectric mirrors separated by a spacer with a thickness of usually $\lambda/2$ form a Fabry-Pérot like cavity with a mode volume on the order of some $(\lambda/n)^3$. The interface of the cylindric post like structure guides the light field by total internal reflection in the region between the Bragg mirrors. As an example, in [Ger98] such a cavity with a mode volume of $5(\lambda/n)^3$ and a quality factor of 5000 was demonstrated. Further expanding the dimensionality of the periodic structure to two dimensions yields even smaller mode volumes. A possible realization is a periodic lattice of air holes etched in

a thin semiconductor slab. A line defect in such a lattice forms a waveguide. A point defect, realized by leaving one hole unetched creates a cavity. The light is then confined in the lattice plane by Bragg reflection and in the third dimension by total internal reflection at the silicon air interface. The fist realizations of those structures yielded quality factors many orders of magnitude below the theoretically predicted limit. Nevertheless, these cavities have steadily been improved. Recently, a photonic crystal cavity with a mode volume as small as $V = 1.7 \ (\lambda/n)^3$ and a quality factor of $Q = 1.3 \times 10^6$ has been demonstrated [Tan07]. The resulting Q/V value is comparable to those observed in microtoroidal resonators. Photonic crystal cavities have been employed for low-threshold lasers [Pai99]. Since they consist of semiconductors, single quantum dot emitters are readily incorporated in the cavity, enabling applications like strong coupling between a quantum dot and the cavity mode [Yos04] and single-photon sources [Pel02].

2 Fundamental properties and fabrication of bottle resonators and ultra-thin optical fibers

This chapter presents a theoretical model of light propagation in bottle modes and ultra-thin optical fibers, followed by a description of the fabrication process of both structures. First, a wave equation calculation [Lou05] on bottle modes is presented. From this model, their spatial and spectral properties are derived. In particular, the intensity distribution and the corresponding mode volume is calculated. Exact knowledge of the latter is of great importance for optimizing the ratio of Q/V. Next, light propagation in optical step-index fibers as well as in ultra-thin optical fibers is discussed. This section will only give a brief overview which is limited to the properties relevant for the understanding of the ultra-thin fiber coupler that is used for excitation of bottle modes. A detailed analysis can be found in [Yar91]. Bottle microresonators and ultra-thin optical fibers are fabricated using a custom built "fiber pulling rig" [War07]. The last section gives a brief description of the fabrication techniques developed in [Poe06, War07].

2.1 Calculations on bottle modes

2.1.1 Wave equation for bottle microresonators

In [Lou05] the wave equation for a bottle resonator is established and solved for its eigenfunctions. An approximately parabolic profile

$$R(z) \approx R_0 \cdot \left(1 - 1/2 \left(\Delta k \cdot z \right)^2 \right). \tag{2.1}$$

of the resonator radius R along the resonator axis z is assumed as illustrated in Fig. 2.1 (a). Here, R_0 is the maximum radius of the resonator at the position $z = 0$ and Δk denotes the curvature of the resonator profile. The electric and magnetic fields of a bottle mode have to fulfill the Helmholtz equation

$$\left(\nabla^2 + k^2 \right) \cdot \vec{E} = 0 , \tag{2.2}$$

$$\left(\nabla^2 + k^2 \right) \cdot \vec{H} = 0 ,$$

where ∇^2 is the Laplace operator and $k = \omega \cdot n/c = 2\pi n/\lambda_0$ is the wave number of the electromagnetic field with angular frequency ω and the vacuum wavelength λ_0, propagating in a medium with refractive index n. The refractive index of silica is $n_{\mathrm{Si}} =$
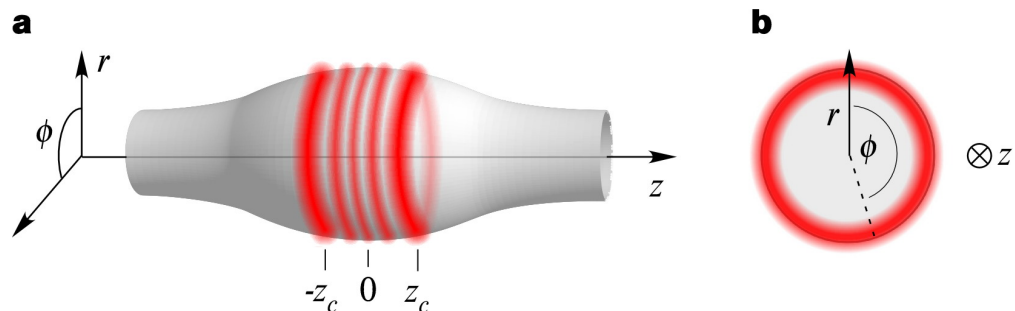
Figure 2.1: Sketch of the resonator geometry along (a) and in a plane perpendicular (b) to the resonator axis. The Helmholtz equation is solved in cylindrical coordinates. (b) The azimuthal coordinate is denoted by ϕ. (a) The radial coordinate and the axial coordinate are denoted by r and z, respectively. A slowly varying parabolic profile of the resonator radius along the z axis is assumed (see Eq. (2.1)). The radial and axial (indicated in red) intensity distribution of the modes is derived. Each bottle mode is located between two caustics at $\pm z_c$. The caustic radius R_c can be understood as a cutoff for propagation along z due to the angular momentum of the bottle mode.

1.467 for a wavelength around $\lambda_0 = 852$ nm (in the experiments presented in this thesis, a diode laser with a wavelength around $\lambda_0 = 852$ is used to excite bottle modes). The speed of light in a vacuum is denoted by c. In cylindrical coordinates (z: axial coordinate, r: radial coordinate, ϕ: azimuthal coordinate) the Laplace operator has the following form

$$\nabla^2 = \frac{1}{r}\partial_r + \partial_r^2 + \frac{1}{r^2}\partial_\phi^2 + \partial_z^2 \ . \tag{2.3}$$

Separation of the wave equation

In [Lou05] the method of adiabatic invariants, well known from the description of charged particles in magnetic bottles, is used to separate the wave equation. Due to the prolate shape of the bottle resonator, there is only a small variation in its radius along z, meaning that $dR/dz \ll 1$ in the central region of the structure. The radial component of the wave vector is given by $k_r = (dR/dz) \cdot k_z$. The resonators used in this work have a diameter $D_0 = 2R_0$ of around 35 μm and a typical curvature of $\Delta k = 0.012$ μm^{-1}. The bottle modes experimentally investigated are located in a region $|z| \leq 10$ μm. With these values one finds $|k_r(z)| \leq 2.5 \times 10^{-2} |k_z(z)|$. The z-component of the wave vector vanishes at the caustics and gets maximal for $z = 0$. Its maximum value depends on the spacing of the caustics. The caustic positions considered here, $|z_c| \leq 10$ μm, ensure that $k_\phi \gg k_z$. This means that the radial component of the wave vector can be neglected with respect to the axial and azimuthal components k_z and k_ϕ.

$$k \approx \sqrt{k_z^2 + k_\phi^2} \ . \tag{2.4}$$

Due to the cylindrical symmetry, the projection of the angular momentum on the z axis is conserved $\partial_z k_\phi(z) R(z) = 0$. Moreover, the value of k_z vanishes at the resonator

caustics with radius R_c, meaning that $k_\phi(\pm z_c) = k$. Thus the axial dependency of k_ϕ is given by

$$k_\phi(z) = k \cdot R_c/R(z) \ . \tag{2.5}$$

Due to the cylinder symmetry, the azimuthal part of the wave function is given by $\exp^{im\phi}$, with integer $m \in \mathbb{Z} - \{0\}$ being the azimuthal quantum number. The z-component of the angular momentum of a bottle mode is then given by $L_z = m\hbar$. Furthermore, motivated by the adiabatic approximation, the wave function is written as a product of the "axial wave function" $Z(z)$ and the "radial wave function" $\vec{\Phi}(r, R(z))$. The latter only exhibits a "weak" z dependency via the adiabatic variation of the resonator radius. The wave equation thus reads

$$\left(\nabla^2 + k^2\right) \cdot \vec{\Phi}(r, R(z)) \, Z(z) \, e^{im\phi} = 0 \ . \tag{2.6}$$

By using the approximation $\partial_z^2 \Phi_i = 0$ one obtains equations for all three components i of the wave function

$$-\frac{1}{Z(z)} \cdot \partial_z^2 Z(z) \ - k_z(z)^2 = \frac{1}{\Phi_i(r, R(z))} \cdot \left(\frac{1}{r}\partial_r \Phi_i(r, R(z)) + \partial_r^2 \Phi_i(r, R(z))\right) \\ -\frac{m^2}{r^2} \ + k_\phi(R(z))^2 \ . \tag{2.7}$$

Neglecting the weak z dependency on the left-hand side, the wave equation separates into two parts. The "radial wave equation" thus reads

$$\partial_r^2 \Phi_i(r, R(z)) + \frac{1}{r}\partial_r \Phi_i(r, R(z)) + \left(k_\phi^2(R(z)) - \frac{m^2}{r^2}\right)\Phi_i = 0 \ . \tag{2.8}$$

It depends on the radial coordinate and contains $R(z)$ and m as parameters. It has the form of a Bessel equation, well known from the description of light propagation in optical fibers [Yar91]. The "axial wave equation" only depends on the z coordinate

$$\left(\partial_z^2 + k_z^2\right) \cdot Z(z) = 0 \ . \tag{2.9}$$

In the following, both equations are solved.

2.1.2 Solving the radial wave equation

In order to derive the electric and magnetic fields propagating in structures with cylindrical symmetry, it is a common strategy to solve for the z- components of the fields [Yar91] and to derive the other components using Maxwell's equations. From Maxwell's curl equation one obtains the following set of equations when neglecting all z derivatives

$$\begin{aligned} E_r &= \frac{-i}{\epsilon\omega}\frac{1}{r}\partial_\phi H_z \ , \\ E_\phi &= \frac{i}{\epsilon\omega}\partial_r H_z \ , \\ H_r &= \frac{i}{\mu\omega}\frac{1}{r}\partial_\phi E_z \ , \\ H_\phi &= \frac{-i}{\mu\omega}\partial_r E_z \ , \end{aligned} \tag{2.10}$$

13

with the electric and magnetic permeabilities of the media $\epsilon = \epsilon_r \cdot \epsilon_0$ and $\mu = \mu_r \cdot \mu_0$, where ϵ_0 and μ_0 are the vacuum permeabilities and ϵ_r and μ_r are the relative permeabilities. For silica $\mu_r = 1$ and $\epsilon_r = n^2$. Due to the adiabatic change in the resonator radius along z, this attempt also applies to bottle modes in close approximation.

In order to solve the radial wave equation for the z-components of the fields, one uses the well known solution of the Bessel differential equation

$$x^2 \partial_x^2 y + x \partial_x y + (x^2 - n^2)y = 0 \ . \tag{2.11}$$

For a fixed value of n there are two linearly independent solutions. The Bessel function of the first kind $J_n(x)$ and the Bessel function of the second kind $Y_n(x)$. By identifying $y = \Phi_i$, $x = k_\phi(z) \cdot r$ and $n = m$, the general solution for $\Phi_i(r, z)$ is then given by the following linear combination

$$\Phi_i(r, z) = A \cdot J_m\left(k_\phi(z) \cdot r\right) + B \cdot Y_m\left(k_\phi(z) \cdot r\right) \ . \tag{2.12}$$

However, the fact that physical fields of confined modes have to be derived sets some restrictions to the solutions. From the asymptotic behavior of the Bessel functions, as well as from their behavior near the resonator surface it can be shown that the wave functions describing E_z and H_z have to be of the form [War07]

$$E_z(r, z) \propto A \cdot J_m\left(\frac{k_0 n R_c}{R(z)} \cdot r\right) \ , \qquad \text{for } r \leq R(z) \ . \tag{2.13}$$

$$E_z(r, z) \propto B \cdot Y_m\left(\frac{k_0 R_c}{R(z)} \cdot r\right) \ , \qquad \text{for } r > R(z) \ . \tag{2.14}$$

As well as

$$H_z(r, z) \propto C \cdot J_m\left(\frac{k_0 n R_c}{R(z)} \cdot r\right) \ , \qquad \text{for } r \leq R(z) \ . \tag{2.15}$$

$$H_z(r, z) \propto D \cdot Y_m\left(\frac{k_0 R_c}{R(z)} \cdot r\right) \ , \qquad \text{for } r > R(z) \ . \tag{2.16}$$

Whispering-gallery mode resonators support modes of two perpendicular polarizations. In transverse magnetic modes (TM modes), the electric field is parallel to the resonator axis and therefore only the components E_z, H_r and H_ϕ contribute to the electromagnetic field, whereas in transverse electric modes (TE modes) H_z, E_r and E_ϕ are the only non-vanishing components. By inserting E_z and H_z in Eq. (2.10) the complete electric field distribution is obtained. The constants A, B, C and D are calculated using the following conditions for an electromagnetic field at a dielectric interface between two media with refractive index n_1 and n_2 [Mes04].

$$(\vec{E}_2 - \vec{E}_1) \times \vec{e}_N = 0, \qquad (n_2^2 \vec{E}_2 - n_1^2 \vec{E}_1) \cdot \vec{e}_N = 0 \ . \tag{2.17}$$

$$(\vec{H}_2 - \vec{H}_1) \times \vec{e}_N = 0, \qquad (\vec{H}_2 - \vec{H}_1) \cdot \vec{e}_N = 0 \ . \tag{2.18}$$

Here $\vec{E}_1$, $\vec{E}_2$ and $\vec{H}_1$, $\vec{H}_2$ are the electric and magnetic field amplitudes in the media in direct proximity to the interface. The normal vector $\vec{e}_N$ is perpendicular to the interface. Using the relations

$$
\begin{aligned}
J'_m(x) &= 1/2 \left(J_{m-1}(x) - J_{m+1}(x) \right) \ , \\
Y'_m(x) &= 1/2 \left(Y_{m-1}(x) - Y_{m+1}(x) \right) \ ,
\end{aligned}
\tag{2.19}
$$

one obtains the following conditions at the resonator surface, at $z = z_c$, for TM polarization

$$
\begin{aligned}
E_z : & \quad A \cdot J_m(k_0 n R_c) = B \cdot Y_m(k_0 R_c) \ , \\
H_\phi : & \quad n A \cdot J'_m(k_0 n R_c) = B \cdot Y'_m(k_0 R_c)
\end{aligned}
\tag{2.20}
$$

and analog for TE polarization

$$
\begin{aligned}
H_z : & \quad C \cdot J_m(k_0 n R_c) = D \cdot Y_m(k_0 R_c) \ , \\
E_\phi : & \quad C \cdot J'_m(k_0 n R_c) = n D \cdot Y'_m(k_0 R_c) \ .
\end{aligned}
\tag{2.21}
$$

The condition obtained for E_r is identical to that for H_z.

Resonance condition

In order to solve these equations, λ_0 and R_c can not be independently chosen. The resonance condition dictates that the optical path length has to be an integer multiple of the wavelength of the light field coupled into the resonator. In [War07] the resonance condition for both polarizations is obtained by dividing the expression for H_ϕ and E_z in the case of TM polarization and the expressions for E_ϕ and H_z and in the case of TE polarization

$$
TM : \quad F_{TM}\left(\lambda_0, R_c\right) = n \frac{J'_m\left(k_0 n R_c\right)}{J_m\left(k_0 n R_c\right)} - \frac{Y'_m\left(k_0 R_c\right)}{Y_m\left(k_0 R_c\right)} = 0 \ ,
\tag{2.22}
$$

$$
TE : \quad F_{TE}\left(\lambda_0, R_c\right) = \frac{J'_m\left(k_0 n R_c\right)}{J_m\left(k_0 n R_c\right)} - n \frac{Y'_m\left(k_0 R_c\right)}{Y_m\left(k_0 R_c\right)} = 0 \ .
\tag{2.23}
$$

In Fig. 2.2 (a), $F_{TM}\left(\lambda_0, R_c\right)$ is plotted as a function of R_c exemplarily for TM polarization. The wavelength is fixed to $\lambda_0 = 852$ nm. For $m = 180$ a series of resonant radii and corresponding modes, differing in the number of nodes p along the radial coordinate, are identified, see Fig. 2.2 (b–d). Since the fundamental mode, corresponding to $p = 0$ and maximum angular momentum, exhibits the smallest mode volume and the tightest confinement it will be used for the following calculations. Figure 2.3 shows the field components for the lowest order, TE polarized radial mode obtained by the same method. In order to calculate the mode volume, the intensity distribution has to be normalized to unity. Thus, the amplitudes are normalized using $\mathrm{Max}\left(|E_z|\right)$ for TM polarization and $\mathrm{Max}((|E_r|^2 + |E_\phi|^2)^{1/2})$ for TE polarization.
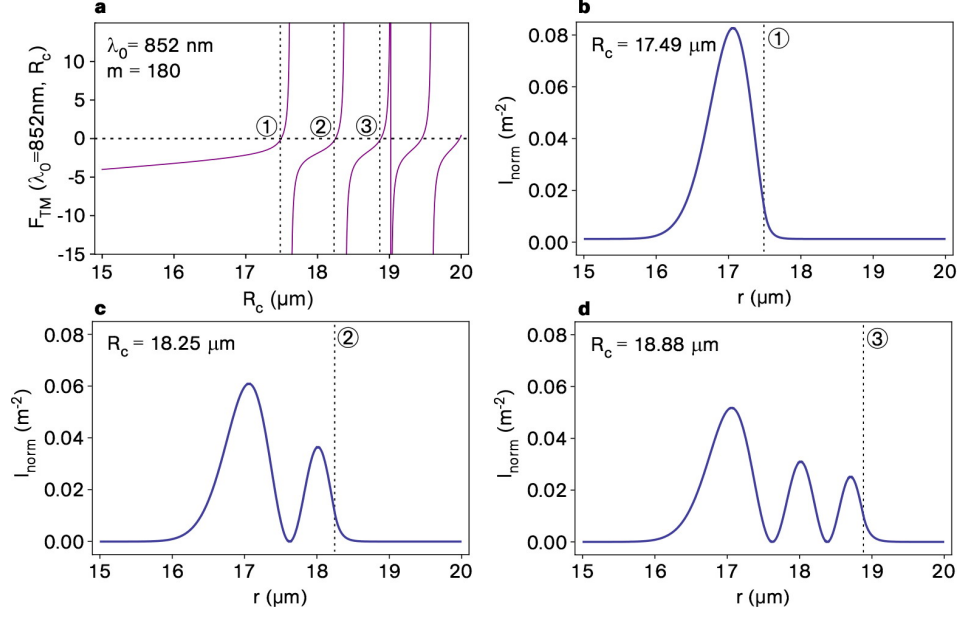
Figure 2.2: Solving the radial wave equation for TM polarization and $m = 180$. (a) In order to identify resonant caustic radii, $F_{TM} (\lambda_0 = 852 \text{ nm}, R_c)$ is plotted for R_c ranging from 15 μm to 20 μm and for a fixed wavelength of $\lambda_0 = 852$ nm. The roots at $R_c = 17.49$ μm, $R_c = 18.25$ μm and $R_c = 18.88$ μm correspond to radii that fulfill the resonance condition. Radii $R_c < 17.49$ are not compatible with an angular momentum of $L_z = 180\hbar$. Plots (b–d) show the normalized radial intensity distribution $I_{\text{norm}}(r) = |E_z(r)|^2 / \int |E_z(r)|^2 r dr$ for all three radii R_c obtained in (a). The intensity is normalized with respect to the radial power density in order to allow a comparison of the peak intensities of the different modes. For the smallest resonant radius, $L_z = 180\hbar$ coincides with the maximum possible angular momentum $L_{z,\text{max}} = \hbar m_{\text{max}}$ and the fundamental radial mode is obtained (b). This mode travels closest to the surface and offers the strongest confinement. For larger radii, m_{max} increases and the modes exhibit $p = m_{\text{max}} - m$ nodes along the radial coordinate.
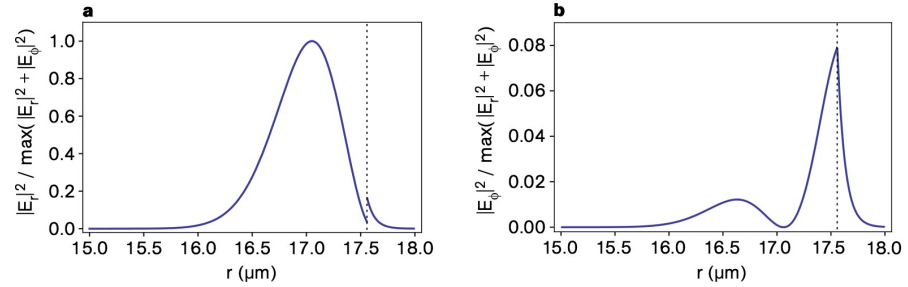
Figure 2.3: $|E_r|^2/\max(|E_r|^2 + |E_\phi|^2)$ (a) and $|E_\phi|^2/\max(|E_r|^2 + |E_\phi|^2)$ (b) for the fundamental radial, TE polarized mode. For a wavelength of $\lambda_0 = 852$ nm and $m = 180$ the resonance condition is fulfilled for a radius of $R_c = 17.56$ μm. Note the discontinuity of $|E_r|^2$ at the surface (dashed line). The radial intensity distribution is proportional to $|\vec{E}|^2 = |E_r|^2 + |E_\phi|^2$. Both field components, E_r and E_ϕ are normalized by dividing them by the maximum value of $|\vec{E}|$.
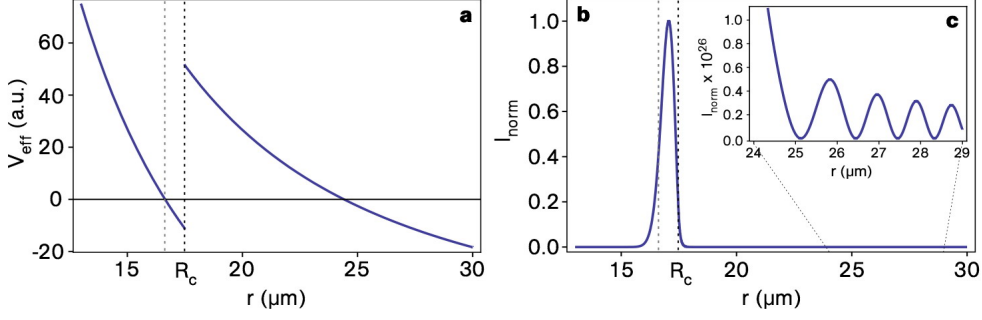
Figure 2.4: (a) Considering the form of the radial wave equation one can define an effective potential for the light confined in a resonator mode. The plot shows V_{eff} for $m_{\text{max}} = 180$ in a bottle microresonator with $R_c \approx 17.49$ μm for a wavelength of 852 nm. (b) Normalized radial intensity distribution $I_{\text{norm}} = |E_z|^2/\max(|E_z|^2)$ of the corresponding TM mode. The mode is located in the region $V_{\text{eff}} \leq 0$, whereas for $V_{\text{eff}} > 0$ the fields are purely evanescent. (c) For larger radii of approximately 25 μm , V_{eff} again becomes positive and gives rise to an unbound, propagating light field. Note the scaling factor of 10^{26} between (b) and (c). Due the rapid exponential decay of the intensity outside of the silica resonator structure the losses due to coupling of the confined fields to the radiating modes are negligible in this case.

Radiation caustic

Whispering-gallery modes are spatially not perfectly confined. Total internal reflection that occurs on a curved surface is not perfectly lossless. Defining an effective potential from the radial wave equation, Eq. (2.8), helps to understand this phenomenon

$$V_{\text{eff}} = -k_\phi\left(z\right)^2 + \frac{m^2}{r^2} \ . \tag{2.24}$$

In Fig. 2.4, V_{eff} is plotted against the radial coordinate at the caustic of the resonator with $R_c = 17.49$ μm for $m = 180$. In the "forbidden" regions, defined by $V_{\text{eff}} > 0$, the fields are purely evanescent. The confined WGM is located in the region close to the surface, where $V_{\text{eff}} \leq 0$. For large radii, where V_{eff} becomes positive again, an unbound propagating light field exists. The radiation caustic R_{rad} is defined as the first node of $|\vec{E}|^2$ outside of the silica resonator structure. Whenever integrating over the radial intensity distribution, R_{rad} is chosen as the upper limit for the integral. That means that only the confined mode and the evanescent field outside of the resonator are considered.

Effective resonator radius and wave number

The z-component of the angular momentum of a bottle mode $L_z = m\hbar$ can be approximated by $L_z \approx R_c \cdot \hbar k_\phi(z_c) = R_c \cdot \hbar k$. The absolute value of the wave number is then given by $k \approx m/R_c$. Strictly, because of the modes finite radial width, one has to define an effective radius $R_{\text{eff}} = c_r \cdot R_c$ by introducing an correction factor c_r. The exact value of k is then obtained by radial integration, where $1/r$ is weighted with $n^2(r) \cdot |E(r, z = z_c)|^2$

and then divided by $\int_0^{R_{rad}} n^2(r)|E(z=z_c)|^2 dr$ for normalization [War07]

$$k = m/(c_r R_c) = m \frac{\int_0^{R_{\mathrm{rad}}} n^2(r) \cdot |E(z=z_c)|^2 \cdot (1/r)\,dr}{\int_0^{R_{\mathrm{rad}}} n^2(r) \cdot |E(z=z_c)|^2 dr} \ . \tag{2.25}$$

For the fundamental TM mode, whose radial intensity distribution is shown in Fig. 2.2 (b), one obtains $c_r = 0.970$ for a caustic radius of $R_c = 17.49$ μm.

2.1.3 Solving the axial wave equation

Using Eq. (2.4) the axial wave equation can be written as

$$\partial_z^2 Z + \left(k^2 - k_\phi^2\right) \cdot Z = 0 \ . \tag{2.26}$$

In order to solve for the eigenfunctions Z and the eigenvalues $k_{m,q}$, one eliminates k_ϕ via $k_\phi(z) = k \cdot R_c/R(z) = m/(c_r R(z))$ using Eq. (2.25). Moreover, according to the analysis in [Lou05], the following expression for the resonator profile $R(z)$ is chosen

$$R(z) = R_0/\sqrt{1 + (\Delta k z)^2} \ . \tag{2.27}$$

In [Sum04, Lou05], it is shown that a resonator with such a radius profile exhibits an equidistant mode spacing. For typical bottle microresonator dimensions, for which $(\Delta k z)^2 \leq 0.014$, this expression corresponds to a close approximation to the parabolic radius profile given in Eq. (2.1). The axial wave equation then takes the form

$$\partial_z^2 Z + \left(k^2 - \left(\frac{m}{c_r R_0}\right)^2 - \left(\frac{m\Delta k}{c_r R_0}\right)^2 \cdot z^2\right) \cdot Z = 0 \ . \tag{2.28}$$

This differential equation is equivalent to the harmonic oscillator

$$\partial_z^2 Z + (E_{\mathrm{kin}} - V(z)) \cdot Z = 0 \ , \tag{2.29}$$

with the "kinetic energy" E_{kin} and the "potential energy" $V(z)$. For the bottle microresonator one identifies

$$E_{\mathrm{kin}} = k^2 - m^2/(c_r R_0)^2 \tag{2.30}$$

and

$$V(z) = \left(\frac{\Delta E_m \cdot z}{2}\right)^2 \ , \tag{2.31}$$

with $\Delta E_m = 2m\Delta k/(c_r R_0)$. The condition that Z be square integrable leads to a discrete set of energy levels $E_{mq} = (q+1/2)\Delta E_m$. The axial quantum number $q \in \mathbb{N}$ (non-negative integer) gives the number of nodes in the axial intensity distribution. The allowed eigenvalues for the wave number are given by

$$k_{m,q} = \frac{m}{c_r R_c} = \sqrt{\frac{m^2}{(c_r R_0)^2} + (q+1/2)\frac{2m\Delta k}{c_r R_0}} \ . \tag{2.32}$$

The solutions for Z are given by a combination of a Hermite Polynomial H_q and a Gaussian

$$Z_{m,q}(z) = H_q\left(\sqrt{\frac{\Delta E_m}{2}} \cdot z\right) \exp\left(-\frac{\Delta E_m}{4}z^2\right) \ . \tag{2.33}$$

The last unknown quantities are R_0 and $z_c = \left((R_0/R_c)^2 - 1\right)^{1/2} \cdot \Delta k^{-1}$. Comparing $k = m/(c_r R_c)$ with the eigenvalues $k_{m,q}$ leads to a quadratic equation

$$\frac{m^2}{(c_r R_0)^2} + \frac{2m\Delta k \cdot (q + 1/2)}{c_r R_0} - \frac{m^2}{(c_r R_c)^2} = 0 \ . \tag{2.34}$$

By choosing $q = 1$ and $m = 180$, corresponding to $R_c = 17.49$ and $c_r = 0.970$ for TM polarization, the central radius of the resonator considered here ($\Delta k = 0.012 \ \mu m^{-1}$) , is fixed to $R_0 = 17.522 \ \mu m$. In order to obtain the axial intensity distribution of the four TM polarized lowest order axial bottle modes ($q = 1$–4) , the axial wave function $Z_{m,q}$ is calculated for each mode according to Eq. (2.33) , again using $c_r = 0.970$. Due to the small radius modulation in the central region of the bottle microresonator structure, the correction factor $c_r = 0.970$, calculated from the radial intensity distribution of the TM polarized $q = 1$ mode, also applies to the higher order axial modes to a close approximation. Figure 2.5 shows the normalized axial intensity distribution $I_{\text{norm}} = Z_{m,q}^2/\max(Z_{m,q}^2)$ for the $q = 1$–4 modes. For modes with higher order axial quantum number the caustic position shifts to larger z and thus R_c decreases. Therefore the resonance condition changes and the resonances shift to smaller wavelengths. In order to calculate the resonant wavelengths λ_q for the higher order modes, Eq. (2.34) is used to solve for $R_c(q)$. For this purpose the value of $c_r = 0.970$ obtained from the radial wave function of the respective $q = 1$ mode is again used. From the resulting values of $R_c(q)$, λ_q can be calculated as illustrated in Fig. 2.6. Finally, the radial intensity distribution of the higher order axial modes is obtained for the given resonator dimensions as described above.
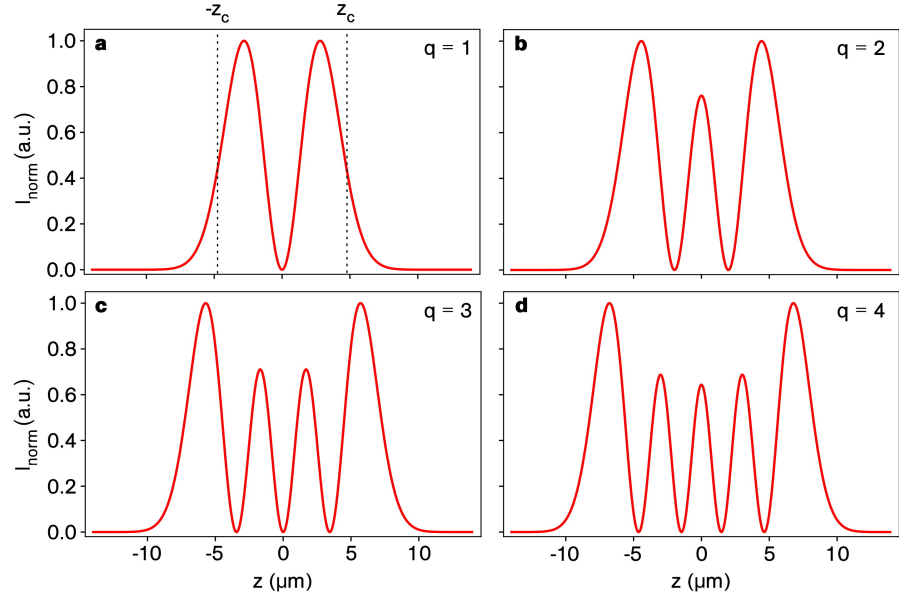
Figure 2.5: Normalized axial intensity distribution $I_{\mathrm{norm}} = Z_{m,q}^2/\max(Z_{m,q}^2)$ of the four lowest order TM polarized axial bottle modes. The axial quantum number q gives the number of nodes along the resonator axis. The solutions are well known from the quantum mechanical harmonic oscillator. Note the enhancement of the intensity near the caustics, where the evanescent field is most pronounced. The two caustics can be used as two well-separated, symmetric coupling ports where light can be coupled into and out of the resonator. The dotted lines in (a) indicate the caustic positions $\pm z_c$, which do not coincide with the maxima of $Z_{m,q}^2$. In the energetically "forbidden" regions $|z| > z_c$ the electric field has to decay exponentially. For a continuously differentiable electric field, this condition can only be fulfilled if the maxima of the axial intensity distribution are shifted towards the resonator's center with respect to $\pm z_c$.
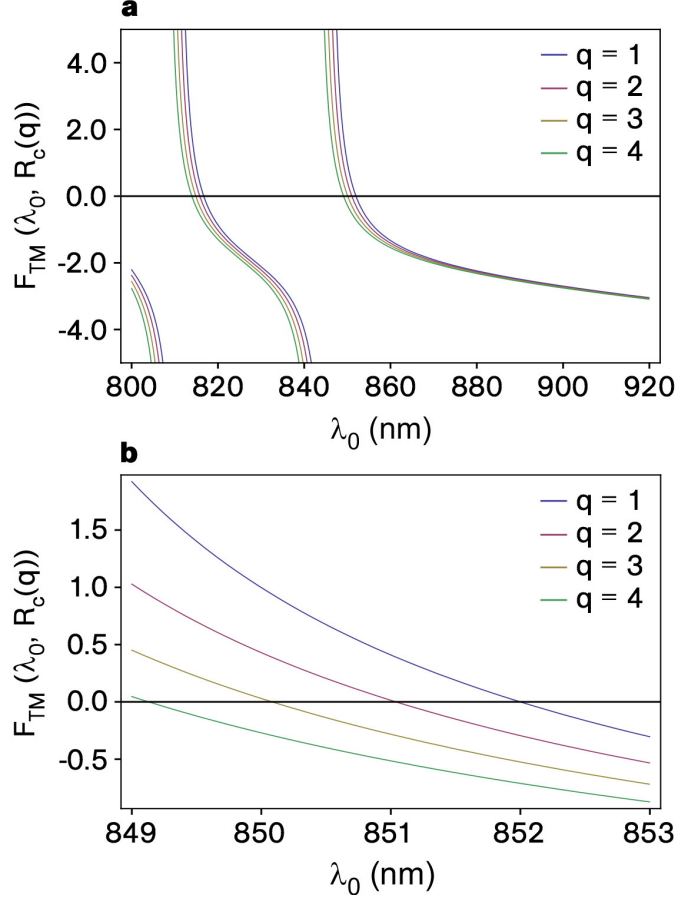
Figure 2.6: Identifying the resonant wavelengths for the four lowest order, TM polarized axial bottle modes. In (a) $F_{TM}(\lambda_0, R_c(q))$ from Eq. (2.22) is plotted with a fixed radius $R_c(q)$ for each mode. (b) shows a smaller range of λ. The roots of each curve mark λ_q. The spectral mode spacing $\Delta\nu_q$ is found to be 397 GHz between the two lowest order modes. For the higher order modes, it slightly decreases by approximately 0.1%. This slight deviation from the equidistant mode spacing, expected from the radius profile given in Eq. (2.27) that is used for solving the axial wave equation, is ascribed to the approximation of c_r when solving Eq. (2.34) for $R_c(q)$.

q	$V_{180,q}$ (TM)	$V_{180,q}$ (TE)
1	1113 μm^3	1176 μm^3
2	1244 μm^3	1314 μm^3
3	1330 μm^3	1406 μm^3
4	1395 μm^3	1474 μm^3

Table 2.1: Mode volumes for the four lowest order axial modes for both polarizations in a resonator with $R_0 \approx 17.5$ μm, a curvature of $\Delta k = 0.012$ and $m = 180$.

2.1.4 Calculating spectral and spatial properties

Finally, the mode volume and the free spectral range of the bottle microresonator are calculated from the above findings.

Mode volume

The radial and axial intensity distribution of a bottle mode with quantum numbers q and m allows one to directly calculate its mode volume $V_{m,q}$ [Lou05]. For this purpose, the intensity distribution is normalized to unity $I_{m,q}/I_{m,q}^{\max}$ and is then integrated over $\mathbb{R}^3$

$$V_{m,q} = \iiint_0^{R_{\mathrm{rad}}} n^2(r) \frac{I_{m,q}(r,z)}{I_{m,q}^{\max}} r d_r d_\phi d_z . \tag{2.35}$$

The upper limit for the radial integral is set to R_{rad}. Due to the cylindrical symmetry, the integration over the azimuthal coordinate yields $\int |e^{im\phi}|^2 d_\phi = 2\pi$. In order to facilitate computation of the mode volume, the integral is split into a radial and an axial part

$$V_{m,q} \approx 2\pi \cdot \int \left(\frac{Z_{m,q}(z)}{Z_{m,q}^{\max}}\right)^2 d_z \cdot \int_0^{R_{\mathrm{rad}}} n^2(r) \left(\frac{|\vec{E}(r)|^2}{\max(|\vec{E}(r)|^2)}\right) r d_r . \tag{2.36}$$

Table 2.1 shows the calculated mode volumes for the lowest order axial modes in a resonator with $R_0 = 17.522$ μm, a curvature of $\Delta k = 0.012$ and $m = 180$ for both polarizations.

Mode spectrum

The axial and azimuthal free spectral range $\Delta\nu_q = \nu_{m,q+1} - \nu_{m,q}$ and $\Delta\nu_m = \nu_{m+1,q} - \nu_{m,q}$ can be derived from the eigenvalues $k_{m,q}$ of the wave function. In close approximation they can be written as

$$\Delta\nu_m = \frac{c}{2\pi n}(k_{m+1,q} - k_{m,q}) \approx \frac{c}{2\pi n c_r R_0} \tag{2.37}$$

and

$$\Delta\nu_q \approx \frac{c\Delta k}{2\pi n} . \tag{2.38}$$

For a bottle microresonator with $R_0 = 17.5$ μm and $\Delta k = 0.012$ μm^{-1} the above formula yields an axial FSR of $\Delta\nu_q = 391$ GHz that is about a factor of five smaller than the azimuthal FSR of $\Delta\nu_m = 1.9$ THz.
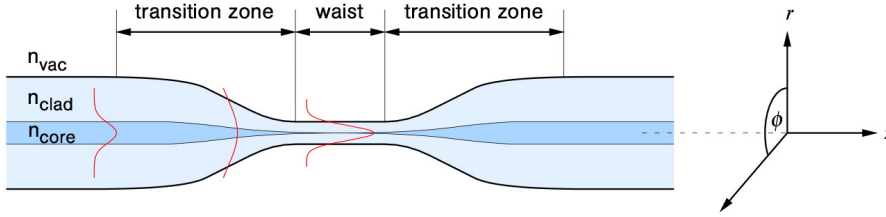
Figure 2.7: Schematic of an ultra-thin tapered optical fiber. The fiber is produced from a commercial step-index glass fiber using a heat-and-pull technique. In the thick fiber ends the mode is guided by total internal reflection induced by the weak refractive index contrast between core and cladding $n_{core} - n_{clad} \ll 1$. The mode in the ultra-thin fiber waist is guided due to the refractive index contrast between the cladding and the surrounding medium $n_{clad} - n_{vac} \approx 0.5$. Shaping the transition zone for optimal coupling between both modes is a prerequisite to obtain high transmission of optical power through the fiber taper [Lov86, War07].

2.2 Ultra-thin optical fibers

Optical step-index glass fibers consist of a core with refractive index n_{core} and a cladding with refractive index n_{clad}. They are commonly made of silica. The core has a slightly increased refractive index, typically due to doping with germanium. In these fibers the light is guided by continuous total internal reflection at the core-cladding interface. Due to the small refractive index contrast $n_{core} - n_{clad} \ll 1$, such waveguides are classified as "weakly guiding". Using a heat-and-pull technique optical fibers can be tapered down to sub-μm diameters [Bir92, Ton03, Bra04, Clo05]. In the sub–μm section, the total internal reflection then occurs at the interface of the cladding and the surrounding medium n_{air} or n_{vac} because the core diameter is now negligible with respect to the wavelength of the guided light. Due to the high refractive index contrast, this case is referred to as "strongly guiding". A schematic of such a ultra-thin tapered fiber is shown in Fig. 2.7. The evanescent field outside the ultra-thin fiber waist exponentially decays at a length scale of a few hundred nanometers in the optical domain. Due to the strong confinement of the mode, the intensity inside the fiber and near the fiber surface is much larger than for a commercial step-index fiber carrying the same power. Therefore these fibers find applications in various fields from nonlinear optics and ultra-sensitive absorption spectroscopy to cold atom physics [Leo04, Sti09, Vet10]. In [Kni97] coupling of light into whispering-gallery modes by frustrated internal reflection using an ultra-thin fiber was demonstrated for the first time. Today, ultra-thin fiber couplers are routinely used with WGM resonators. The wave numbers of both the fundamental fiber mode and the resonator modes can be easily matched by variation of the waist diameter [Kni97]. For a properly chosen fiber diameter the coupling between the resonator mode and the fundamental fiber mode is dominant and the coupler shows almost ideal single-mode to single-mode coupling characteristics [Spi03]. Moreover, the scattering losses introduced by the ultra-thin fiber are negligible. In the following, a brief description of the mode propagation in step-index fibers and ultra-thin fiber tapers is given, followed by a description of the fabrication process.

2.2.1 Theoretical description of light propagation in glass fibers

In [Yar91] the mode propagation in step-index circular waveguides is described. In this general approach, a structure with cylindrical symmetry along z, radius a and refractive index n_1, embedded in a medium with refractive index $n_2 < n_1$ is assumed. As in the analysis of bottle modes, first the Helmholtz equation is solved for E_z and H_z. The other field components are then calculated using Maxwell's equations. For a mode with angular momentum along the fiber axis $L_z = l\hbar$ (with integer $l \in \mathbb{Z}$) and the so-called propagation constant β, one chooses the following ansatz

$$\begin{bmatrix} E_z \\ H_z \end{bmatrix} = \Psi(r) \cdot exp\left(i\left(\omega t - \beta z + l\phi\right)\right) \ . \tag{2.39}$$

The propagation constant is given by $\beta = k_0 \cdot n_{\text{eff}}$, with an effective refractive index $n_1 > n_{\text{eff}} > n_2$ resulting from the localization of the mode in both media. The fields have to fulfill the Helmholtz equation

$$\left(\partial_r^2 + \frac{1}{r}\partial_r + \frac{1}{r^2}\partial_\phi^2 + \partial_z^2 + k^2\right) \cdot \begin{bmatrix} E_z \\ H_z \end{bmatrix} = 0 \ , \tag{2.40}$$

which by exploiting the z and ϕ dependency from Eq. (2.39), again takes the form of a Bessel differential equation

$$\left(\partial_r^2 + \frac{1}{r}\partial_r + \left(k^2 - \beta^2 - \frac{l^2}{r^2}\right)\right)\Psi(r) = 0 \ . \tag{2.41}$$

In the case of a vanishing value of β, i.e., no propagation along the fiber axis, this equation is identical to Eq. (2.8) describing a WGM mode. Since the sign of $k^2 - \beta^2$ is opposite in both media two different types of solutions can be found. For $r < a$, where $h^2 = n_1^2 k_0^2 - \beta^2 > 0$ one obtains

$$\begin{bmatrix} E_z \\ H_z \end{bmatrix} \propto \begin{bmatrix} A \\ B \end{bmatrix} J_l\left(hr\right) \cdot \exp\left(i\left(\omega t + l\phi - \beta z\right)\right) \ . \tag{2.42}$$

In contrast, for $r > a$, where $q^2 = n_2^2 k_0^2 - \beta^2 < 0$ the equation is solved by the modified Bessel functions of the second kind K_l

$$\begin{bmatrix} E_z \\ H_z \end{bmatrix} \propto \begin{bmatrix} C \\ D \end{bmatrix} K_l\left(qr\right) \cdot \exp\left(i\left(\omega t + l\phi - \beta z\right)\right) \ . \tag{2.43}$$

Using Maxwell's equations the missing field components are then calculated. The coefficients A, B, C, D are derived from the properties of the fields at the interface. Moreover, in analogy to the resonance condition for bottle modes, a transcendental equation that can be used to solve for the propagation constant β is obtained

$$l^2 \left[\left(\frac{1}{qa}\right)^2 + \left(\frac{1}{ha}\right)^2\right]^2 \left(\frac{\beta}{k_0}\right)^2 = \left(\frac{J_l'\left(ha\right)}{haJ_l\left(ha\right)} + \frac{K_l'\left(qa\right)}{qaK_l\left(qa\right)}\right)$$
$$\left(\frac{n_1^2 J_l'\left(ha\right)}{haJ_l\left(ha\right)} + \frac{n_2^2 K_l'\left(qa\right)}{qaK_l\left(qa\right)}\right) \ . \tag{2.44}$$
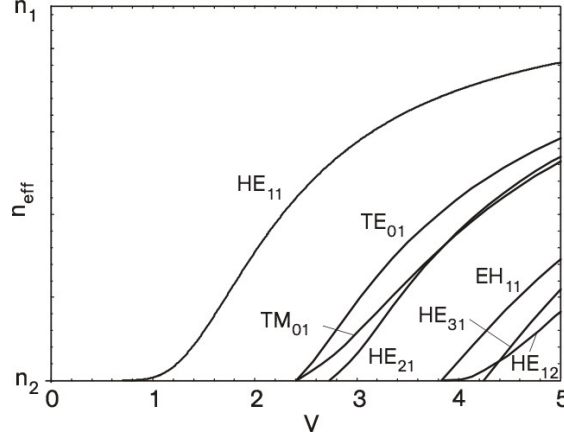
Figure 2.8: The normalized propagation constant $\beta/k_0 = n_{\text{eff}}$ as a function of the V-parameter for various solutions of Eq. (2.44). The fundamental HE_{11} mode exists for all fiber radii. All other modes are only guided if the fiber radius is larger than a certain cutoff radius.

For each value of l this equation yields a set of propagation constants $\beta_{l,m}$ with positive integer $m \in \mathbb{N} - \{0\}$ from which the field distribution of each particular mode can be calculated using the above equations.

In general, two classes of solutions exist. For $l = 0$, i.e., for modes with vanishing angular momentum along the z-axis, the fields are azimuthally symmetric and the modes are denoted by TE_{0m} (transverse electric) and TM_{0m} (transverse magnetic). In TE_{0m} modes H_r, H_z and E_ϕ are the only non-vanishing components, whereas TM_{0m} modes only consist of E_r, E_z and H_ϕ. For $l > 0$ the solutions are much more complicated. These "hybrid modes", EH_{lm} and HE_{lm}, have six nonzero field components. HE_{11} is the fundamental mode. As will be shown in the following, this mode exhibits the largest n_{eff} and is the only mode that is guided for arbitrarily small fiber radii a.

These general solutions apply to both, the strongly guiding ultra-thin fiber waist as well as the weakly guiding step-index fiber. However, for the latter case, simpler solutions can be found using $n_1 - n_2 \ll 1$. For this condition, matching of the fields at the interface according to Eq. (2.17/2.18) is simplified and Eq. (2.44) becomes linear in β. The number of solutions is reduced by a factor of two and the propagation constants of $EH_{l-1,m}$ and $HE_{l+1,m}$, that solve the linear equation, become degenerate in this approximation. Superpositions of the $EH_{l-1,m}$ and $HE_{l+1,m}$ modes then lead to the linearly polarized LP_{lm} modes. The fundamental "weakly guided" LP_{01} mode is obtained from the quasi-liner polarized fundamental HE_{11} for $n_1 - n_2 \ll 1$.

Figure 2.8 shows the normalized propagation constant $n_{\text{eff}} = \beta/k_0$ as a function of the V-parameter, $V = k_0 a \sqrt{n_1^2 - n_2^2}$, for various modes of the fiber waist. The first higher order modes are the TE_{01} and the TM_{01} modes. For $V = 2.405$ the effective refractive index n_{eff} reaches the value of the refractive index in the optically thinner medium n_2 for both modes. As a result, these modes are no longer guided for radii with $V \leq 2.405$.

The corresponding cutoff radius is given by

$$a_{\text{cutoff}} = \lambda_0 \cdot \frac{2.405}{2\pi\sqrt{n_1^2 - n_2^2}} = 310 \text{ nm} , \qquad \text{for } \lambda_0 = 852 \text{ nm} . \qquad (2.45)$$

This value is also referred to as the single mode cutoff radius because for smaller radii only the fundamental HE_{11} is guided.

2.3 Fabrication of bottle microresonators and ultra-thin optical fibers

I will now describe the fabrication of our ultra-thin optical fibers and bottle microresonators from commercial glass fibers using a heat-and-pull technique. When not explicitly stated, a step-index single mode fiber with an operation wavelength of 830 nm (Newport, F-SF) is used. The company specifies a cladding diameter of 125 μm, a mode field diameter of 5.6 μm and an absorption of 5 dB/km. Before processing the fiber, the mechanical buffer is removed with a special tool and the fiber surface is cleaned with acetone (Merck, Aceton UVASOL). The fiber pulling rig used for fabrication of both structures is schematically shown in Fig. 2.9. A detailed description of the rig, as
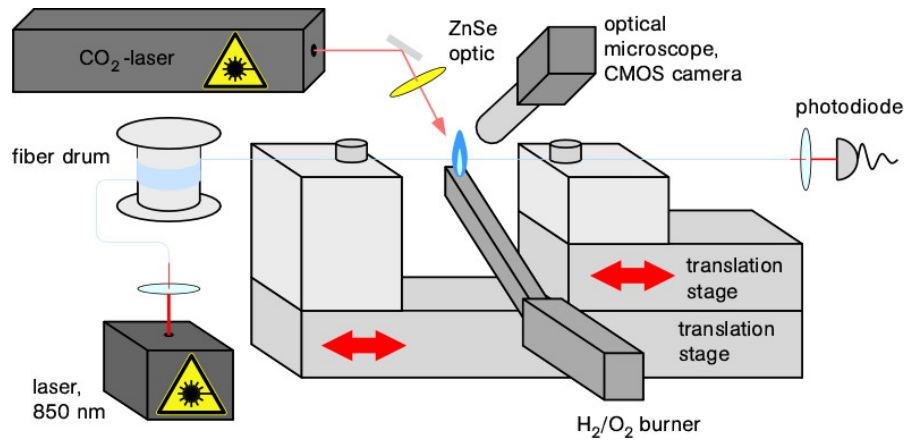
Figure 2.9: Schematic of the so-called "fiber pulling rig", used to fabricate ultra-thin optical fibers and bottle microresonators. A commercial optical fiber is clamped to two translation stages. One stage is mounted on top of the other. The fiber is then heated by an oxygen-hydrogen flame with a width of 1 mm. The upper stage, called "stretcher", elongates the heated fiber, while the "translater" moves it relative to the flame ("flame-brush technique"). Alternatively, a focused CO_2-laser beam with a maximum power of 30 W (Synrad, Series 48-2) can be used as a heat source. The laser beam is focused by a ZnSe lens ($f = 48$ mm) and only heats a 100 μm – 150 μm wide section of the fiber. A microscope connected to a CMOS camera allows one to take micrographs of processed fibers. Moreover, during the fabrication of ultra-thin optical fibers, the transmission of a diode laser emitting at a wavelength of 850 nm through the fiber is monitored.

well as of the fabrication of ultra-thin optical fibers and bottle microresonators is given in [Poe06, War07].

2.3.1 Ultra-thin optical fibers

Using the flame as a heat source, ultra-thin optical fibers with diameters down to 100 nm can be produced. In order to tailor the shape and slope of the transition zone and to create a waist of arbitrary length, the effective flame-width is varied during the pulling process by moving the fiber relative to the heat source. The movement of the translation stages is controlled via a computer and calculated to yield the desired fiber shape. In this work, I use fibers with a waist diameter of typically 500 nm. The typical transmission after fabrication is larger than 97%.

2.3.2 Bottle microresonators

The fabrication process for bottle microresonators consists of two steps. Figure 2.10 shows the structure resulting from each step. First, a few millimeter-long section with a homogeneous diameter corresponding to the desired resonator diameter is created by
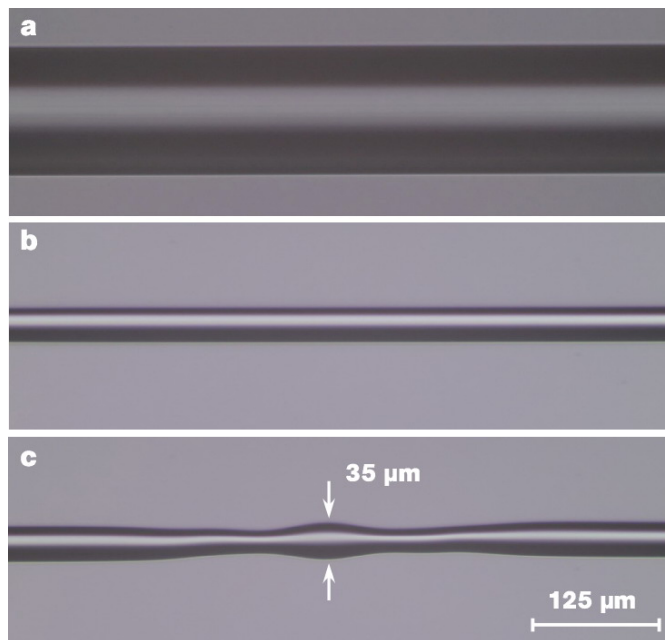
Figure 2.10: Micrographs showing the fabrication of a typical bottle microresonator in 2 steps, starting from a commercial 125–μm diameter optical step-index fiber (a). (b) First, a section with a homogeneous diameter of 35 μm is created by simultaneously heating and stretching the fiber. (c) Next, local heating by a focused CO_2-laser beam and simultaneous elongation creates two microtapers on the fiber waist separated by approximately 150 μm. The bulge between the microtapers forms a bottle microresonator of radius $D_0 = 35$ μm.
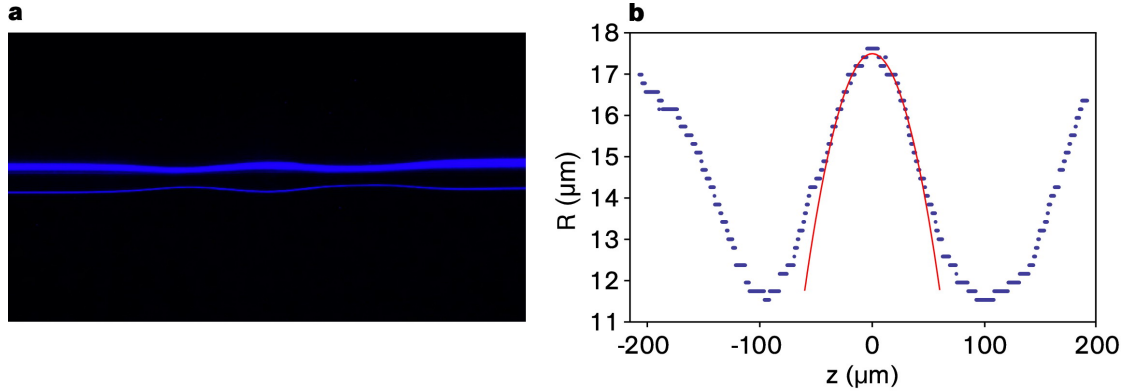
Figure 2.11: Reconstructing the diameter profile of a bottle microresonator. (a) Micrograph of a typical bottle microresonator taken after fabrication. Since the customized image analysis software uses only the information from the blue pixels all other pixels are deactivated. A flashlight mounted in the fiber pulling rig is used for illumination. (b) Reconstructed diameter profile with a parabolic fit (red) . Only the data in the region $z = \pm 35$ mum have been considered for the fit. In the central zone where the mode is guided the resonator profile shows close agreement with a parabola of the form $D(z) \approx D_0 \cdot [1 - 1/2 \, (\Delta k \cdot z)^2]$. The fit yields $D_0 = 35$ μm and $\Delta k = 0.0135$ μm^{-1}.

the flame-brush technique described above. This step is accomplished using the hydrogen/oxygen flame or the focused CO_2-laser beam. Next, a bulge is formed on the fiber waist between two microtapers. Each of the microtapers is realized by locally heating the fiber waist with the focussed CO_2-laser beam, while slightly stretching it. The central zone of the resulting bulge exhibits a parabolic variation of the fiber diameter and forms the bottle microresonator. Typical resonator diameters lie in the $D_0 = 30$–45 μm range. Adjustment of the CO_2-laser beam spot size, the microtaper separation, and the elongation length allows one to precisely tailor the resonator. Typically, curvatures of $\Delta k = 0.009$–0.020 μm^{-1} are used. In order to create bottle microresonators with curvatures of 0.012 or higher, a third fabrication step is applied. The central bulge is heated to a temperature close to the melting point. The bulge then deforms due to surface tension, increasing the resonator's curvature.

Finally, the diameter profile is measured using the microscope in combination with a customized image analysis software. A typical micrograph taken on a resonator after fabrication and the inferred profile is shown in Fig. 2.11. The programm successively scans the pixels of each line of the micrograph and automatically detects the fiber edges. From this data the profile can be calculated after calibration of the microscope using a test target with known dimensions. An analysis of the obtained accuracy shows that this method allows one to determine the local diameter with a precision of ± 2 μm and Δk with a precision of ± 0.001 μm^{-1} and. The accuracy is mostly limited by the resolution of the optical microscope. In [Poe06, War07] the profile of bottle microresonators is reconstructed from the diffraction pattern obtained by shining a collimated laser beam at the resonator. This method provides a radial resolution much better than 100 nm. However, it is only applicable to resonators of curvatures around 0.004 μm^{-1}.

3 Coupling and Characterization of bottle modes

Efficient coupling of propagating light fields into bottle modes requires phase matched excitation. In order to match the propagation constants of the input light field and the bottle mode, one has to make use of an auxiliary dielectric structure. For example, light can be coupled into WGM modes using the evanescent field generated by frustrated internal reflection at the surface of a prism [Bra89] or a side-polished optical fiber [Dub95]. In this work, light is coupled into a bottle mode by overlapping its evanescent field with that of an ultra-thin optical fiber [Kni97]. In doing so the ultra-thin fiber is not in direct contact with the resonator surface but an air gap of spatial width x is maintained between the surface of both structures. This "coupling gap" is measured perpendicular to the resonator axis. Changing x enables flexible adjustment of the strength of coupling between the light field propagating in the ultra-thin fiber and the bottle mode. The chapter starts with a description of the experimental setup used to couple light into bottle modes. A general model of coupling light into a resonator with losses is given, followed by an experimental investigation of the coupling junction between an ultra-thin optical fiber and a bottle microresonator. It is shown that light can be coupled into and out of bottle modes with high efficiency and minimal losses. Next, measurements on the spatial and spectral properties of bottle modes are presented. Ultra-high quality factors are observed using a cavity-ringdown technique and the optimal resonator parameters for highest Q/V-ratios are discussed. Finally, tuning of an UHQ bottle mode to an arbitrary, predetermined frequency is demonstrated. The combination of all these properties makes the bottle microresonator a promising candidate for CQED experiments as discussed in chapter 5 on the basis of the findings presented here.

3.1 Experimental setup

In the following, the mechanical and optical components of the experimental setup used to excite bottle modes are described. This setup is used throughout this work with only marginal modifications, which will be pointed out in the respective sections.

3.1.1 Mechanical components

A. Fiber holder   After fabrication, the fibers carrying the resonator and the ultra-thin fiber waists are attached to specialized holders that stabilize the structures and that allow one to apply mechanical strain along the fiber axis. A schematic of the fiber holder design is shown in Fig. 3.1. The unprocessed regions on both sides of the fiber
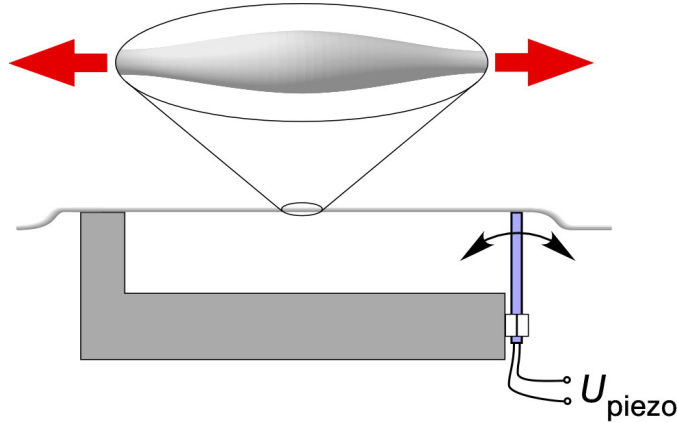
Figure 3.1: Schematic of the fiber holder design used to manipulate both, the ultra-thin fibers and the resonator fiber. The picture illustrates the application of mechanical strain to a bottle microresonator using an integrated piezo-electric bending actuator controlled by a voltage U_{piezo}. This design enables the tuning of bottle modes and the reduction of the vibration amplitude of the ultra-thin fiber waists.

taper are glued to the holder. One end of each fiber is attached to a bending piezo-electric actuator (Physik Instrumente, PL112.11). A voltage U_{piezo} of $0 - 30$ V can be applied to the actuator, corresponding to a displacement of $0 - 80$ μm. This setup allows one to strain-tune the resonance frequency of the bottle modes. Moreover, increasing the strain applied to the ultra-thin fibers reduces vibrations.

B. Positioning of the ultra-thin fibers A positioning system is used to align the ultra-thin fibers at one of the caustics of a particular bottle mode in close proximity to the resonator surface. The ultra-thin fibers are mounted perpendicularly to the resonator axis. The positioning system consists of three orthogonally oriented translation stages (Physik Instrumente, M-105). The actuator for each translation stage is chosen corresponding to the positioning accuracy and translation range required for the corresponding axis. A photograph of the positioning system is shown in Fig. 3.2. In the following, the positioning requirements for each axis are discussed.

- **Positioning along the resonator axis.** For coupling to different axial bottle modes the position of the ultra-thin fiber can be scanned along the resonator axis via a servomotor-driven translator (Physik Instrumente, M-232). Since the spatial modulation of the axial intensity distribution is on the order of a few micrometers, its resolution of 100 nm is sufficient to precisely place the fiber waist at one of the two caustics of a given mode for optimal coupling efficiency.

- **Control of the coupling gap.** The width x of the coupling gap between the ultra-thin fiber and the resonator has to be in the range of the decay length of the evanescent fields of both structures, i.e., a few hundred nanometers and is controlled with a resolution of 10 nm using a piezo-electric actuator (Physik In-
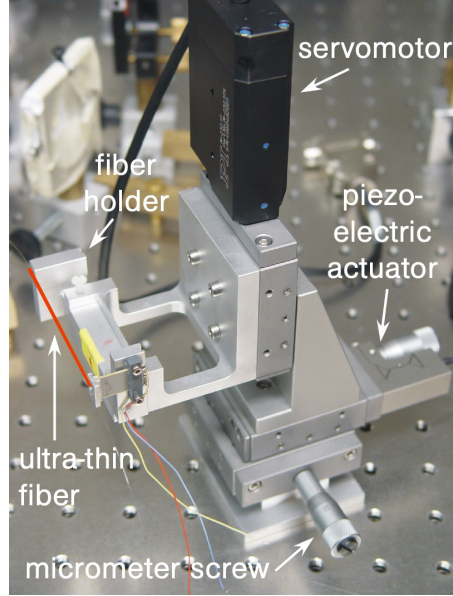
Figure 3.2: Mechanical system used for positioning an ultra-thin optical fiber (indicated by the red line). Three orthogonally oriented stages driven by a piezo-electric actuator, a servomotor and a micrometer screw are used to place the ultra-thin fiber at one of the caustics of the bottle microresonator.

strumente, P-854.00). A voltage of $0 - 100$ V corresponds to a travel range of 25 μm. A micrometer screw with a resolution of 1 μm and a travel range of 18 mm is used for coarse control of the coupling gap.

- **Translation along the axis of the ultra-thin fiber.** The third translation stage allows one to displace the ultra-thin fiber along its axis. A micrometer screw is accurate enough to place the 3–5 mm long fiber waist at the position of the resonator.

C. Microscope An optical microscope is used to image the bottle microresonator. Excited bottle modes are clearly visible from light scattered due to surface inhomogeneities. Even the position of an ultra-thin fibers can be clearly identified by light scattered from the fiber waist. The microscope objective (Mitutoyo, M Plan APO 10x) has a numerical aperture of 2.8 and a working distance of 33.5 mm. It offers a resolution of 1 μm and its depth of focus is 3.5 μm. Using a lens tube the objective is connected to a monochromatic CMOS camera with enhanced sensitivity in the near infrared (Allied Vision Technologies, Marlin F-131B).

D. Setup in "add-drop configuration" The geometry of bottle modes allows one to simultaneously access the resonator with two ultra-thin fibers, see Fig. 3.3, without the spatial constraints inherent to equatorial WGMs typically employed in microspheres and microtoroidal resonators. For bottle modes with axial quantum numbers $q \geq 1$,
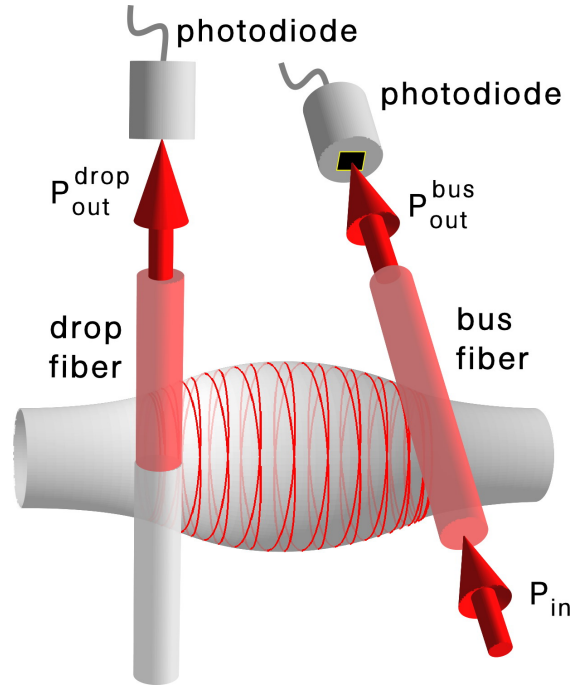
Figure 3.3: Schematic of the coupling setup in add-drop configuration. Two ultra-thin fiber couplers are placed at both caustics of the bottle microresonator. Depending on its frequency, light propagating in the bus fiber is selectively coupled into the resonator mode and exits the resonator through a second ultra-thin fiber, referred to as the drop fiber. The optical powers at the output of the bus fiber $P_{\text{out}}^{\text{bus}}$ and the drop fiber $P_{\text{out}}^{\text{drop}}$ are measured using two photodiodes. The red line indicates a possible path of a light ray in the bottle microresonator.

both caustics are separated by at least 5 μm. This facilitates the use of the bottle microresonator as a four-port device in so-called "add-drop configuration". The fiber that is used to couple light into the resonator is denominated as "bus fiber". The second fiber is called "drop fiber". In this configuration, the bottle microresonator acts as a filter which frequency selectively transfers light from the bus fiber to the drop fiber. In communication technology such devices are called add-drop filters and are used for de-/multiplexing optical signals [Chu99,Ibr02]. The resonator fiber is mounted vertically (the resonator axis is rotated by 90° in the schematic in Fig. 3.3 for illustration purposes). The bus and the drop fiber can be moved independently using two positioning systems, as described above. Both ultra-thin fibers lie in the same plane perpendicular to the resonator. The angle between them can be chosen arbitrarily, taking into account the spatial constraints due to both positioning systems and the microscope objective. Figure 3.4 shows a photograph of the complete mechanical setup.
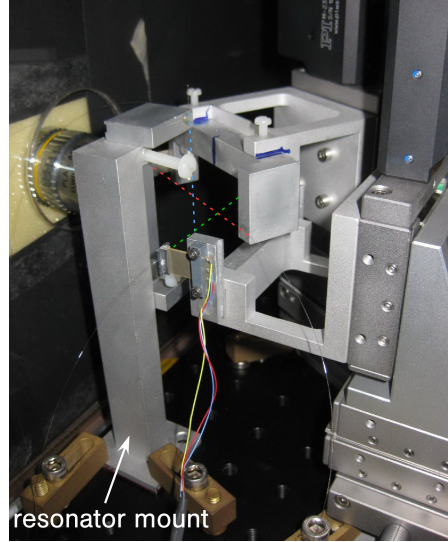
Figure 3.4: Mechanical setup used for operating a bottle microresonator in add-drop configuration. The bottle microresonator (indicated by the dashed blue line) is mounted vertically. The bus (dashed green line) and the drop fiber (dashed red line) are mounted in a plane perpendicular to the resonator axis. Each ultra-thin fiber can be manipulated using a positioning system as shown in Fig. 3.2. The picture shows a situation in which both ultra-thin fibers are moved away from the bottle microresonator.

3.1.2 Optical Components

The spatial and spectral properties of bottle modes are investigated by means of a distributed feedback (DFB) diode laser operating at a wavelength of around 850 nm with a short-term ($< 5 \ \mu$s) linewidth of 400 kHz (Toptica Photonics, DL 100 DFB 1028). The frequency of the "probe light" ν_{probe} can be tuned over 1.1 THz by modulation of the laser diode temperature T_{LD}, while fine tuning over a range of 20 GHz is achieved by modulating the input current (-3 dB modulation bandwidth of 10 kHz). A schematic of the optical setup is shown in Fig. 3.5. The laser light field at the bus fiber waist is matched to the respective bottle mode using a polarization control, consisting of a quarter- and a half-wave plate. Photodiodes monitor the power transmitted through the bus fiber and the power transferred to the drop fiber, denoted by $P_{\mathrm{out}}^{\mathrm{bus}}$ and $P_{\mathrm{out}}^{\mathrm{drop}}$, respectively. The signals of both photodiodes are recorded using a digital oscilloscope with a sampling rate up to 4 Gs/s (Agilent Technologies, MS06104A), triggered by the same arbitrary waveform generator (Agilent Technologies, 33250A) that is used to scan the laser frequency by current modulation. In order to trace ν_{probe} during a measurement, a few percent of the probe light power is split off using a half-wave plate and a polarizing beam splitter cube. This light is then sent through a reference Fabry-Pérot cavity. A photodiode monitors the transmitted power. The cavity length of 1 m corresponds to a mode spacing of 150 MHz at a wavelength of 850 nm, which thus provides a frequency scale that allows one to calibrate ν_{probe}. An acousto-optical modulator (Crystal Technology, 3200-121), operated at a frequency of 200 MHz, designated AOM in the following,
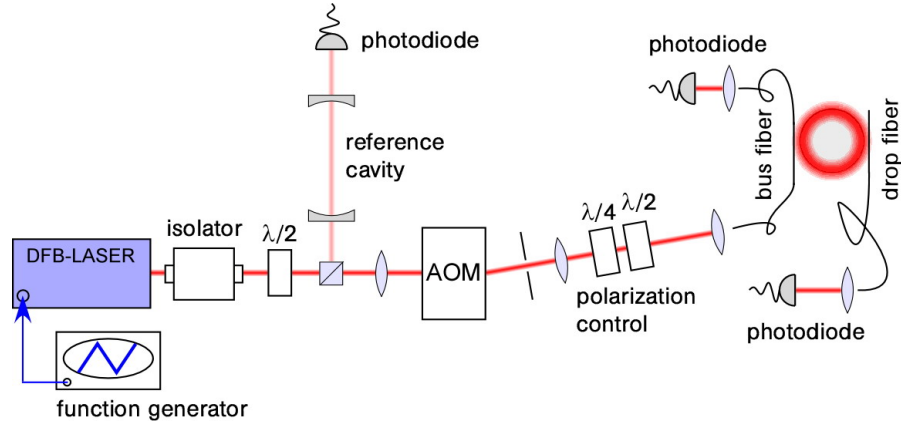
Figure 3.5: Schematic of the optical setup.

is used for fast control of the laser power coupled into the bus fiber P_{in}. By focusing the laser into the AOM crystal, it is possible to switch off the probe beam within 35 ns.

3.2 Coupling between bottle modes and ultra-thin optical fibers

In this section, a general model [Hau84] describing the transfer of optical energy between an input light field and an optical resonator is applied to the system investigated in this work. In the experimental part of this chapter the drop fiber is not used. Therefore, the theoretical discussion is limited to the case of one ultra-thin fiber coupled to a bottle mode. Nevertheless, the findings are easily transferred to a system operating in add-drop configuration. This case will be considered in the next chapter.

For the bottle microresonator the coupling between the bottle mode and the ultra-thin fiber can be tuned by adjusting the width x of the coupling gap. The influence of the width of this gap on the coupling characteristics and the quality factor of the bottle mode is discussed. It is shown that at the so-called "critical coupling point" a complete transfer of the optical power to the resonator mode is possible. Next, the deviations of the ultra-thin fiber coupler from its ideal behavior, in terms of single mode coupling characteristics and scattering losses induced by the ultra-thin fiber, is investigated. Moreover, the influence of the phenomenon of modal coupling is discussed. In WGM resonators, Rayleigh scattering can cause energy transfer between counter-propagating modes. In modes with ultra-high quality factors the transfer of energy between both modes can be much faster than the decay of the intracavity intensity. This situation is referred to as strong modal coupling. The coupling characteristics and spectral mode properties of a WGM resonator is altered in the presence of strong modal coupling.
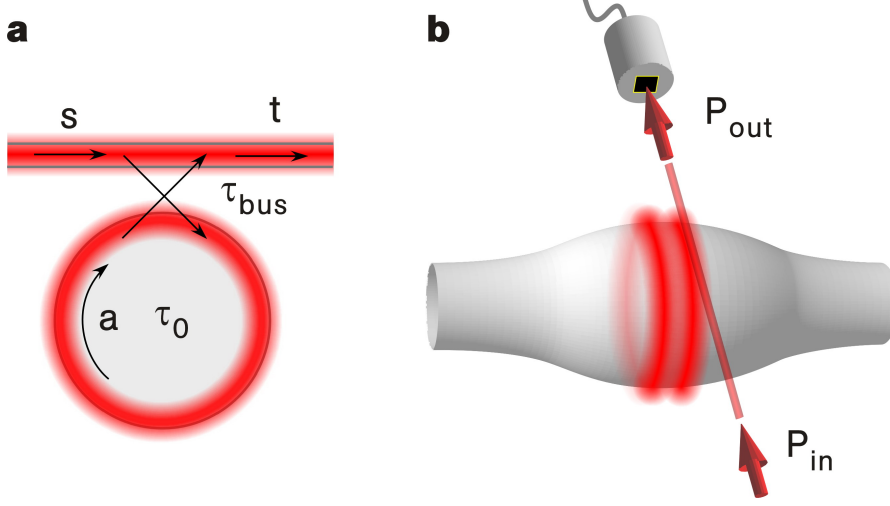
Figure 3.6: (a) The coupling junction between the bus fiber and the bottle micro-resonator can be described by a simple model using few parameters. The "mode amplitude" of the bottle microresonator is denoted by a. Whereas s and t are the "input field amplitude" and the "output field amplitude" of the waveguide. Characteristic time constants τ_{bus} and τ_0 describe the transfer of optical energy between both structures and the intrinsic resonator energy loss. (b) In the experimental characterization the power transmitted through the bus fiber $P_{\text{bus}}^{\text{out}} = |t|^2$ is measured for a given input power $P_{\text{in}} = |s|^2$ and varying width x of the coupling gap.

3.2.1 Modelling the ultra-thin fiber – resonator coupling junction

In [Hau84] a general formalism that describes the coupling of a resonator to an external light field is presented. Using this model the coupling junction between a bottle mode and the bus fiber is described using the parameters schematically indicated in Fig. 3.6. It is assumed that a bottle mode with resonance frequency $\nu_0 = \omega_0/2\pi$ is excited by a light field of frequency ω propagating on the waist of the bus fiber. The optical energy W stored in the mode of the bottle microresonator is obtained from its mode amplitude a via $W = |a|^2 = aa^*$. The transfer of optical energy between the fundamental HE_{11} mode of the bus fiber waist and the bottle mode is described by a characteristic time constant τ_{bus}. This parameter exhibits a strong dependence on the width x of the coupling gap because it is determined by the spatial overlap between the evanescent fields of both structures. Similarly, the dissipation of energy through intrinsic resonator losses like absorption or Rayleigh scattering from bulk and surface inhomogeneities is described by τ_0. The optical power incident through the bus fiber is given by $P_{\text{in}} = |s|^2 = ss^*$ using the input field amplitude s. From the output field amplitude t, the power transmitted through the bus fiber is obtained from $P_{\text{out}} = |t|^2 = tt^*$. The bus fiber transmission is defined as $P_{\text{in}}/P_{\text{out}} = |t/s|^2$. According to [Hau84] the system is then described by the following differential equation

$$\frac{d}{dt}a = i(\omega_0 - \omega)a - \frac{1}{2}\left(\tau_0^{-1} + \tau_{\text{bus}}^{-1}\right)a + \tau_{\text{bus}}^{-1/2}s \ . \tag{3.1}$$

Note that $|s|^2$ represents optical power in units J/s whereas $|a|^2$ is the optical energy given in J. The first term describes the fact that power buildup in the resonator is only possible at a discrete frequency ω_0, at which the resonance condition is fulfilled. The second term describes the decay of the mode amplitude due to intrinsic resonator losses and the presence of the bus fiber. The third term describes the coupling to the driving light field incident through the bus fiber. The exact expression describing how τ_{bus} couples a and s in the last term of the above equation, is derived in [Hau84] by using time reversibility. Next, the equation is solved in the absence of a driving light field

$$\frac{d}{dt}W = a^* \frac{d}{dt} a + a \frac{d}{dt} a^* = -\left(\tau_0^{-1} + \tau_{\text{bus}}^{-1}\right) W \ . \tag{3.2}$$

In this case, the energy stored in the resonator mode decays exponentially due to intrinsic losses and back-coupling to the bus fiber

$$W = W_0 \exp\left(-t\left(\tau_0^{-1} + \tau_{\text{bus}}^{-1}\right)\right) = W_0 \exp\left(-t/\tau_{\text{load}}\right) \ . \tag{3.3}$$

The overall time constant of the energy decay is then given by $\tau_{\text{load}}^{-1} = \tau_{\text{bus}}^{-1} + \tau_0^{-1}$ and the loaded quality factor in the presence of the bus fiber is thus given by $Q_{\text{load}} = \omega_0 \tau_{\text{load}}$. It is possible to separate the different physical effects that contribute to the loaded quality factor

$$Q_{\text{load}}^{-1} = (\omega \tau_0)^{-1} + (\omega \tau_{\text{bus}})^{-1} = Q_0^{-1} + Q_{\text{bus}}^{-1} \tag{3.4}$$

and thus to define an intrinsic quality factor Q_0 which only includes the intrinsic resonator losses. The loss mechanism with the smallest time constant will dominate Q_{load}.

The steady-state solution ($\frac{d}{dt}a = 0$) of Eq. (3.1) is easily found to be

$$a = \frac{s \ \tau_{\text{bus}}^{-1/2}}{i\left(\omega - \omega_0\right) + 1/2\left(\tau_0^{-1} + \tau_{\text{bus}}^{-1}\right)} \ . \tag{3.5}$$

As shown in Fig. 3.6, the power transmitted through the bus fiber is used to characterize the fiber coupler. Thus, in the following, an expression for the bus fiber transmission $T = |t/s|^2$ is derived. The output field amplitude t, is proportional to the cavity amplitude and the input field amplitude

$$t = c_s \cdot s + c_a \cdot a \ . \tag{3.6}$$

According to Eq. (3.2) the power escaping through the bus fiber P_{c} in the absence of a driving field ($s = 0$) and the power dissipated due to the intrinsic resonator losses P_0 are given by

$$P_{\text{c}} = \tau_{\text{bus}}^{-1} |a|^2 \quad \text{and} \quad P_0 = \tau_0^{-1} |a|^2 \ . \tag{3.7}$$

From the first of the above equations, it is apparent that $c_a = \tau_{\text{bus}}^{-1/2}$. The second equation can be used to formulate energy conservation in order to solve for c_s

$$\underbrace{|s|^2 - |t|^2}_{\text{power coupled to resonator}} = \underbrace{\frac{d}{dt}|a|^2}_{\text{energy buildup rate}} + \underbrace{\tau_0^{-1}|a|^2}_{P_0} \ . \tag{3.8}$$

Equation (3.1) is used to eliminate $\frac{d}{dt}|a|^2$ from above formula

$$\frac{d}{dt}|a|^2 = -\left(\tau_0^{-1} + \tau_{\mathrm{bus}}^{-1}\right)\,|a|^2 + \tau_{\mathrm{bus}}^{-1/2}\left(a^*s + as^*\right)\ . \tag{3.9}$$

Inserting Eq. (3.9) into Eq. (3.8) yields

$$|s|^2 - |t|^2 = -\tau_{\mathrm{bus}}^{-1}\,|a|^2 + \tau_{\mathrm{bus}}^{-1/2}\left(a^*s + as^*\right)\ . \tag{3.10}$$

Using $a = (t - c_s s)\,\tau_{bus}^{1/2}$, obtained from Eq. (3.6), yields $c_s = -1$ and thus

$$\frac{t}{s} = -1 + \tau_{\mathrm{bus}}^{-1/2}\,\frac{a}{s}\ . \tag{3.11}$$

Inserting Eq. (3.5) finally yields

$$\frac{t}{s} = \frac{1/2\left(\tau_{\mathrm{bus}}^{-1} - \tau_0^{-1}\right) - i\left(\omega - \omega_0\right)}{1/2\left(\tau_{\mathrm{bus}}^{-1} + \tau_0^{-1}\right) + i\left(\omega - \omega_0\right)}\ . \tag{3.12}$$

The transmission T, written as a function of drive frequency and fiber–resonator gap, is thus

$$T(\omega, x) = 1 - \left[1 - \left(\frac{\tau_{\mathrm{bus}}(x)^{-1} - \tau_0^{-1}}{\tau_{\mathrm{bus}}(x)^{-1} + \tau_0^{-1}}\right)^2\right]\cdot$$
$$\frac{1/4\left(\tau_{\mathrm{bus}}(x)^{-1} + \tau_0^{-1}\right)^2}{1/4\left(\tau_{\mathrm{bus}}(x)^{-1} + \tau_0^{-1}\right)^2 + (\omega - \omega_0)^2}\ . \tag{3.13}$$

As a function of the frequency of the driving field the resonance appears as a Lorentzian-shaped dip in the bus fiber transmission. Its FWHM (full width at half maximum) is $\Delta\omega = \tau_{\mathrm{bus}}^{-1} + \tau_0^{-1} = \tau_{\mathrm{load}}^{-1}$, corresponding to a spectral linewidth of $\Delta\nu = (2\pi \cdot \tau_{\mathrm{load}})^{-1}$. This means that the loaded quality factor can also be inferred from the FWHM linewidth of the resonance in the signal transmitted through the bus fiber

$$Q_{\mathrm{load}} = \omega_0 \cdot \tau_{\mathrm{load}} = \frac{\nu_0}{\Delta\nu}\ . \tag{3.14}$$

The on-resonance transmission $T_{\mathrm{res}}(x) = T\left(\omega = \omega_0, x\right)$ is given by

$$T_{\mathrm{res}}(x) = \left(\frac{\tau_{\mathrm{bus}}(x)^{-1} - \tau_0^{-1}}{\tau_{\mathrm{bus}}(x)^{-1} + \tau_0^{-1}}\right)^2\ . \tag{3.15}$$

Progressively decreasing the gap between the bus fiber and the resonator reduces τ_{bus}. This leads to a decrease in Q_{load}, which is apparent in a broadening of the Lorentzian-shaped resonance dip. Moreover, it is common to classify different coupling regimes dependent on the ratio $\tau_0/\tau_{\mathrm{bus}}$ [Cai00b].

1. **under-coupled regime**: $\tau_{\text{bus}} > \tau_0$. For a large width x of the coupling gap, for which $\tau_{\text{bus}} \gg \tau_0$, T_{res} is close to unity and increases with x. Only a fraction of the power incident through the bus fiber is transferred to the resonator, where it is dissipated.

2. **critical coupling**: $\tau_{\text{bus}} = \tau_0$. For one particular gap size the coupling time constant matches that of the intrinsic losses and the power incident through the bus fiber is completely dissipated in the resonator. The "cavity leakage field" coupling back from the resonator to the waveguide and the waveguide field transmitted past the coupling junction have equal amplitudes but a phase shift of π. The vanishing transmission can thus be understood as destructive interference of both fields with equal amplitude. The corresponding quality factor is given by

$$Q_{\text{crit}} = \frac{\omega_0 \tau_0}{2} = \frac{Q_0}{2} \ . \tag{3.16}$$

3. **over-coupled regime:** $\tau_{\text{bus}} < \tau_0$. A further reduction of the gap results in a recovery of the transmission. In this regime, the amplitude of the cavity leakage field is larger than that of the transmitted waveguide field.

In order to complete this discussion, Eq. (3.5) is used to solve for the energy stored inside the bottle mode on resonance $W_{\text{res}} = |a\,(\omega = \omega_0)|^2$ as a function of τ_0/τ_{bus}. The result is plotted in Fig. 3.7. The energy stored inside the bottle mode $W = |a|^2$ (for an arbitrary detuning $\omega - \omega_0$ and an arbitrary value of τ_{bus}) can as well be obtained from the spatial integral over the electric energy density $\mathcal{E} = n^2 \epsilon_0 |\vec{E}(\vec{r})|^2/2$ [Yar91]

$$|a|^2 = 1/2 \int_{\mathbb{R}^3} n^2 \epsilon_0 |\vec{E}(\vec{r})|^2 d\vec{r} = \frac{\epsilon_0 E_0^2}{2} \int_{\mathbb{R}^3} n^2(\vec{r}) |\vec{\Psi}(\vec{r})|^2 d\vec{r} \ . \tag{3.17}$$

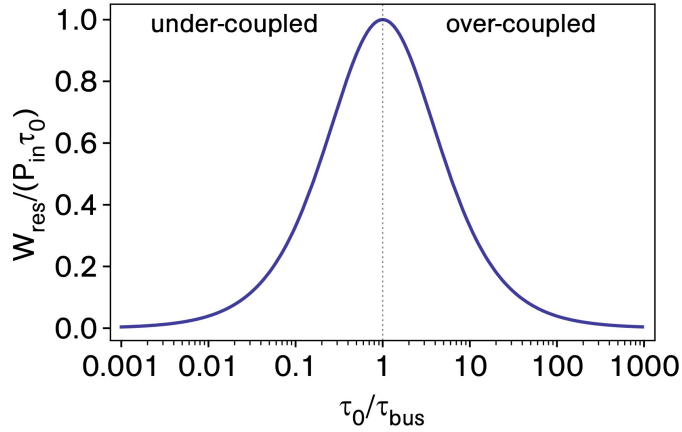**Figure 3.7:** Energy stored inside a bottle mode on resonance $W_{\text{res}} = |a\,(\omega = \omega_0)|^2$ as a function of τ_0/τ_{bus}. A maximum value of $P_{\text{in}} \cdot \tau_0$ is reached at critical coupling. This value corresponds to the power incident through the bus fiber integrated during the intrinsic energy storage time τ_0.

Here, E_0 is the peak value of the electric field strength and $\vec{\Psi}(\vec{r}) = \vec{\Phi}\left(r, z\right)) Z\left(z\right) e^{im\phi}$ is the wave function of the mode as calculated in section 2.1 with its maximum value normalized to unity. The integral of above equation is identical to the definition of the mode volume, yielding

$$|a|^2 = \epsilon_0 E_0^2 V_{m,q}/2 \ . \tag{3.18}$$

Using the relation between the electric field and the intensity $I_0 = n^2 c \epsilon_0 |E_0|^2/2$ [Hec89, Yar91] yields

$$I_0 = \frac{|a|^2 n^2 c}{V_{m,q}} \ . \tag{3.19}$$

The absolute intensity distribution of the bottle mode is given by $I(\vec{r}) = I_0 |\vec{\Psi}(\vec{r})|^2$. The peak value I_0^{crit} of the bottle mode's intensity distribution on resonance under the condition of critical coupling can now be expressed using the ratio of $Q_0/V_{m,q}$. For this purpose one inserts the value of the energy stored inside the bottle mode $|a(\omega = \omega_0)|^2 = P_{\text{in}}\tau_0$ at critical coupling, obtained from Fig. 3.7 , into equation 3.19

$$I_0^{\text{crit}} = P_{\text{in}} \frac{n^2 \lambda_0}{2\pi} \frac{Q_0}{V_{m,q}} \ . \tag{3.20}$$

3.2.2 Experimental characterization of the ultra-thin fiber coupler

The properties of the ultra-thin fiber coupler are experimentally investigated and compared with the above theoretical results. The bus fiber is placed at the caustic of a $q = 2$ bottle mode of a 36–μm diameter resonator while continuously scanning ν_{probe} over the mode's resonance frequency. By carefully adjusting x, critical coupling is realized as shown in Fig. 3.8. In a separate measurement taken on a $q = 1$ mode of a

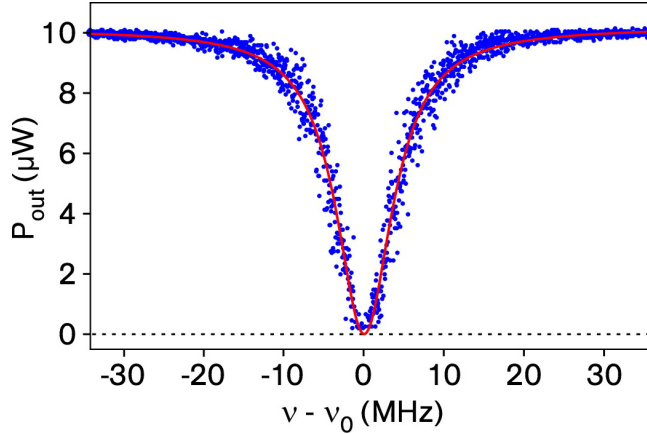**Figure 3.8:** Spectrum of a bottle mode with $q = 2$ in a 36–μm diameter resonator. A Lorentzian fit (red line) shows close agreement with the measured line shape. From the fit one obtains $\Delta\nu = 8.5$ MHz and $T_{\text{res}} < 1\%$ The measured line shape corresponds to a quality factor of $Q_{\text{crit}} = 4.1 \times 10^7$.
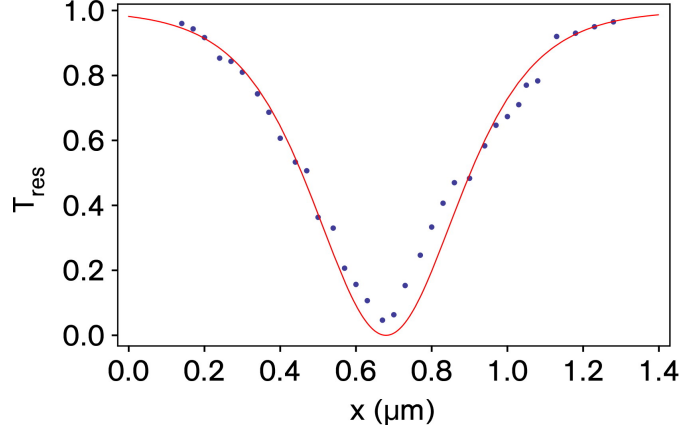
Figure 3.9: Transmission on resonance T_{res} for various values of the width x of the coupling gap. Critical coupling is achieved for $x = 680$ nm. The data shows close agreement with the theoretical prediction from the model. The measurement is taken for a $q = 1$ mode in a resonator with a diameter of 35 μm. The red line shows a fit to the data according to the model presented in previous section, assuming an exponential variation of $\tau_{\text{bus}}(x)$.

35–μm diameter resonator, x is varied while ν_{probe} is continuously swept over the resonance. Figure 3.9 shows T_{res} for various values of x ranging from 1.3 μm to the point at which the bus fiber touches the resonator due to vibrations. The latter situation can be identified by the resulting sudden drop in the off-resonant transmission. For small gap sizes, the deviation of the transmitted signal from unity becomes smaller than the noise level of the photodiode. Thus T_{res} can not be extracted from this data. The gap size is calculated from the voltage applied to the piezoelectric actuator using the manufacturers specifications, $\Delta x = \Delta U_{\text{piezo}} \cdot 0.25$ μm/V. For this bottle mode, the residual transmission at critical coupling is 4%. In fact, different modes show different values of T_{res} at critical coupling (usually smaller than 5%). A finite transmission at critical coupling can be caused by a slight mismatch of the polarizations in the fiber waist and the resonator mode. However, for modes with small $\Delta\nu$ this effect seems more pronounced. This leads to the conclusion that the finite laser linewidth contributes to this effect in a regime in which $\Delta\nu_{\text{probe}} \ll \Delta\nu$ is no longer fulfilled.

For small gap sizes in the strongly over-coupled regime, T_{res} recovers to values close to unity. From the measurement presented in Fig. 3.9 a maximum value of $T_{\text{res}} = 0.96$ is obtained in this regime. In the next section, a lower limit for the losses introduced by the coupling junction between the fiber taper and the bottle microresonator is estimated using this value.

3.2.3 Losses introduced by the ultra-thin fiber coupler

As shown above, it is possible to almost completely recover the transmission in the over-coupled regime. The light detected at the photodiode in this case is completely

transferred to the resonator and back to the coupling fiber. This shows that it is possible to enter a regime in which the coupling between the resonator mode and the fundamental mode of the fiber coupler is much stronger than the intrinsic resonator losses. Moreover, it reveals that the losses introduced by the fiber coupler itself are almost negligible. Both facts are very important when optical energy has to be transferred between two ultra-thin fiber waveguides in the filter and switching applications presented later.

Following the analysis in [Spi03], I now introduce the "coupling rate" $\kappa_{\text{bus}} = \tau_{\text{bus}}^{-1}$ which describes the coupling between the fundamental HE_{11} mode of the bus fiber and the resonator mode, the "rate of coupling to intrinsic loss channels" $\kappa_0 = \tau_0^{-1}$ and the "rate of coupling to parasitic loss channels" $\kappa_{\text{para}} = \tau_{\text{para}}^{-1}$. The physical origin of κ_{para} is, e.g., scattering at the resonator–fiber coupling junction. Another possible parasitic loss mechanism is coupling between the resonator mode and higher order waveguide modes, from which the light is lost in the tapered fiber transitions. For the experiments presented in this work, the bus fiber only sustains the fundamental HE_{11} mode. Thus, the only possible loss channel is the coupling to radiating modes by scattering at the coupling junction.

In order to gain an intuitive understanding of the coupling rates introduced above, I refer to Eq. (3.7). This equation shows that in the absence of a driving field, the power coupled from the resonator mode to a particular loss channel, characterized by a characteristic decay time τ, is proportional to τ^{-1}. It is also useful to introduce the coupling parameter K. It is defined by the ratio of coupling between the fundamental bus fiber mode and the bottle mode to the coupling to all other loss channels

$$K(x) = \frac{\kappa_{\text{bus}}(x)}{\kappa_{\text{para}}(x) + \kappa_0} \ . \tag{3.21}$$

The transmission on resonance through the bus fiber can be expressed by the coupling parameter [Spi03]

$$T_{\text{res}}(x) = \left(\frac{1-K}{1+K}\right)^2 \ . \tag{3.22}$$

In the presence of parasitic losses, the critical coupling point ($K = 1$) is shifted towards the resonator surface, where $\tau_{\text{bus}}^{-1} = \tau_0^{-1} + \tau_{\text{para}}^{-1}$ is fulfilled. By inverting Eq. (3.22) it is possible to calculate the coupling parameter from T_{res} .

$$K = \left(\frac{1 \pm \sqrt{T_{\text{res}}}}{1 \mp \sqrt{T_{\text{res}}}}\right) \ , \tag{3.23}$$

where the upper signs apply for transmissions in the over-coupled regime, whereas the lower signs apply for transmission values from the under-coupled regime. By defining

$$K^{-1} = K_I^{-1} + K_P^{-1} \ , \tag{3.24}$$

the coupling parameter can be split into an intrinsic part $K_I = \kappa_{\text{bus}}/\kappa_0$ and a parasitic part $K_P = \kappa_{\text{bus}}/\kappa_{\text{para}}$. The so-called "ideality" I quantifies the parasitic losses with respect to the coupling rate κ_{bus},

$$I(x) = \frac{\kappa_{\text{bus}}(x)}{\kappa_{\text{para}}(x) + \kappa_{\text{bus}}(x)} = \frac{1}{1 + K_P^{-1}} \ . \tag{3.25}$$
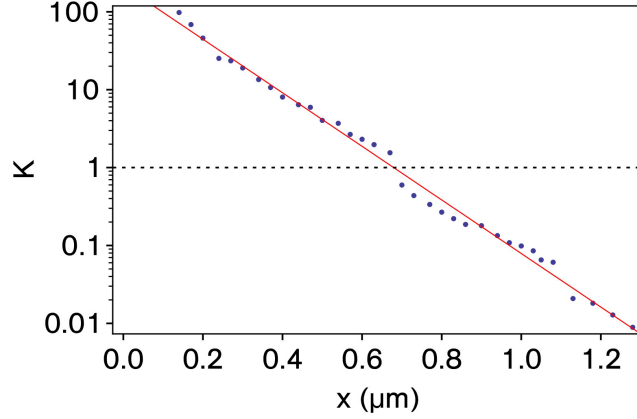
Figure 3.10: Spatial variation of the coupling parameter calculated from T_{res}. The solid line (red) is a fit of the form $K_0 \cdot \exp\left(-x/\gamma_0\right)$ with $\gamma_0 = 130$ nm. A maximum value of $K = 98$ is obtained close to the resonator surface. The horizontal dashed line indicates the critical coupling point for which $K = 1$.

For $I = 1$ the ultra-thin fiber coupler introduces no parasitic losses. Since the power coupled into the resonator mode is determined by the overlap of the exponentially decaying evanescent fields outside the resonator and the coupling fiber waist, $\kappa_{bus}(x) = \kappa_{bus}^0 \exp\left(-\gamma_0 x\right)$ is expected to decrease exponentially with x, whereas κ_0 is constant. This means that K_I also varies exponentially with x. As long as the parasitic losses are smaller than the intrinsic losses, K is dominated by K_I (as obvious from Eq. (3.24)) and $log(K(x))$ shows a linear behavior. In [Spi03] a deviation from this linear behavior was observed due to coupling to one higher order waveguide mode. Figure 3.10 shows the variation of K with the width x of the coupling gap, calculated from the measurement presented in Fig. 3.9 using Eq. (3.23). As expected from the single mode properties of the ultra-thin fiber coupler, $\log\left(K\right)$ shows no deviation from the linear behavior. In the strongly over-coupled regime K reaches a maximum value of 98, consistent with an ideality of $I \geq 0.99$. It follows that the scattering losses introduced by the coupling junction are negligible.

Finally, the overall loss rate of the light stored inside the resonator $\kappa_{\mathrm{para}} + \kappa_0$ compared to the coupling rate κ_{bus} is quantified using

$$E_{\mathrm{bc}}(x) = \frac{\kappa_{\mathrm{bus}}(x)}{\kappa_{\mathrm{para}}\left(x\right) + \kappa_0 + \kappa_{\mathrm{bus}}\left(x\right)} = \frac{1}{1 + K^{-1}} \tag{3.26}$$

In the absence of a field incident through the bus fiber this quantity can be intuitively understood as the "back-coupling efficiency", which describes the probability that a photon stored in the resonator is coupled back into the fundamental mode of the bus fiber rather than being dissipated by intrinsic or parasitic losses. Figure 3.11 shows a plot of E_{bc} as a function of the width x of the coupling gap. These results show that using a tapered fiber coupler, one can enter a regime in which the coupling between the propagating light field and the bottle mode is much larger than the intrinsic (and
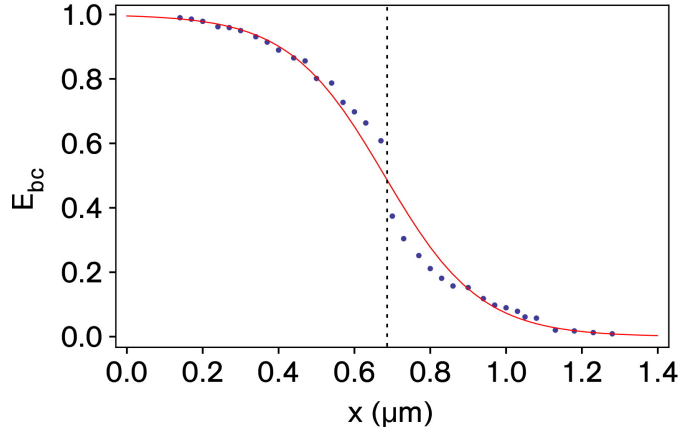
Figure 3.11: Dependency of E_{bc} on the width x of the coupling gap. In the under-coupled regime almost all of the light stored inside the mode is dissipated and E_{bc} exhibits values close to zero. For critical coupling (indicated by the vertical dashed line) a value of $E_{bc} = 0.5$ is reached. In the over-coupled regime, κ_{bus} becomes much larger than κ_0 and κ_{para} and a maximum value of $E_{bc} = 0.99$ is measured. The red line corresponds to the values obtained for K from the fit in Fig. 3.10.

parasitic) losses. This is a prerequisite for realizing highly efficient filter and switching functionalities as will be demonstrated in the next chapter.

3.2.4 Modal coupling

In WGM resonators, sub-wavelength surface inhomogeneities and refractive index fluctuations induce Rayleigh scattering. On the one hand, this phenomenon contributes to the intrinsic resonator losses and, on the other hand, it introduces a coupling between counter-propagating modes. Assuming that the light is initially coupled into a mode with quantum numbers (q, m) and a mode amplitude a_{cw}, optical energy can be transferred to the counter-propagating mode with quantum numbers $(q, m' = -m)$ and mode amplitude a_{ccw} (The indices cw and ccw stand for clockwise and counter-clockwise sense of rotation). Due to the cylindrical symmetry of the system, both modes are initially degenerate and have the same resonance frequency ω_0. They only differ in the sign of the z component of the angular momentum $m\hbar$. Mathematically, the transfer of optical energy between counter-propagating modes is described by the time constant τ_{scat}. The "mode-coupling parameter" $\Gamma = (\tau_0/\tau_{scat})$ then describes the ratio of the optical power transferred to the respective counter-propagating mode and the power that is dissipated due to intrinsic losses. Modal coupling is only observable in the regime of strong coupling of the counter-propagating modes $\Gamma \geq 1$. In analogy to the coupled harmonic oscillator model, the new eigenmodes are symmetric and antisymmetric superpositions of the initially degenerate modes with new eigenfrequencies centered around ω_0. Due to the minute Rayleigh scattering in WGM resonators, this effect is only observable for UHQ modes. A record value of $\Gamma = 31$ has been observed for an UHQ mode in a

microsphere of 30 μm diameter [Kip02]. Besides the quality factor there are many parameters that affect the modal coupling rate. The probability that a photon, scattered in an arbitrary direction, is transferred to the counter-propagating mode, is higher for resonators with smaller diameters [Kip02]. The surface roughness is the prime source of Rayleigh scattering and strongly depends on the fabrication process. Bottle microresonators typically exhibit only small modal coupling parameters. In the experiments described in the following, typically modes with $\Gamma \leq 2$ are used. Therefore, the influence of the modal coupling will be small. Nevertheless, it has to be considered in some points throughout this work. Therefore, in the following, the altered mode properties and coupling characteristics in the presence of modal coupling will be investigated according to [Hau84, Gor00, Kip02, Kip04b]. The analysis is similar to that performed above. Therefore, only the most important equations will be given. Equation (3.1) can be extended for both modes by adding a term for the inter-modal energy transfer [Kip02]. This yields two coupled differential equations for the mode amplitudes of the degenerate modes

$$\frac{d}{dt}a_{\mathrm{cw}} = i(\omega_0 - \omega)a_{\mathrm{cw}} - \frac{1}{2}\left(\tau_0^{-1} + \tau_{\mathrm{bus}}^{-1}\right)a_{\mathrm{cw}} - \frac{i}{2}\tau_{\mathrm{scat}}^{-1}a_{\mathrm{ccw}} + \tau_{\mathrm{bus}}^{-1/2}s \ , \quad (3.27)$$

$$\frac{d}{dt}a_{\mathrm{ccw}} = i(\omega_0 - \omega)a_{\mathrm{ccw}} - \frac{1}{2}\left(\tau_0^{-1} + \tau_{\mathrm{bus}}^{-1}\right)a_{\mathrm{ccw}} - \frac{i}{2}\tau_{\mathrm{scat}}^{-1}a_{\mathrm{cw}} \ . \quad (3.28)$$

Since the scattering into the respective counter-propagating mode only results in a redistribution of energy, the corresponding coefficient $i/(2\tau_{\mathrm{scat}})$ has to be purely imaginary. Using the total lifetime of photons in the resonator $\tau = \left(\tau_0^{-1} + \tau_{\mathrm{bus}}^{-1}\right)^{-1}$ the solutions in the steady-state $(da/dt = 0)$ are given by [Kip04b]

$$a_{\mathrm{cw}} = \kappa s \frac{i\left(\omega_0 - \omega\right) + \frac{1}{\tau}}{-\left(\omega_0 - \omega\right)^2 - \tau_{\mathrm{scat}}^2 + \frac{1}{\tau^2} + i\left(\omega_0 - \omega\right)\frac{1}{\tau}} \ , \quad (3.29)$$

$$a_{\mathrm{ccw}} = \kappa s \frac{-2i\tau_{\mathrm{scat}}}{-\left(\omega_0 - \omega\right)^2 - \tau_{\mathrm{scat}}^2 + \frac{1}{\tau^2} + i\left(\omega_0 - \omega\right)\frac{1}{\tau}} \ . \quad (3.30)$$

The mode amplitudes of the new symmetric and antisymmetric eigenmodes can then be constructed in the following way

$$u_s = \frac{1}{\sqrt{2}}\left(a_{\mathrm{cw}} + a_{\mathrm{ccw}}\right) \ , \quad (3.31)$$

$$u_{as} = \frac{1}{\sqrt{2}}\left(a_{\mathrm{cw}} - a_{\mathrm{ccw}}\right) \ . \quad (3.32)$$

Both eigenmodes are mutually orthogonal standing waves with an azimuthal intensity distribution proportional to $\cos\left(m\phi\right)^2$ and $\sin\left(m\phi\right)^2$ respectively. The new eigenfrequencies are

$$\omega = \omega_0 \pm \frac{1}{2\tau_{\mathrm{scat}}} \quad \mathrm{or} \quad \nu = \nu_0 \pm \frac{1}{4\pi\tau_{\mathrm{scat}}} \ . \quad (3.33)$$

Ideally, the linewidth of both eigenmodes is still given by $\Delta\omega = \tau_{\mathrm{bus}}^{-1} + \tau_0^{-1} = \tau^{-1}$, corresponding to a spectral linewidth of $\Delta\nu = (2\pi\tau)^{-1}$. However, experimentally one
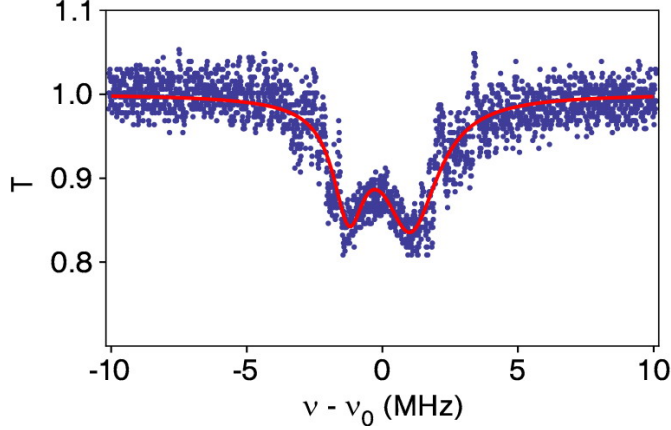
Figure 3.12: Modal coupling in a bottle microresonator. The measurement shows a $q = 1$ mode in a bottle microresonator with a diameter of 35 μm in the under-coupled regime. The fit (red line) is a superposition of two Lorentzian profiles with $\Delta\nu$ of 1.4 MHz and 2.5 MHz and a spectral separation of 2.3 MHz. The observation of distinct linewidth can be explained by the fact that both eigenmodes are mutually orthogonal standing waves. For this reason they sense different parts of the resonator surface and thus experience different losses.

often observes distinct linewidth for both modes. This observation can be understood from the mutually orthogonal azimuthal intensity distribution of the symmetric and the antisymmetric eigenmode. Both modes sense different parts of the resonator surface and therefore experience different losses. Figure 3.12 shows the typical line shape in the under-coupled regime in the presence of modal coupling measured for a 35–μm diameter bottle microresonator. The counter-propagating mode couples to the ultra-thin fiber as well. Therefore, besides the power transmitted through the fiber taper in the direction of the incident wave $|t|^2$, a certain amount of power $|r|^2$ is reflected from the coupling junction. The corresponding amplitudes are again given by the interference of the cavity leakage field and the field incident through the ultra-thin fiber, resulting in $t = -s + \tau_{\mathrm{bus}}^{-1/2} a_{\mathrm{cw}}$ and $r = \tau_{\mathrm{bus}}^{-1/2} a_{\mathrm{ccw}}$. From these quantities, the transmission T and reflectance $R = |r/s|^2$ can be calculated. A more detailed analysis [Kip02,Kip04b] shows that due to the additional losses caused by the coupling of the counter-propagating mode to the waveguide, the critical coupling point is shifted. In the absence of modal coupling, the critical coupling point is defined by $K = 1$ or $\tau_{\mathrm{bus}} = \tau_0$. However, this condition is modified for strong modal coupling

$$K_{\mathrm{crit}} = \frac{\tau_0}{\tau_{bus}} = \sqrt{1 + \Gamma^2} \quad \Rightarrow \quad \tau_{bus} = \frac{\tau_0}{\sqrt{1 + \Gamma^2}} \ . \tag{3.34}$$

This means that, in order to achieve vanishing transmission, τ_{bus} has to be reduced by moving the fiber waist closer to the resonator with respect to the situation in the absence of modal coupling.

Knowledge of τ_{crit} and τ_{scat} allows one to calculate the intrinsic quality factor [Kip04a]

$$Q_0 = \omega_0 \tau_0 = \omega_0 \frac{2}{\tau_{\text{crit}}} \left(\frac{1}{\tau_{\text{crit}}^2} - \frac{1}{\tau_{\text{scat}}^2} \right)^{-1} . \tag{3.35}$$

In the absence of modal coupling one again obtains $Q_0 = 2\omega_0\tau_{\text{crit}} = 2Q_{\text{crit}}$ which is consistent with the result from Eq. (3.16).

3.3 Spatial characterization of bottle modes

In order to characterize the spatial properties of bottle modes, an erbium-doped resonator with diameter $D_0 = (36 \pm 2)$ μm and curvature $\Delta k = (0.015 \pm 1)$ μm^{-1} is fabricated from the 50–μm diameter core of a standard Er^{3+}-doped multimode fiber (CorActive, Er637). The cladding is removed by wet etching using hydrofluoric acid. When resonantly exciting bottle modes at a wavelength around 850 nm, the erbium ions emit fluorescence light at a wavelength around 540 nm in an two-photon up-conversion process [Kli00, Cai00a]. This green fluorescence is then observed using the optical microscope. The pump light at a wavelength of 850 nm is blocked by a short-pass filter with a cutoff wavelength of 600 nm (Thorlabs, FES0600). Depending on the position of the bus fiber along the resonator axis and the laser frequency, different axial modes can be individually excited, as shown in Fig. 3.13. Due to its limited depth of focus, the microscope will only sharply image a certain part of the resonator along the direction of imaging. Therefore, using an image-processing software (CombineZM), each picture shown in the Fig. 3.13 has been generated from a stack of micrographs obtained by varying the focal plane in order to increase the effective focal depth.

For a quantitative analysis, the spatial dependency of the power emitted by the fluorescent Er^{3+} ions along the resonator axis is extracted from the figures using custom image analysis software. Figure 3.14 shows the extracted data together with the axial intensity distribution of the pump field at a wavelength of 850 nm calculated from Eq. (2.33) for the given resonator geometry. The maxima and minima of the spatial distribution of the measured fluorescence intensity are expected to coincide with the nodes and antinodes of the WGM that guides the pump light at a wavelength of 850 nm. However, the relation between pump power guided in the mode and the power emitted via fluorescence is nonlinear for an up-conversion process. Therefore, the relative hight of the distinct intensity maxima of the pump mode's axial intensity distribution is not expected to be reproduced by the data. Moreover, the nodes of the pump light's axial intensity distribution are not apparent from the measured fluorescence intensity. Possible explanations are the limited resolution of the microscope as well as reflection of the light emitted by the Er^{3+} ions at the resonator surface. For the calculation, I used the measured resonator radius R_0 = 18μm as well as $c_r = 0.97$ and $m = 180$, which are consistent with a high angular momentum WGM mode for the given radius. The position of the nodes and antinodes in the calculated intensity distribution compares best with the data for a curvature of 0.016 μm^{-1}, which is consistent with the independently measured curvature.

The results confirm the axial standing wave structure of the bottle modes by quantitatively reproducing the position of the nodes and antinodes of the resonator mode

as calculated in chapter 2.1.3. Moreover, the enhanced light intensity at the caustics is qualitatively observed. In the following, the spectral characteristics of bottle modes are investigated.
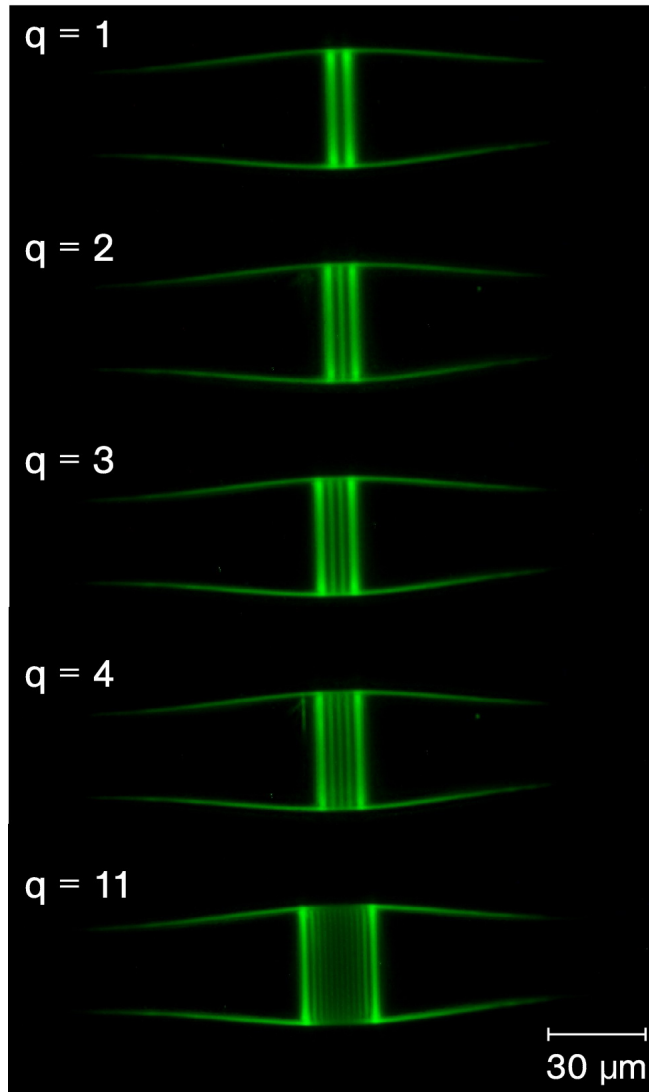
Figure 3.13: Experimental micrographs of the $q = 1$–4 and $q = 11$ bottle modes visualized via the up-converted green fluorescence of dopant erbium ions in a 36–μm diameter bottle microresonator.
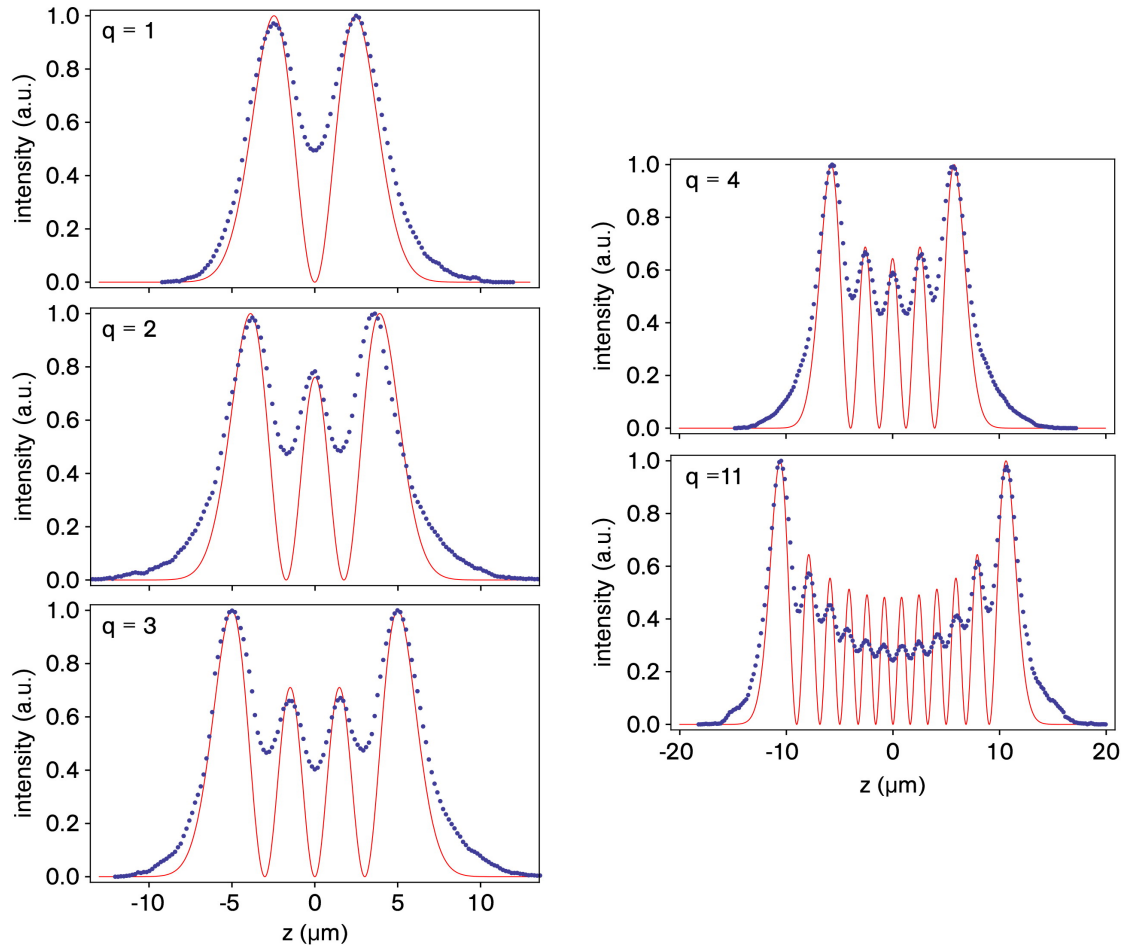
Figure 3.14: Fluorescence intensity along resonator axis (blue dots), extracted from Fig. 3.13, plotted together with the calculated intensity distribution of the mode guiding the pump light at a wavelength of 850 nm (red lines). Both intensities are normalized to unity for better comparability.

Identifying different axial modes in standard bottle microresonators. The measurements described in the following are exclusively carried out on resonators fabricated from standard silica fibers which are not doped with Er^{3+} ions. When aligning the bus fiber with the resonator and scanning the laser frequency over a certain spectral range, excitation of bottle modes is observed via the characteristic dips in the bus fiber transmission and through light scattered by surface inhomogeneities of the bottle microresonator. By moving the bus fiber along the resonator axis distinct axial modes can be excited. For a given mode the axial quantum number is determined by again translating the bus fiber along the resonator axis between both caustics of the mode, while recording the spatial modulation of the coupling efficiency. For a constant width of the coupling gap the coupling coefficient $\kappa_{bus} = \tau_{bus}^{-1}$ then varies according to the modes axial intensity distribution. A change in the coupling coefficient results in a change of the transmission on resonance T_{res}, according to Eq. (3.15). By starting in the under-coupled regime for $|z| > z_c$ the "coupling point" is shifted towards critical coupling at the modes intensity maxima and T_{res} decreases. In contrast, at the intensity nodes the transmission almost recovers to unity. The same method was used in [Lin10] to measure the polar intensity distribution of microspheres and microtoroidal resonators.

3.4 Quality factor of bottle modes

As pointed out above, a primary task of a resonator is to enhance the intensity of a light field. As apparent from Eq. (3.20), this enhancement is proportional to the ratio of quality factor to mode volume Q/V. The mode volume is given by the geometry of the resonator and is not directly accessible by measurements. It has to be calculated as described in section 2.1.4. The following section deals with the measurement of the quality factor of bottle modes and the optimization of Q/V.

Techniques for measuring the quality factor

The analysis in section 3.2.1 showed that the quality factor of a bottle mode can be either measured in the time domain or in the frequency domain. As apparent from Eq. (3.14), Q_{load} can be inferred from the temporal decay of the intracavity energy τ_{load} or from the FWHM linewidth $\Delta\nu$ of the Lorentzian-shaped resonance dip. Due to the reciprocal relation between both quantities, their combination enables the measurement of the quality factor over a wide range of magnitudes. In the following, I describe the experimental realization of these techniques.

Linewidth measurement. Since the quality factor is inversely proportional to $\Delta\nu$, measuring the latter provides a good method to determine moderate to high quality factors. For this purpose, ν_{probe} is scanned over the resonance frequency of a critically coupled bottle mode. Using a digital oscilloscope, P_{out} and the power transmitted through the reference cavity are recorded. The latter is used to calibrate the frequency scan and to plot P_{out} versus ν_{probe}. Fitting a Lorentzian to the data then yields $\Delta\nu_{load}$. For accurate measurements, some conditions have to be fulfilled:

- The observed resonance in $P_{\text{out}}^{\text{bus}}$ is obtained by a convolution of the excitation lasers spectral power density (Lorentzian with FWHM $\Delta\nu_{\text{probe}}$) and the ideal Lorentzian-shaped resonance given in Eq. (3.13). The linewidth of the resulting Lorentzian is then given by $\Delta\nu + \Delta\nu_{\text{probe}}$. Consequently, the condition $\Delta\nu_{\text{probe}} \ll \Delta\nu$ has to be fulfilled. The short-term linewidth of the laser used here, is around $\Delta\nu_{\text{probe}} \approx$ 400 kHz [War07]. For a loaded quality factor of $Q_{\text{load}} = 10^8$ the resulting error in the measured linewidth will be 10%.

- The amplitude of acoustic fluctuations in the resonance frequency of the laser resonator and the bottle mode have to be significantly smaller than $\Delta\nu$.

- The power P_{in} has to be much smaller than the threshold power of thermal bistability[1] which scales as Q^{-2}. The detectors used here require a minimum input signal of several tens of μW in order to obtain a suitable signal to noise ratio. This sets a lower limit to the linewidth (typically 1 MHz) that can be measured without distortion of the line shape.

Accordingly, these constraints make spectral measurements only reliable for quality factors smaller than $Q_{\text{load}} = 10^8$.

Cavity-ringdown measurement. For precise measurements of ultra-high quality factors, the so-called cavity-ringdown technique is used. The decay of the energy stored in the resonator in the absence of a driving field is described by Eq. (3.3). Inserting this equation into Eq. (3.7) yields the temporal decay of P_{out}

$$P_{\text{out}} = W_0 \, \tau_{\text{bus}}^{-1} \cdot \exp\left(-t/\tau_{\text{load}}\right) \;, \tag{3.36}$$

where W_0 is the energy stored in the resonator at $t = 0$. This means that by rapidly switching off the probe beam after resonant excitation of a bottle mode, it is possible to monitor the exponential decay of the intracavity energy through the output port of the bus fiber. The probe beam can be switched off within 35 ns using an AOM. Therefore, it is possible to measure $Q_{\text{load}} \geq 10^8$, corresponding to $\tau_{\text{load}} \geq 45$ ns. In order to observe the cavity-ringdown, ν_{probe} is slowly scanned over a resonance while monitoring P_{out}. The oscilloscope is triggered to the falling slope of the photodiode signal, with the trigger level set to a value corresponding only to a few percent residual transmission. When the bottle mode under investigation is resonantly excited, the oscilloscope starts the data acquisition. A special trigger output of the oscilloscope simultaneously disables the radio frequency output of the AOM's driver unit. Figure 3.15 shows the typical behavior of P_{out} in such a measurement.

---

[1] For a detailed description of thermal bistability see section 4.2.1
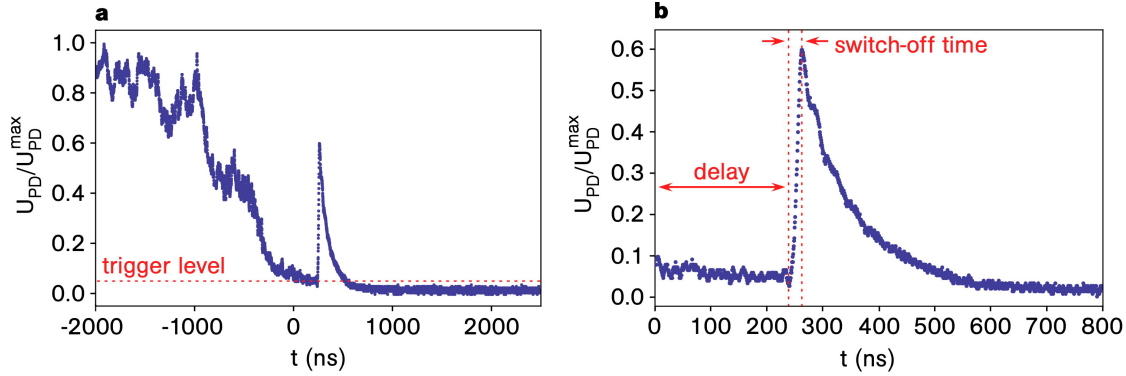
Figure 3.15: Typical cavity-ringdown measurement taken on a 38–μm diameter bottle microresonator. (a) and (b) show the signal from the photodiode measuring the power transmitted through the bus fiber with its maximum value normalized to unity for different time intervals. The frequency of the probe laser light ν_{probe} is swept over a resonance. For $t = 0$ ns the transmission reaches a value corresponding to the trigger level of the oscilloscope, indicated by the dashed line in (a). The laser power is switched off within 35 ns, see dashed lines in (b), via a TTL pulse sent by the oscilloscope to the AOM driver. The time delay of 240 ns is due to the electronics of the oscilloscope and the AOM driver and the velocity of the acoustic wave travelling in the AOM crystal. After completely switching off the probe laser power, the transmission has partially recovered and then exponentially decays to zero. At critical coupling, the waveguide field and the "cavity leakage field" destructively interfere due to their identical amplitudes and the phase-shift of π (see section 3.2.1). After completely switching off the input field, the intracavity intensity can thus be monitored via the cavity leakage field.

3.4.1 Prerequisites for ultra-high quality factors in WGM resonators

According to Eq. (3.4), the loaded quality factor is determined by the inevitable losses due to the coupling to a waveguide and due to intrinsic losses. The latter are caused by the resonator material, the resonator surface and imperfections of the total internal reflections at a curved surface

$$Q_0^{-1} = Q_{\mathrm{mat}}^{-1} + Q_{\mathrm{surface}}^{-1} + Q_{\mathrm{rad}}^{-1} \ . \tag{3.37}$$

In order to achieve highest quality factors, it is necessary to have a closer look at the origin of these intrinsic losses.

Material-related losses

The material-related losses in silica stem from absorption and Rayleigh scattering. The latter is induced by density fluctuation at a sub-micron scale. Since it is hard to distinguish these effects, the absorption coefficient α includes both effects. Silica has a minimum in its absorption coefficient at a wavelength of 1550 nm, at which both loss mechanisms contribute equally. For a shorter wavelength, the Rayleigh scattering is dominant due to its $(1/\lambda)^4$ dependence [Mes04]. For a wavelength larger than 1550 nm the losses are dominated by infrared absorption. Moreover, for a wavelength in the $1000 - 1500$ nm region, some resonances due to absorption by OH contaminants are observed. Using Lambert-Beer's law, the corresponding quality factor is given by

$$Q_{\mathrm{mat}} = \frac{2\pi n}{\alpha \lambda_0} \ . \tag{3.38}$$

This means that for resonators with $Q > 10^8$ the material absorption coefficient should be $\alpha < 0.11$ m^{-1}. Low-OH fused silica has a absorption coefficient as low as $\alpha = 4.5 \cdot 10^{-4}$ m^{-1} [Lin91]. For the fiber from which bottle microresonators are produced in this work (Newport, F-SF) the absorption is specified with 5 dB/km, which corresponds to $\alpha = 1.2 \cdot 10^{-3}$ m^{-1}. A bottle mode travels close to the surface of the resonator in a region that is formed from the outer cladding of the initial fiber. For a mode guided in a standard fiber, this part only weakly contributes to the absorption. Due to the lack of detailed insight into the manufacturing process, it is not clear that the specified value is also valid for the absorption in the outer cladding. In order to rule out the possibility of a limitation of Q by contaminations in this part of the fiber, plastic-clad fibers with a pure silica core of 200 μm diameter (CeramOptec, PWF200T) were used on a trial basis for resonator fabrication. The attenuation is specified to be around 7 dB/km at $\lambda_0 = 850$ nm, a value almost identical to that of the F-SF fiber. The cladding is stripped off and only the pure silica core is used to fabricate the resonator. No influence on the quality factor is observed. As a conclusion, other loss mechanisms should be dominant here.

Absorption-limited quality factors were observed in microspheres of very large diameter. A loaded quality factor of 8×10^9 was measured for a sphere with a diameter of 750 μm at a wavelength of 633 nm [Gor96]. In a sphere with 680 μm diameter Vernooy

et al. observed a quality factor of 7.2×10^9 at $\lambda_0 = 850$ nm [Ver98a]. In order to obtain high Q/V, however, one has to fabricate resonators with a much smaller diameters. For smaller resonator diameters, the electric field strength at the resonator surface becomes more and more pronounced and surface-related loss mechanisms begin to dominate the quality factor.

Surface-related losses

For resonator diameters below 50 μm, surface effects like scattering at surface inhomo-geneities and water adsorption, as well as surface contamination by dust particles have a significant effect on the overall intrinsic quality factor. In [Kip04a], a strong decrease in the quality factor was observed for microtoroidal resonators fabricated with diameters below 35 μm. In microspheres and microtoroidal resonators a very low surfaces roughness is achieved due to the production process, in which the material forming the resonator is first heated beyond the melting point and then solidifies forming a very smooth surface. Atomic force microscopy reveals a rms surface roughness of 2 nm measured over a 20 nm square for a microsphere [Ver98a]. For bottle microresonators the fabrication process is somewhat different. During the fabrication, the material is only heated to a point at which its viscosity is low enough to allow deformation because the cylindrical shape of the fiber would not be stable if the material was heated to the melting point. For some resonators a post-annealing step is added after fabrication. During this step, the resonator temperature is increased to a temperature close to the melting point, for which the resonator starts to deform and slightly increase in curvature due to surface tension (also see section 2.3.2). However, no influence on the quality factor was observed. In [Gor96] a rapid drop in the quality factor as well as a shift in resonance frequency in the first 5 minutes after fabrication were measured. This process shows the characteristic time scale of hydration, a chemical process in which OH groups are chemically bound to a SiO_2 surface [Ada77, Bur90]. A further degradation in the quality factor within 20–30 min after production is referred to adsorption of atmospheric water at the hydrated surface. In this work, no measurements of the quality factor for times shorter than 30 min after production are performed. A degradation of the quality factor at a time scale of some hours up to few days is observed when the resonator is kept under ambient conditions. By setting up the experiment in a laminar flow box (Spetec, FBS24) it is possible to maintain UHQs for many weeks. The class H14 filter of the laminar flow box provides a filter efficiency of 99.995% for particles with diameters larger than 120 nm.

Radiative loss

The total internal reflection that occurs at a curved surface is not lossless. As already pointed out in section 2.1.2, the form of the effective radial potential of the bottle microresonator V_{eff} gives rise to a propagating field for radii beyond R_{rad}, see Eq. (2.24). The evanescent field leaking out of the resonator couples the WGM to propagating light fields, causing radiative losses. A quantitative analysis [Dat92, Buc03] found that Q_{rad}

decreases approximately exponentially with the resonator diameter. For a wavelength of 852 nm and a resonator diameter of 30 μm, Q_{rad} is as high as 2×10^{21}, and for a resonator with 14 μm diameter, Q_{rad} only decreases to 4×10^8. Both values are several orders of magnitude higher than what is experimentally observed for the corresponding diameter because absorption and surface-related losses dominate the quality factor by far.

3.4.2 State of the art $-$ Q/V in microresonators

This section gives an overview of the values of Q/V achieved in different microresonators. The highest values to date have been observed in microtoroidal resonators and in photonic crystal cavities. In most publications, the value of Q_0/V is stated. In view of possible applications the value of Q_{crit}/V or Q_{load}/V is a more meaningful quantity and will therefore be considered here, as far as possible. In WGM resonators it is often desirable to work under the condition of critical coupling which results in a maximum of the intracavity intensity and vanishing bus fiber transmission. Photonic crystal cavities and Fabry-Pérot microresonators lack the possibility of flexibly adjusting the coupling rate and are mostly operated in the under-coupled regime. For these structures, the value Q_{load}/V will be considered, even though a precise comparison is difficult.

WGM resonators. One of the highest values of Q/V to date have been realized in WGM resonators. An intrinsic quality factor of $Q_0 = 4 \times 10^8$ was obtained by a cavity-ringdown measurement in a microtoroidal resonator with a diameter of 29 μm at a wavelength of $\lambda = 1550$ nm. For these cavity dimensions, the mode volume was calculated to be $V = 180 \, \mu\mathrm{m}^3$ [Kip04a]. A typical value of the mode-coupling parameter for microtoroidal resonators with these dimensions is $\Gamma \approx 30$ [Kip04a]. The loaded quality factor at critical coupling would thus reduce to $Q_{\mathrm{crit}} = 1.2 \times 10^7$. This results in an value of $Q_0/V = 2.5 \times 10^6 \, (\lambda/n)^{-3}$ which reduces to $Q_{\mathrm{crit}}/V = 7.5 \times 10^4 \, (\lambda/n)^{-3}$ in the case of critical coupling.

Photonic crystals. Photonic crystal cavities confine light to volumes near the fundamental limit on the order of λ^3. To date, only moderate quality factors in the 10^5 – 10^6 range have been observed for such ultra-small mode volume devices [Wei06, Asa06, Tan07]. A photonic crystal cavity with a mode volume as small as $V = 1.7 \, (\lambda/n)^3$ and a quality factor of $Q_{\mathrm{load}} = 1.2 \times 10^6$ has been demonstrated in [Tan07]. A value of $Q_0 = 1.3 \times 10^6$ for the intrinsic quality factor of the cavity was stated, indicating that the measurement of Q_{load} was taken in the strongly under-coupled regime. The cavity design is based on a two-dimensional photonic crystal slab in which a line defect serves as a waveguide. Implementation of the cavity is achieved by local width modulation of the line defect. Above values correspond to a ratio of $Q_{\mathrm{load}}/V = 7.1 \times 10^5 \, (\lambda/n)^{-3}$, which, to my knowledge, is the highest observed in a photonic crystal cavity to date. The performance of photonic crystals in terms of the ratio Q/V is therefore comparable with microtoroidal resonators.

Fabry-Pérot microresonators. The mode volume of a Fabry-Pérot resonator depends on the distance between the mirrors and can thus be significantly diminished by decreasing the latter. However, the quality factor roughly scales with this distance. In [Hoo00] a Fabry-Pérot resonator with an optimized ratio of Q/V is used. The cavity had a length of 10.9 μm and a beam waist of $w_0 = 14$ μm. For a wavelength of $\lambda = 852$ nm, $V = 1680$ μm^3 and $Q = 1.2 \times 10^7$ are achieved. This results in a ratio of $Q/V = 4400$ $(\lambda/n)^{-3}$ which is 1–2 orders of magnitude smaller than the values reported for microtoroidal resonators and photonic crystal cavities.

Bottle microresonators. Previous experimental work has demonstrated that bottle microresonators are readily fabricated from standard optical glass fibers [Kak01, War06, Poe06, War07, Mur09]. In [Kak01, War06, Poe06, War07] the values for D_0 ranged from 12 μm to 16 μm . Theoretically, these dimensions should be large enough to avoid radiative losses and thus to reach Q factors in the 10^7–10^9 range [Buc03]. However, the experimentally observed Q factors were smaller than 10^4 in [Kak01]. In [Poe06, War07] the highest measured quality factor was around 4×10^5 in the under-coupled regime. In [Mur09] a bottle microresonator with a diameter of 185 μm was fabricated from a 125–μm diameter fiber using the arc discharge of a fusion splicer to heat the fiber. The bulge forming the bottle microresonator is created by simultaneously heating and compressing the fiber. Despite the large diameter, this resonator yielded quality factors not exceeding 5×10^5. Due to their small quality factors along with moderate mode volumes, the bottle microresonators realized prior to the work presented here were not compatible with microtoroidal resonators and photonic crystal cavities in terms of Q/V.

3.4.3 Experimental results – UHQ in bottle microresonators

In this work, ultra-high quality factors are measured for bottle microresonators fabricated using the technique presented in section 2.3.2 and using the setup described in section 3.1 in combination with the cavity-ringdown technique described above. The polarization of the mode under investigation can be obtained by investigating its frequency tuning characteristics. When applying a mechanical strain σ to the resonator two classes of modes are observed that show different tuning speeds $\Delta\nu/\sigma$. The tuning characteristics for modes of different polarizations is discussed in section 3.5.1. Figure 3.16 shows the ringdown measurement taken on a TE polarized mode with an axial quantum number of $q = 1$ in a resonator with a diameter of $D_0 = 35$ μm and a curvature of $\Delta k = 0.012$ μm^{-1}. The ringdown time constant $\tau_{\mathrm{crit}} = (82\pm0.45)$ ns directly yields $Q_{\mathrm{crit}} = (1.8\pm0.01)\times10^8$. Using Eq. (3.35), one obtains $Q_0 = (3.6 \pm 0.02) \times 10^8$ for the negligible modal splitting observed for this mode. This ultra-high intrinsic quality factor is comparable to the values reported for microtoroidal resonators of the same diameter [Kip04a]. At critical coupling, the quality factor measured here is about one order of magnitude larger than the corresponding value for microtoroidal resonators [Kip04a].

As described in section 3.4.1, the influence of different parameters on the quality factor, e.g., material and fabrication technique, have been investigated. The only parameter that significantly affects the quality factor is the resonator diameter. Figure 3.17 shows
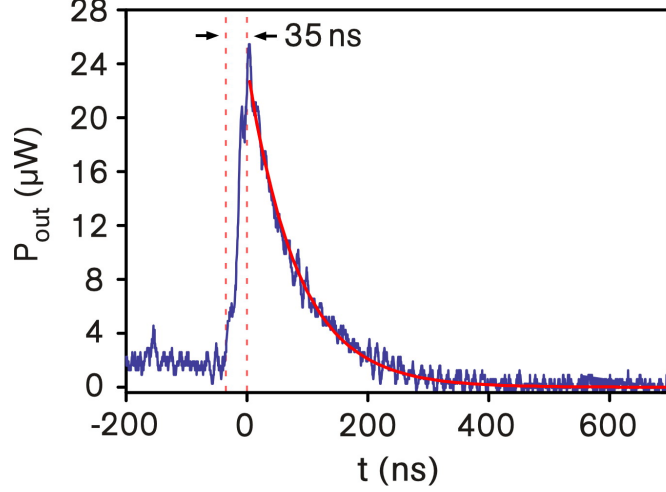
Figure 3.16: Cavity-ringdown measurement of the $q = 1$ bottle mode in a bottle microresonator with a diameter of 35 μm and a curvature of $\Delta k = 0.012$ μm^{-1}. The measurement was performed at critical coupling for a wavelength near 850 nm and transverse electric (TE) polarization. The exponential fit (red line) according to Eq. (3.36) yields $\tau_{\mathrm{crit}} = (82 \pm 0.45)$ ns.

Q_{crit} for D_0 ranging from 16 μm to 105 μm. For resonator diameters below 35μm the quality factor decreases rapidly, whereas for larger diameters it is almost constant. The highest value of $Q_{\mathrm{crit}} = 2.9 \times 10^8$ is measured for $D_0 = 105$ μm. This observation is in agreement with the results obtained with microtoroidal resonators [Kip04a].

Optimizing Q/V

Next, Q_{crit}/V is analyzed for the various resonator diameters used in Fig. 3.17. The mode volume is calculated according to section 2.1.4 using the same parameters ($\Delta k = 0.012$ μm^{-1} and $q = 1$) as for the 35–μm diameter resonator on which the measurement presented in Fig. 3.16 was carried out. The calculated mode volume as well as Q_{crit}/V are shown in Fig. 3.18. According to this analysis optimal ratios of Q_{crit}/V are expected for diameters in the range of 35–45 μm. For $D_0 < 35$ μm, Q_{crit}/V is governed by the rapid decrease of Q_{crit}. For larger diameters, the mode volume slowly increases, thus leading to a decrease in Q_{crit}/V. The $q = 1$ mode in the $D_0 = 35$ μm resonator for which the UHQ was measured in Fig. 3.16 exhibits Q_{crit}/V of 3.0×10^4 $(\lambda/n)^{-3}$. For comparison, this is about one order of magnitude smaller than the value of Q_{load}/V obtained for the photonic crystal cavity in [Tan07] (which is measured in the strongly under-coupled regime) and only about a factor of two smaller than the value for Q_{crit}/V observed in microtoroidal resonators [Kip04a].
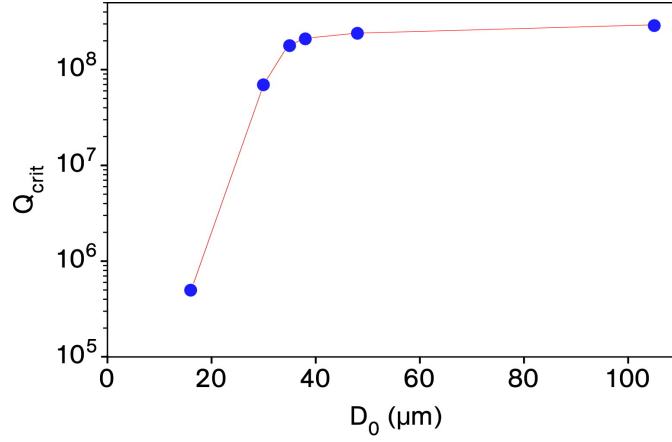
Figure 3.17: Quality factor Q_{crit} as a function of resonator diameter D_0. For resonator diameters ranging from $30 - 105$ μm, ultra-high quality factors are measured using a cavity-ringdown technique. Due to the small errors on the order of 0.5%, no error bars are shown. The quality factor of 4×10^5 for $D_0 = 16$ μm is inferred from the linewidth of the mode. The red line is a guide to the eye. Modes with varying axial quantum numbers in resonators with different curvatures of the resonator profile were used. However, for a given resonator diameter, a dependency of the quality factor on the axial quantum number and on the curvature of the resonator profile is not observed.
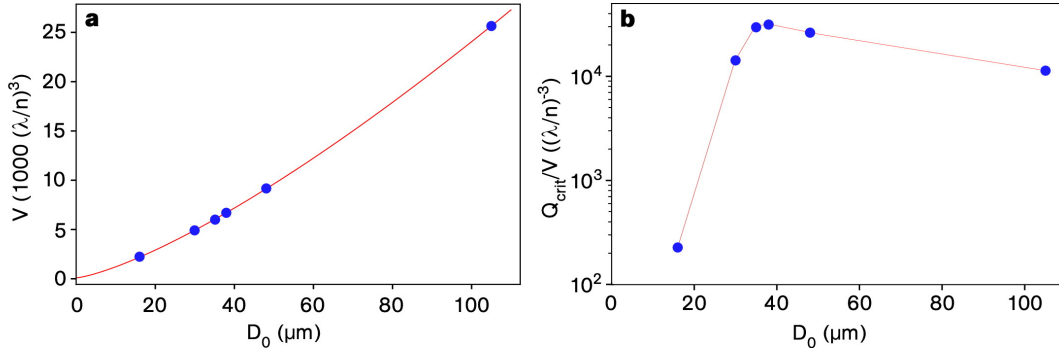
Figure 3.18: (a) Calculated mode volumes for different resonator diameters. The calculation assumed TE polarization, an axial quantum number of $q = 1$ and a curvature of $\Delta k = 0.012$ μm^{-1}. (b) Q_{crit}/V obtained from the calculated mode volumes shown in (a) and the radial dependency of Q_{crit} presented in Fig. 3.17.

3.5 Tunability of bottle modes

In this section, the tunability of UHQ bottle modes is investigated. Tunability is a critical issue in applications which require the coupling of light of an arbitrary, predetermined frequency into a mode of the resonator. As an example, in CQED experiments the resonance frequency of a UHQ bottle mode has to be matched to an atomic transition frequency.

3.5.1 Fundamentals of tuning the resonance frequency of bottle modes

By changing the optical path length of the resonator, it is possible to shift the resonance frequency ν_0 by $\Delta\nu_0$. The optical path length depends on the resonator geometry and the refractive index. In the following analysis, the curvature of the resonator is neglected and it is treated as a cylinder of Radius R_0. The frequency shift that corresponds to a change Δn in the refractive index and a change ΔR in the resonator radius is then given by [Lon03]

$$\frac{\Delta\nu_0}{\nu_0} \approx -\frac{\Delta R}{R_0} - \frac{\Delta n}{n} \ . \tag{3.39}$$

There are two principle methods of tuning the resonance frequency. They are discussed in the following.

Thermo-optic tuning. Due to the thermo-optical effect, the refractive index of the resonator material depends on its temperature. Silica exhibits a relatively small thermo-optic coefficient of $\partial n/\partial T \approx 1.3 \cdot 10^{-5} K^{-1}$ [Lon03]. Changing the temperature of the resonator material by 1 K will thus only change the resonance frequency by $\Delta\nu_0/\nu_0 = -9 \times 10^{-6}$, i.e, by 9 ppm of the optical frequency.

Elasto-optic tuning. Applying mechanical strain to the resonator fiber changes the resonator radius as well as the refractive index. The Poisson coefficient σ describes the relation between lateral contraction $\Delta R/R_0$ and relative length change $\Delta L/L$ of the resonator fiber

$$\frac{\Delta R}{R_0} = -\sigma \cdot \frac{\Delta L}{L} \ , \tag{3.40}$$

where the Poisson coefficient for silica is $\sigma_{SiO_2} = 0.17$ [Bor68].

The refractive index change experienced by a glass fiber due to a force along its axis is calculated using the elasto-optic tensor. For TM modes, the light field exhibits parallel polarization with respect to the strain applied. Using the components $p_{11} = 0.126$ and $p_{12} = 0.26$ of the elasto-optic tensor [Bor68] the relative change in refractive index is given by

$$\frac{\Delta n}{n} = -\frac{n^2}{2} \left(p_{11} - 2\sigma p_{12} \right) \frac{\Delta L}{L} = -0.04 \cdot \frac{\Delta L}{L} \ . \tag{3.41}$$

For TE polarization, one obtains, in the same way, $\Delta n/n = -0,14 \cdot (\Delta L/L)$ [Lon03]. The overall relative change in resonance frequency for both polarizations is then given

by

$$
\begin{aligned}
\text{TM:} \quad & \frac{\Delta\nu_0}{\nu_0} = 0.21 \cdot \frac{\Delta L}{L} \ , \\
\text{TE:} \quad & \frac{\Delta\nu_0}{\nu_0} = 0.31 \cdot \frac{\Delta L}{L} \ .
\end{aligned}
\tag{3.42}
$$

Strain tuning is only possible within the elastic regime of silica. Hooke's law relates the relative length change to the applied strain ϵ, via the modulus of elasticity,

$$
\epsilon = E_{\text{Si0}_2} \cdot \frac{\Delta L}{L} \ .
\tag{3.43}
$$

For silica the latter takes a value of $E_{\text{Si0}_2} = 72$ GPa. The strain is calculated by the force applied by the piezo-electric actuator divided by the cross-section of the resonator structure. Silica's typical damage threshold of 3 GPa [Gla91], sets the maximum applicable relative length change to $\Delta L/L = 0.042$ and therefore should in principle allow one to tune the resonance frequency by 1.3% of the optical frequency, i.e., 4.5 THz.

3.5.2 State of the art – tuning WGM resonators

While equatorial WGMs, like microtoroidal resonators and microspheres, have the advantage of having small mode volumes, they also exhibit a large frequency spacing between consecutive modes. In small WGM resonators, the azimuthal free spectral range is typically very large. According to section 2.1.4, changing m by one for a 35–μm diameter WGM changes its resonance frequency by $\Delta\nu_m \approx 1.9$ THz, i.e., about one percent of the optical frequency. Due to its monolithic design, tuning a WGM microresonator over such a large range is a critical issue. Electrical thermo-optic tuning of equatorial WGMs in a 75–μm diameter microtoroidal resonator over more than 300 GHz has been demonstrated [Arm04] for a wavelength of 1550 nm. This corresponds to 35% of the azimuthal FSR and to 0.15% of the optical frequency. Using a strain tuning technique, tuning over 400 GHz for $\lambda = 800$ nm has been demonstrated for a 80–μm diameter microsphere, limited by the mechanical damage threshold of the resonator [Kli01]. This corresponds to 50% of the azimuthal FSR and 0.12% of the optical frequency. Recently, strain-tuning of a so-called "microbubble resonator" with a diameter of 200 μm over 690 GHz has been demonstrated [Sum10b]. For a wavelength of 1550 nm, this corresponds to 2.2 azimuthal FSRs. Microbubble resonators consist of a bulge on a microcapillary created from a silica tube [Sum10a]. Due to the small wall thickness in the section forming the resonator, which is on the order of 1–2 μm, mechanical strain can be applied very efficiently to this structure, leading to the impressive frequency shift of 0.35% of the optical frequency. Unfortunately, the azimuthal FSR is only smaller than the demonstrated tuning range for microbubble resonator of diameters larger than 90 μm. Moreover, the highest quality factor achieved in these structures is 1.5×10^6. Therefore, these resonators are not suitable for applications for which high Q/V-ratios are required.

In summary, fully tunability of whispering-gallery modes combining ultra-high quality factors and small mode volumes has not been achieved prior to the work presented here.
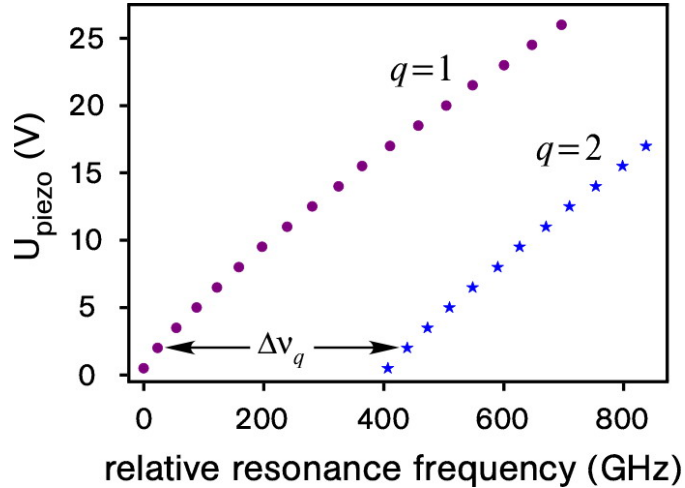
Figure 3.19: Tuning the bottle microresonator. Using a piezo-electric actuator to elastically elongate a bottle microresonator of 35 μm diameter and $\Delta k = 0.012 \ \mu\mathrm{m}^{-1}$, the TE polarized $q = 1$ and $q = 2$ bottle modes are strain-tuned. The tuning range of 700 GHz of the $q = 1$ mode exceeds the observed axial FSR of $\Delta\nu_q = 425 \pm 8$ GHz.

3.5.3 Experimental results – tuning an UHQ bottle microresonator

The bottle microresonator offers a solution for the problem described above. According to Eq. (2.38), its axial FSR only depends on the curvature of the resonator profile and can thus be made much smaller than its azimuthal FSR without significantly affecting the mode volume. It is therefore sufficient to tune the bottle microresonator over one axial FSR in order to ensure that an arbitrary predetermined frequency will coincide with the resonance frequency of an appropriately chosen bottle mode. However, in order to keep the mode volume small it is desirable to work with a low axial quantum number q, thereby minimizing the separation between the two caustics. In the following, tuning of a bottle mode over one axial FSR is presented in a 35–μm diameter resonator with a curvature of $\Delta k = 0.012 \ \mu\mathrm{m}^{-1}$. Based on this measurement, I then introduce a tuning scheme that enables tuning of the bottle microresonator to any arbitrary frequency by bridging the azimuthal FSR using a set of lowest order axial bottle modes.

Strain tuning of a bottle mode over one axial FSR is demonstrated using the setup described in section 3.1. The measurement, presented in Fig. 3.19, is carried out with the same $q = 1$ mode which yielded the UHQ in Fig. 3.16. The resonance frequencies of the TE polarized $q = 1$ and $q = 2$ bottle modes are measured for varying mechanical strain. For this purpose, the bus fiber transmission in a small spectral region is continuously monitored by rapidly scanning the laser current. The spectral positions of both modes are then identified by manually scanning the laser over the whole tuning range by means of the laser diode temperature T_{LD}. Next, U_{piezo} is stepwise increased by 0.5 V. For each voltage increment, the temperature change of the laser diode that is necessary to compensate for the induced shift in the resonance frequency is measured. The reference cavity is used to calibrate ν_{probe} as a function of T_{LD}. The results are shown in Fig. 3.19.

The observed tuning range of 700 GHz is 1.6 times larger than the measured axial FSR of $\Delta\nu_q = (425 \pm 8)$ GHz. This corresponds to a frequency shift of 0.2% of the optical frequency. The experimentally measured axial FSR of $\Delta\nu_q = (425 \pm 8)$ GHz is in close agreement with the theoretical value of (391 ± 33) GHz, calculated from the measured curvature of the resonator profile using Eq. (2.38). The maximum strain applied to the resonator in this measurement, limited by the travel range of the bending actuator, can be inferred from the frequency shift using Eq. (3.42) and Hooke's law and is about 15% of the typical damage threshold of silica. Figure 3.20 schematically illustrates tuning of the examined UHQ bottle microresonator to an arbitrary frequency using only the four lowest order axial bottle modes.

3.6 Conclusion

To summarize, in this chapter the first experimental realization of bottle microresonators exhibiting ultra-high quality factors is presented. In conjunction with the mode volumes calculated in section 2.1.4, this results in ratios of Q_{crit}/V that align with the highest values reported from other types of microresonators. Tuning of bottle modes which combine ultra-high quality factors and small mode volumes to an arbitrary, predetermined frequency has been demonstrated for the first time in monolithic microresonators. Moreover, the coupling characteristics between a bottle microresonator and an ultra-thin fiber coupler have been investigated. The nearly lossless coupling mechanism enables highly efficient light transfer into and out of the bottle modes. By changing the gap between the ultra-thin fiber and the bottle microresonator, the coupling rate can be varied with high flexibility. At the critical coupling point, the light field launched into the ultra-thin fiber is completely transferred to the bottle mode. Moreover, by further decreasing the coupling gap, it is possible to enter a regime in which the coupling between the ultra-thin fiber and the bottle mode dominates the intrinsic losses of the mode. This is a prerequisite for realizing highly efficient filter functionality, as will be demonstrated in the following chapter.
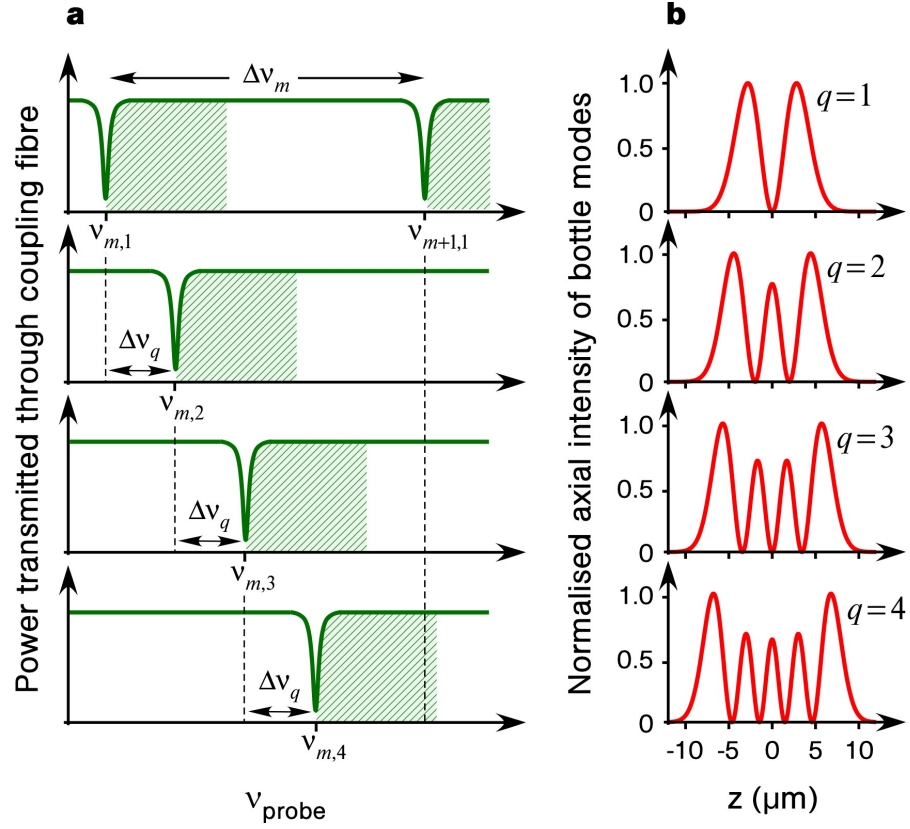
Figure 3.20: Bottle microresonator tuning scheme for the resonator with $D_0 = 35$ μm and $\Delta k = 0.012$ μm^{-1}, for which tuning over one axial FSR was demonstrated in Fig. 3.19. For this resonator dimensions $\Delta\nu_m = 1.9$ THz is calculated to be five times larger than the measured value of $\Delta\nu_q = 425$ GHz. (a) Assuming the measured tuning range (indicated by the green shaded areas) of 700 GHz, the $q = 1 - 4$ bottle modes allow one to fully bridge the azimuthal FSR of the bottle microresonator. This makes any arbitrary frequency accessible by strain tuning the nearest mode with $q = 1 - 4$ and m properly chosen. (b) Calculated axial intensity distribution of the TE polarized $q = 1 - 4$ bottle modes for the resonator dimensions given above. These modes exhibit the smallest possible separation between the two caustics and thus yield the smallest mode volumes ranging from 1180 μm^3 to 1470 μm^3 for a wavelength of $\lambda = 850$ nm.

4 From high efficiency add-drop filters to all-optical switches

This chapter starts with an experimental examination of the performance of the bottle microresonator in add-drop configuration. Next, the nonlinear properties of the bottle resonator in this configuration are characterized. Due to the third-order susceptibility, $\chi^{(3)}$, of silica, the refractive index of the resonator material depends on the intracavity intensity I via the Kerr effect $n = n + n_2 \times I$, where $n_2 \propto \chi^{(3)}$ is the nonlinear refractive index. A variation of the intracavity intensity then modifies the optical path length of the cavity and thus changes the transmission properties of the microresonator. This effect is often used in the field of "all-optical switching", i.e., the control or redirection of the flow of light using a second light field. For a given input power, the nonlinear shift of the resonance frequency in units of the resonator linewidth is proportional to $n_2 Q^2 / V$. Therefore the power at which switching occurs is proportional to $V/(n_2 Q^2)$. The advantageous combination of a moderate value of n_2 and a very low absorption coefficient in silica allows one to observe all-optical switching at record-low powers in bottle microresonators. Finally, it is shown that the same set-up can also be operated for all-optical routing and as an optical memory.

4.1 High efficiency narrow-band add-drop filter

In this section, the linear optical properties of the bottle microresonator coupled to two ultra-thin fibers, as shown in Fig. 3.3, are examined.

4.1.1 Model – a bottle microresonators coupled to two ultra-thin optical fibers

In order to describe the power transfer between the bus and the drop fiber, the model of the resonator–fiber coupling junction, presented in chapter 3.2.1 is extended according to Fig. 4.1. The system is then described by the following equation [Hau84]

$$\frac{d}{dt}a = i\left(\omega_0 - \omega\right)a - \frac{1}{2}\left(\tau_0^{-1} + \tau_{\text{bus}}^{-1} + \tau_{\text{drop}}^{-1}\right)a + \tau_{\text{bus}}^{-1/2}s \ . \tag{4.1}$$

In this case, the loaded quality factor is given by

$$Q_{\text{load}}^{-1} = Q_0^{-1} + Q_{\text{bus}}^{-1} + Q_{\text{drop}}^{-1} = 1/\left(\omega_0 \tau_0\right) + 1/\left(\omega_0 \tau_{\text{bus}}\right) + 1/\left(\omega_0 \tau_{\text{drop}}\right) \ . \tag{4.2}$$

The power optical power at the output of the drop fiber $P_{\text{out}}^{\text{drop}} = |e|^2$ is given by the square of the output field amplitude. In analogy to the previous analysis, one derives
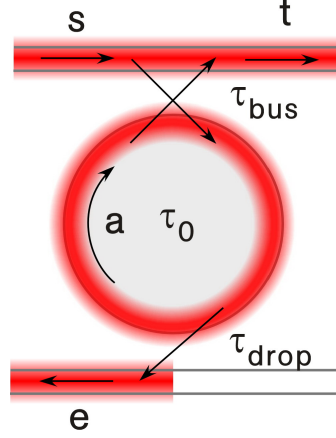
Figure 4.1: A bottle microresonator, coupled to two ultra-thin fibers. The model described in section 3.2.1 is extended by introducing two parameters accounting for the influence of the drop fiber. Its "output field amplitude" is denoted by e and the time constant of the energy transfer between the resonator mode and the drop fiber is τ_{drop}.

the "normalized output amplitudes" at both fiber outputs as

$$\frac{e}{s} = \tau_{\mathrm{drop}}^{-1/2}\frac{a}{s} = \frac{\left(\tau_{\mathrm{drop}}\cdot\tau_{\mathrm{bus}}\right)^{-1/2}}{1/2\left(\tau_{\mathrm{bus}}^{-1}+\tau_0^{-1}+\tau_{\mathrm{drop}}^{-1}\right)+i\left(\omega-\omega_0\right)} \tag{4.3}$$

and

$$\frac{t}{s} = \frac{1/2\left(\tau_{\mathrm{bus}}^{-1}-\tau_0^{-1}-\tau_{\mathrm{drop}}^{-1}\right)-i\left(\omega-\omega_0\right)}{1/2\left(\tau_{\mathrm{bus}}^{-1}+\tau_0^{-1}+\tau_{\mathrm{drop}}^{-1}\right)+i\left(\omega-\omega_0\right)} \ . \tag{4.4}$$

The transmitted and the dropped powers normalized to the input intensity are calculated from $T = |t/s|^2$ and $D = P_{\mathrm{out}}^{\mathrm{drop}}/P_{\mathrm{in}} = |e/s|^2$. Both quantities are related via the ratio of the intrinsic loss rate to the drop fiber coupling rate [Rok04]

$$\left(1+Q_{\mathrm{drop}}/Q_0\right)D = 1-T \ , \tag{4.5}$$

meaning that in order to achieve efficient power transfer between the fibers, the light has to be coupled into the drop fiber much faster than it is dissipated inside the resonator. The highest transfer efficiency between the bus and the drop fiber is obtained for critical coupling, defined by

$$\tau_{\mathrm{bus}}^{-1} = \tau_0^{-1}+\tau_{\mathrm{drop}}^{-1} \ , \tag{4.6}$$

resulting in a vanishing value for T. Inserting Eq. (4.6) and Eq. (4.2) into Eq. (4.5), the transfer efficiency for critical coupling $E = D\left(T=0\right)$ between both ultra-thin fiber tapers is then given by

$$E = 1 - 2Q_{\mathrm{load}}/Q_0 \ . \tag{4.7}$$

This means that, in order to achieve high transfer efficiencies, one has to significantly reduce Q_{load} which in turn leads to a decrease in the frequency selectivity of the add-drop filter. More details are given in section 4.1.3.

The experiments presented in the following are carried out under the condition of critical coupling. Therefore, the value Q_{load} stated for a bottle microresonator will always refer to the overall quality factor at critical coupling. This means that Q_{load} and Q_{crit}, as well as $\Delta\nu_{\text{load}}$ and $\Delta\nu_{\text{crit}}$ are equivalent. Nevertheless, I will use Q_{load} and $\Delta\nu_{\text{load}}$ for the bottle microresonator in add-drop configuration whenever I want to emphasize that the corresponding values at critical coupling are a function of the variable coupling to the drop fiber.

4.1.2 State of the art − UHQ add-drop filters

In the past, microresonator-based add-drop filters have been extensively studied [Vah04, Ill06, Hee08]. However, most of these devices featured low to moderately high Q resonators and their Q^2/V values were comparatively low. Consequently, high optical powers are required for potential non-linear applications. Moreover, high transfer efficiencies in resonator-based add-drop filters can only be obtained if the resonator-waveguide coupling rate dominates the resonator loss rate. This implies a further reduction of the Q factor of the loaded resonator. To my knowledge, the only add-drop filters based on ultra-high quality factor microresonators so far have been realized with WGMs. Transfer efficiencies of 93% at a loaded quality factor of 3.3×10^6 have been demonstrated using a 65–μm diameter microtoroidal resonator coupled to two ultra-thin fibers [Rok04]. The intrinsic quality factor of this resonator was $Q_0 = 1 \times 10^8$ for a wavelength around 1550 nm.

4.1.3 Experimental realization

In order to realize the add-drop configuration, the waists of two ultra-thin fibers with a diameter of 500 nm are placed at the axial position of the caustics of one particular resonator mode. The mechanical and optical setup is identical to the one described in section 3.1. Except when stated otherwise, the measurements described in the following are performed under the condition of critical coupling in order to obtain the highest possible power transfer on resonance. First, the bus fiber–resonator gap is adjusted in the absence of the drop fiber. By reducing the gap between the drop fiber and the resonator, light can be coupled into the second waveguide and is monitored by another photodiode, see Fig. 4.2. According to Eq. (4.6) the bus fiber gap has to be adjusted simultaneously in order to maintain critical coupling. In order to verify the relation in Eq. (4.7), the frequency of the probe laser is scanned over a bottle mode with an axial quantum number $q = 2$ and an intrinsic quality factor of $Q_0 = 1.8 \times 10^8$ in a 36–μm diameter resonator. The powers at both output ports are monitored. The performance of the resonator is characterized independently of the losses in the transitions of the ultra-thin fibers. The measured powers are corrected for these losses and one obtains the powers at the waist of the bus fiber $P_{\text{out}}^{\text{bus}}$ and the drop fiber $P_{\text{out}}^{\text{drop}}$, immediately following the resonator-fiber coupling junction. The input power P_{in} is also corrected in order to obtain its value at the fiber waist just before the coupling junction. In the following, this correction is carried out whenever solely the resonator performance is to be characterized.
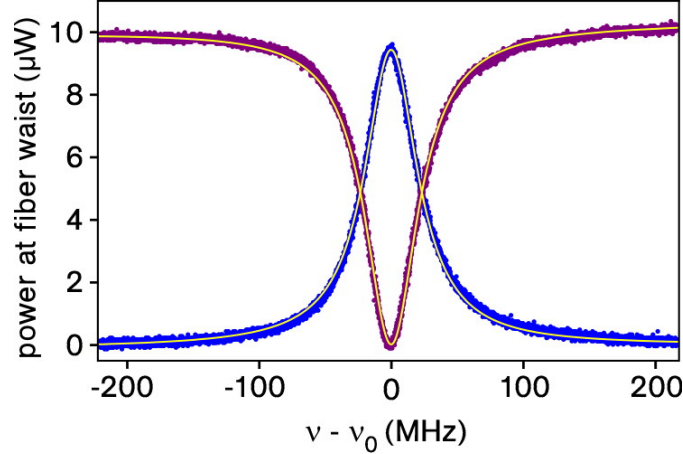
Figure 4.2: Resonant power transfer between two ultra-thin optical fibers coupled to the evanescent field of a bottle mode with ultra-high intrinsic quality factor. The plot shows the powers at the waists of the bus fiber $P_{\mathrm{out}}^{\mathrm{bus}}$ (purple dots) and the drop fiber $P_{\mathrm{out}}^{\mathrm{drop}}$ (blue dots) while the frequency of the probe laser is swept over the resonance. A loaded quality factor of $Q_{\mathrm{load}} = 7.2 \times 10^6$ and a power transfer efficiency $E = 0.93$ is inferred by fitting a Lorentzian to both signals (yellow curves).

In contrast, when demonstrating applications like all-optical switching or routing, the power launched into the input of the bus fiber and the powers at the outputs of the bus and the drop fiber are quoted. In subsequent measurements, the gap between the drop fiber and the resonator is reduced while the bus fiber gap is simultaneously adjusted to maintain the condition of critical coupling. Figure 4.2 shows one such measurement for a particular gap size. From a Lorentzian fit, a linewidth of $\Delta\nu_{\mathrm{load}} = 49$ MHz is determined, corresponding to a loaded quality factor of $Q_{\mathrm{load}} = 7.2 \times 10^6$, and a transfer efficiency of $E = 93\%$ between the fiber waists. The overall transfer efficiency E_{tot}, including the losses at the taper transitions to the ultrathin fiber waists, remains as high as $E_{\mathrm{tot}} = 90\%$. Figure 4.3 shows the power transfer efficiency between the fiber waists versus Q_{load} as inferred from above measurements. Fitting Eq. (4.7) to this data yields an intrinsic quality factor of $Q_0 = 1.8 \times 10^8$. In summary, the performance of the device in terms of combining high efficiency filter functionality, high loaded quality factor and single mode fiber operation lines up with the best to date [Rok04].

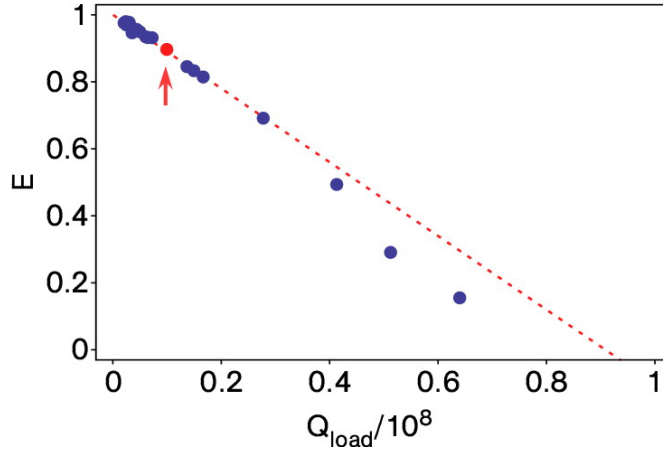**Figure 4.3:** Power transfer efficiency between both fiber waists at the critical coupling point as a function of Q_{load}. The data shows close agreement with the theoretical linear prediction, however, for high loaded quality factors, a slight modal splitting is observed, leading to an underestimation of the quality factor. Excluding the three rightmost data points, a fit of Eq. (4.7) (blue line) yields an intrinsic quality factor of $Q_0 = 1.8 \times 10^8$. The red arrow indicates the data point extracted from the measurement shown in Fig. 4.2.

4.2 Optical Kerr bistability at microwatt power levels

In all measurements presented so far, the bottle microresonator was operated in the linear regime. Heating of the mode volume caused by absorption, or a third order susceptibility $\chi^{(3)}$ of the resonator material introduce a nonlinear behavior, where ν_0 depends on the intracavity intensity via the thermo-optic or the Kerr effect. Nonlinear resonators show hysteretic, bistable behavior in the frequency dependency of the intracavity power or in the power at the resonator outputs as a function of the input power for a fixed frequency. At time scales larger than the thermal relaxation time of a mode, the nonlinear Kerr frequency shift is usually several orders of magnitude weaker than the one caused by the thermo-optic effect. Due to the sub-picosecond response time of the Kerr effect [Liu05], this situation can be inverted for fast modulations of the intracavity intensity [Rok05].

In the following section, bistability in bottle microresonators is experimentally investigated and then employed for all-optical switching applications. First, the principle of all-optical switching is explained and it is shown that resonator-based all-optical switching schemes offer the possibility of drastically lowering the switching power. The relevant material properties are discussed and material-related figures of merit are introduced. By slightly adapting the model from section 4.1, the bistable behavior in bottle microresonators caused by the Kerr effect can be described. The origin of the bistable behavior is investigated and the time scales on which the bistability is exclusively due to the Kerr effect is identified. In this regime, the obtained results are in close agreement with the findings from the model. Moreover, the performance of the bottle microresonator as an all-optical switch in terms of switching threshold and switching speed is experimentally

investigated. The measured switching powers of 50 μW are, to the best of my knowledge, the lowest values ever achieved for all-optical switching via the Kerr effect. However, the bandwidth of this ultra-low power all optical switch is limited to 5 MHz. Higher switching speeds can only be achieved by significantly increasing the switching threshold. Coating the bottle microresonator with a nonlinear polymer might offer a solution to this problem. Such a system is a promising candidate for the realization of all-optical switches with a bandwidth of up to several GHz and at the same time only moderate power requirements in the sub-Watt range.

4.2.1 Fundamentals – thermal and Kerr nonlinearity in microresonators

Thermal bistability

Bistability due to the thermo-optic effect is well known in WGM resonators [Bra89, Ill92]. This thermal bistability is readily observed when slowly scanning ν_{probe} over the resonance frequency of a mode. If the intracavity intensity exceeds a certain threshold, the line shape $T(\nu_{\mathrm{probe}})$ depends on the sign of $d\nu_{\mathrm{probe}}/dt$. Figure 4.4 shows this effect observed in a 35 μm bottle microresonator with a loaded quality factor in the 10^7–10^8 range. The power in the bus fiber waist is on the order of several tens of μW. In [Tre98], Kerr bistability in a 50–μm diameter microsphere with a quality factor of 2×10^8 was observed using the technique described above. In order to suppress the thermo-optic effect, the microsphere was cooled to cryogenic temperatures. At a threshold power around 10 μW, a resonance frequency shift on the order of the linewidth was observed.
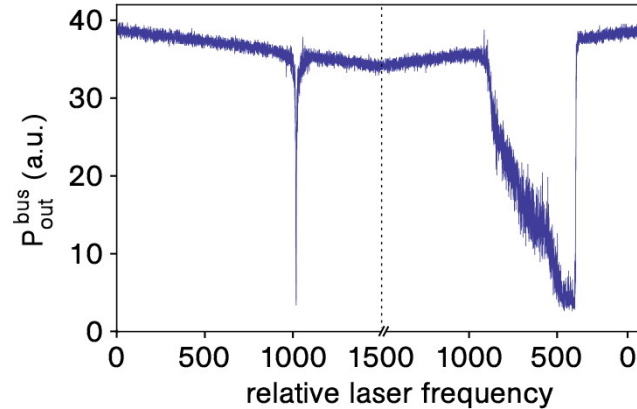
Figure 4.4: Thermal bistability in a bottle microresonator. Depending on the sign of $d\nu_{\mathrm{probe}}/dt$, the transmission $T(\nu_{\mathrm{probe}})$ shows two distinct values for a given frequency ν_{probe}. For $d\nu_{\mathrm{probe}}/dt < 0$ (right side of the graph) the resonance frequency shift due to heating of the mode volume by absorption has the same sign as the change of the laser frequency. The resonance frequency is therefore pulled along with the laser frequency scan causing a broadening of the line shape. In contrast, a scan over the same frequency range with $d\nu_{\mathrm{probe}}/dt > 0$ (left side of the graph) shows a reduction of the linewidth with respect to the line shape measured for powers P_{in} below the threshold of thermal bistability.

Origin of the Kerr nonlinearity

An electric field $\vec{E}$ of angular frequency ω_1 propagating in a dielectric medium generates a polarization $\vec{P}$. For high intensity fields, the polarization is a complicated function of the electric field and can be derived using a Taylor expansion [Mes04]. The i-th component of the polarization $\vec{P}$ can be written as a function of the components E_j ($j = 1, 2, 3$) of the electric field using the susceptibility tensors $\chi^{(m)}$ of order $m = 1, 2, 3 \dots$

$$P_i(r,t) = \epsilon_0 \chi_{ij}^{(1)} E_j + \epsilon_0 \chi_{ijk}^{(2)} E_j E_k + \epsilon_0 \chi_{ijkl}^{(3)} E_j E_k E_l \dots . \tag{4.8}$$

In the case of low intensities or weak higher order susceptibilities, $\chi^{(2)}$ and $\chi^{(3)}$, the polarization and the electric field show a linear relation. In this regime of linear optics, the medium is fully characterized by its refractive index $n = \sqrt{1 + \chi^{(1)}}$ and its absorption coefficient α. Otherwise, the higher order terms must be taken into account. The second term gives rise to polarizations $P(\omega = 2\omega_1)$ and $P(\omega = 0)$ and is thus responsible for phenomena well known as second harmonic generation and optical rectification [Mes04]. An additional wave with a frequency ω_2 incident into the nonlinear medium causes polarizations at the sum and difference frequencies $P(\omega = \omega_1 + \omega_2)$, $P(\omega = \omega_1 - \omega_2)$. These processes will only efficiently generate an electric field at the given frequency if a constant phase between the incident electric fields and the generated field is maintained. Due to dispersion of the refractive index, this phase matching condition is generally not fulfilled.

In this work, the focus lies on the optical Kerr effect which is related to the third term on the right hand side of Eq. (4.8). Three fields at frequencies ω_1, ω_2 and ω_3 generate polarizations at frequencies $\omega = \pm\omega_1 \pm \omega_2 \pm \omega_3$,

$$P_i(\omega) = \epsilon_0 \chi_{ijkl}^{(3)}(\omega, \omega_1, \omega_2, \omega_3) E_j(\omega_1) E_k(\omega_2) E_l(\omega_3) . \tag{4.9}$$

In the degenerate case, where $\omega_1 = \omega_2 = \omega_3$, this results in a polarization with frequency $\omega = 3\omega_1$ (third harmonic generation) and an additional contribution at the frequency of the driving field $\omega = \omega_1$. Since in the latter case all fields oscillate at the same frequency, the phase matching condition is automatically fulfilled without any further precautions to be taken. The overall polarization at the frequency of the driving field is then given by

$$P(\omega_1) = \epsilon_0 \left(\chi^{(1)} + \chi^{(3)}(\omega_1, \omega_1, \omega_1, -\omega_1)|E(\omega_1)|^2 \right) E(\omega_1) . \tag{4.10}$$

This gives rise to an intensity-dependent susceptibility at the frequency ω_1 and thus to a change in the refractive index

$$n = n_1 + n_2 \cdot I , \tag{4.11}$$

with the linear refractive index $n_1 = \sqrt{1 + \chi^{(1)}}$ and the nonlinear refractive index $n_2 \propto \chi^{(3)}$. This phenomenon is known as the Kerr effect. In a pump–probe experiment a strong pump field at frequency ω_2 can also induce a polarization at the frequency of a weak probe field ω_1,

$$P(\omega_1) = \epsilon_0 \left(\chi^{(1)} + \chi^{(3)}(\omega_1, \omega_1, \omega_2, -\omega_2)|E(\omega_2)|^2 \right) E(\omega_1) , \tag{4.12}$$
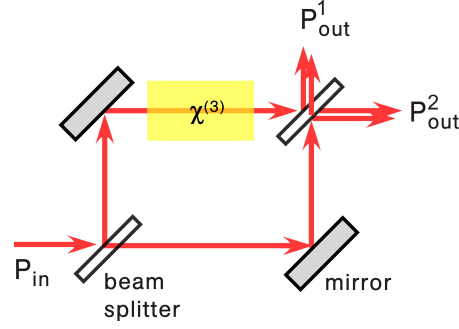
Figure 4.5: All-optical switch using a medium with high third order susceptibility placed in one arm of a Mach-Zehnder interferometer. A nonlinear phase shift of π is necessary in order to fully modulate the intensity at the output.

resulting in an refractive index change at the probe frequency. This situation is called cross-phase modulation, while in the case of only one beam incident into the nonlinear material one also speaks of self-phase modulation.

All-optical switching using the Kerr effect

The basic principle of all-optical switching is presented in Fig. 4.5. The nonlinear phase shift induced by the propagation of a free laser beam through a nonlinear material is translated into a intensity modulation by incorporating the nonlinear medium into a Mach-Zehnder interferometer. For sufficiently high input powers the relative phase shift between both interferometer arms, introduced by the Kerr effect, reaches a value of π. The optical power is thus switched between both output ports.

In order to obtain a switch with small dimensions and moderate power requirements, the material, regarding its linear and nonlinear properties α, n_2, and α_2 (two-photon absorption coefficient), has to be chosen carefully. In an absorbing medium, the nonlinear phase shift Φ_{NL} of a wave propagating in z direction is a function of the spatially varying intensity, described by

$$dI = -(\alpha I + \alpha_2 I^2) \cdot dz \ . \tag{4.13}$$

The overall nonlinear phase shift at a given position z in the nonlinear medium is then obtained by integration

$$\Phi_{\mathrm{NL}} = \int_0^z \frac{2\pi}{\lambda} n_2 I(z) dz \ . \tag{4.14}$$

If the linear absorption is the dominant loss mechanism $\alpha \gg \alpha_2 I$ the solution of both differential equations is given by

$$I(z) = I_0 \exp\left(-\alpha z\right) \qquad \text{and} \qquad \Phi_{\mathrm{NL}} = 2\pi \frac{n_2 I_0}{\lambda \alpha} \left(1 - \exp\left(-\alpha z\right)\right) \ . \tag{4.15}$$

For an critical intensity $I_{2\pi} = \alpha\lambda/n_2$ a phase shift of 2π is obtained for $z \to \infty$. In contrast, if the nonlinear absorption dominates one obtains

$$I(z) = \frac{I_0}{1 + \alpha_2 I_0 z} \qquad \text{and} \qquad \Phi_{\mathrm{NL}} = 2\pi \frac{n_2}{\lambda \alpha_2} \ln\left(1 + \alpha_2 I_0 z\right) \ . \tag{4.16}$$

material	λ (nm)	n_2 $(\mathrm{m^2W^{-1}})$	α $(\mathrm{m^{-1}})$	α_2 $(\mathrm{mW^{-1}})$	$I_{2\pi}$ $(\mathrm{Wmm^{-2}})$	T
SiO_2	852	$2.5{\cdot}10^{-20}$	$4.5{\cdot}10^{-4}$	-	$1.7\cdot10^4$	$\gg 1$
$Pb{:}SiO_2$	1064	$2.2{\cdot}10^{-19}$	0.5	$7.2{\cdot}10^{-15}$	$2\cdot10^6$	30
$As_{0.38}S_{0.62}$	1303	$4.2{\cdot}10^{-18}$	1.5	$<1.6{\cdot}10^{-12}$	$5\cdot10^5$	>2
GaAs	1064	$-3{\cdot}10^{-17}$	100	$2.5{\cdot}10^{-10}$	$4\cdot10^6$	0.1
$Al_{0.18}Ga_{0.82}As$	1555	$1{\cdot}10^{-17}$	10	$<1{\cdot}10^{-12}$	$1.5\cdot10^6$	>6
DANS	1319	$8{\cdot}10^{-18}$	40	$8{\cdot}10^{-13}$	$7\cdot10^6$	7.5
PPV	800	$1{\cdot}10^{-15}$	100	$8{\cdot}10^{-10}$	$8\cdot10^4$	1.6
MEH-PPV	1080	$2.2{\cdot}10^{-17}$	12	$2{\cdot}10^{-10}$	$6\cdot10^5$	0.2

Table 4.1: Linear and nonlinear material properties together with the figures of merit for all-optical switching for some glasses, semiconductors and polymers as given in [Lee02]. The stated values were measured for distinct wavelengths, at which the materials show favorable figures of merit. $Pb{:}SiO_2$ is known as lead silicate, $As_{0.38}S_{0.62}$ belongs to the chalcogenide glasses, DANS (4-dialkylamino-4´-nitro-stilbene) and PPV (polyphenylenevinylene) are nonlinear polymers.

In the literature it is common to characterize a Kerr material by $I_{2\pi} = \alpha\lambda/n_2$ and the two-photon figure of merit $T = n_2/(\lambda\alpha_2)$ [Lee02, Koy02]. The material is considered well suited for all-optical switching applications if it exhibits a small value for $I_{2\pi}$ and if $T \gg 1$. Typical values for both figures of merit for glasses, semiconductors and polymers are listed in [Lee02]. Table 4.1 gives an overview. The values of the nonlinear polymer MEH-PPV (poly[2-methoxy-5-(28-ethylhexyloxy)-1,4-phenylenevinylene]) is taken from [Koy02], those of SiO_2 from [Buc03] and [Tay96].

The values listed in the table show that the intensities required for all-optical switching according to the scheme proposed above are very high, even for materials with high n_2, which typically suffer from strong linear absorption. Nevertheless, such switches have been realized. In [Kim93] a 1.65 cm long and 1.8 μm thick waveguide fabricated from spin-coated films of the side-chain polymer DANS was incorporated in one arm of an Mach-Zehnder interferometer. A mode locked Nd:YAG laser, providing 90 ps pulses, was necessary to achieve a nonlinear phase shift of $\Phi_{\mathrm{NL}} = 0.5\pi$. The peak power coupled to the waveguide was estimated to be 39 W which corresponds to a peak intensity of 4.5×10^6 $\mathrm{Wmm^{-2}}$ at the input of the waveguide. By placing the nonlinear medium inside a resonator and employing its intensity enhancement, the power requirements can be significantly reduced.

Resonator enhanced all-optical switching

Figure 4.6 gives an overview of different resonator-based all-optical switching (AOS) schemes. The schemes are exemplary illustrated for an Fabry-Pérot (FP) resonator, see (a). In two-wavelength all-optical switching, as illustrated in Fig. 4.6 (b), a nonlinear resonator containing a medium that exhibits a strong third order nonlinear susceptibility is used for routing an input signal between its output ports by use of another, high-

intensity pump beam. The weak signal beam is initially detuned from resonance and most of the light is reflected. A high-intensity pump beam shifts the optical path length of the resonator by cross-phase modulation. If the resonance frequency shift is properly chosen, the signal beam is resonantly transmitted. In single-wavelength AOS, illustrated in Fig. 4.6 (c), the same effect is achieved by modulating the intensity of the signal beam. In the initial situation, only a small fraction of the optical power is coupled into the resonator mode. By increasing the input intensity, the resonance frequency is altered due to the Kerr effect. This in turn decreases the detuning between the resonator and the signal light field. Thus a larger fraction of the incident power is coupled to the resonator. When the intracavity intensity reaches a critical value, the resonator is pulled in resonance with the frequency of the signal light field in an self-amplified process. The case of single-wavelength AOS in a Fabry-Pérot cavity is readily transferred to a switch utilizing a bottle microresonator, as shown in Fig. 4.6 (d). The reflected power that does not enter the cavity in the case of an FP resonator corresponds to the power transmitted through the bus fiber for a bottle microresonator. The power transmitted through the FP on resonance corresponds to the power transferred to the drop fiber. The one- and
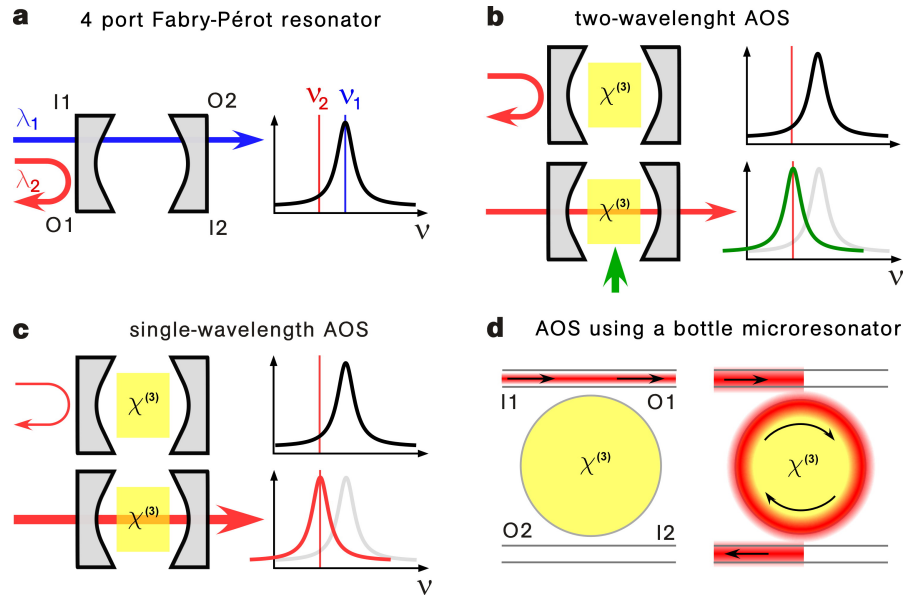
Figure 4.6: Different resonator enhanced all-optical switch schemes. (a) The schemes are illustrated for an FP resonator, which exhibits two input ports ($I1$ and $I2$) and two output ports ($O1$ and $O2$) and therefore forms an add-drop device comparable to a bottle microresonator coupled to two ultra-thin fibers. A resonant signal at frequency ν_1 incident into $I1$ is transmitted through the resonator and thereby transferred to $O2$. A signal detuned from resonance at frequency ν_2 is reflected into $O1$. (b–c) By introducing a Kerr material into the FP, a signal beam initially detuned from resonance can be switched between $O1$ and $O2$, employing an intense pump beam or by modulation of the intensity of the signal beam itself. (d) Transfer of the single-wavelength all-optical switching scheme to a bottle microresonator, fabricated from a nonlinear material.

two-wavelength schemes are neither directly comparable nor do they provide the same functionality. This work focuses on one-wavelength all-optical switches. In the following, the advantages and disadvantages of resonator-based switching schemes are discussed in detail. Although this discussion is in principle valid for all types of microresonators, the focus will lie on monolithic WGM resonators.

Reduction of the switching threshold.   I will now derive an expression for the threshold power, allowing one to define a figure of merit for resonator-based single-wavelength all-optical switching.

The nonlinear shift of the resonance frequency, required for optical switching, $\Delta\nu_0$, scales as $1/Q_{\mathrm{crit}}$. At critical coupling, a shift of the resonance frequency of the linewidth $\Delta\nu_{\mathrm{crit}}$ is sufficient to switch between 80% and 0% transmission through a waveguide coupled to a WGM resonator. The required relative resonance frequency shift[1] is then given by

$$\Delta\nu_0/\nu_0 = -\Delta\nu_{\mathrm{crit}}/\nu_0 = -1/Q_{\mathrm{crit}} \qquad (4.17)$$

and can therefore be made very small for UHQ bottle resonators. Moreover, the strong enhancement of the intracavity intensity leads to large nonlinear resonance frequency shifts for only moderate input powers. The intracavity intensity at critical coupling is given by $I_0^{\mathrm{crit}} = P_{\mathrm{in}}(n^2\lambda_0/\pi)(Q_{\mathrm{crit}}/V_{m,q})$. This formula is derived from Eq. (3.20), assuming $Q_0 = 2Q_{\mathrm{crit}}$, and is therefore only valid in the absence of the drop fiber. For an initial detuning between the optical frequency of the probe laser light and the optical resonance frequency of the bottle mode $\delta_0^\nu = \nu_{\mathrm{probe}} - \nu_0 = -\Delta\nu_{\mathrm{crit}}$, 20% of P_{in} is inserted into the resonator. For example, in a microresonator with a mode volume of 1000 $\mu\mathrm{m}^3$ and a quality factor of $Q_0 = 10^8$, a power of $P_{\mathrm{in}} = 1$ mW launched into the bus fiber then corresponds to a intracavity intensity of 2 MW/mm^2. The relative nonlinear resonance frequency shift is given by

$$\Delta\nu_0/\nu_0 = -\Delta n/n \approx -0.2 P_{\mathrm{in}} \frac{n_2 n \lambda_0}{\pi} \frac{Q_{\mathrm{crit}}}{V_{m,q}} \ . \qquad (4.18)$$

By combining Eq. (4.17) and Eq. (4.18), an estimation for the threshold power at which switching occurs is obtained assuming an initial detuning of $\delta_0^\nu = -\Delta\nu_{\mathrm{crit}}$,

$$P_{\mathrm{thr}} = \frac{5\pi}{n_2 n \lambda_0} \frac{V}{Q_{\mathrm{crit}}^2} \ . \qquad (4.19)$$

Taking into account only linear losses, the relation $Q_{\mathrm{mat}} = 2\pi n/(\alpha\lambda_0) = 2Q_{\mathrm{crit}}$, valid for monolithic resonators, can be used to define a material-related figure of merit for resonator-based all optical switching

$$P_{\mathrm{thr}} = \frac{5\alpha^2 \lambda_0 V_{m,q}}{\pi n_2 n^3} \ . \qquad (4.20)$$

Table 4.2 gives an overview of P_{thr} for the nonlinear materials from Tab. 4.1.   The

---

[1] An increase in the intracavity intensity gives rise to a positive refractive index change and thus to a negative resonance frequency shift, leading to the minus sign in Eq. (4.17). Therefore, in order to achieve all-optical switching, the frequency of the signal light field has to be set to a value smaller than the initial resonance frequency ν_0, as illustrated in Fig. (4.6).

material	λ	n_2	α	Q_{mat}	P_{thr}
	(nm)	$(\mathrm{m}^2\mathrm{W}^{-1})$	(m^{-1})		(W)
SiO_2	852	$2.5 \cdot 10^{-20}$	$4.5 \cdot 10^{-4}$	$2.4 \cdot 10^{10}$	$3.5 \cdot 10^{-9}$
				$(3.6 \cdot 10^8)$	$(1.6 \cdot 10^{-5})$
$Pb{:}SiO_2$	1064	$2.2 \cdot 10^{-19}$	0.5	$2.0 \cdot 10^7$	$3.9 \cdot 10^{-4}$
$As_{0.38}S_{0.62}$	1303	$4.2 \cdot 10^{-18}$	1.5	$7.7 \cdot 10^6$	$8.0 \cdot 10^{-5}$
GaAs	1064	$-3 \cdot 10^{-17}$	100	$2.1 \cdot 10^5$	$1.3 \cdot 10^{-2}$
$Al_{0.18}Ga_{0.82}As$	1555	$1 \cdot 10^{-17}$	10	$1.3 \cdot 10^6$	$6.9 \cdot 10^{-4}$
DANS	1319	$8 \cdot 10^{-18}$	40	$1.9 \cdot 10^5$	$1.0 \cdot 10^{-1}$
PPV	800	$1 \cdot 10^{-15}$	100	$2.0 \cdot 10^5$	$8.2 \cdot 10^{-4}$
MEH-PPV	1080	$2.2 \cdot 10^{-17}$	12	$8.2 \cdot 10^5$	$2.5 \cdot 10^{-3}$

Table 4.2: Estimated switching threshold P_{thr} and absorption limited quality factor Q_{mat} for the same nonlinear materials as presented in Tab. 4.1. A mode volume of 1000 $\mu\mathrm{m}^3$, typical for WGM microresonators, is assumed. The values given in brackets for SiO_2 are the quality factor experimentally observed in an 35 μm silica bottle microresonator, limited by surface-related losses and the resulting threshold power. Even when assuming this value, P_{thr} in silica is at least a factor of 5 smaller than the values for all other materials.

nonlinear refractive index of silica is two to three orders of magnitude lower than for common nonlinear materials. At the same time, however, silica exhibits a very low absorption coefficient of $\alpha = 4.5 \times 10^{-4}$ m^{-1} at a wavelength of 852 nm [Buc03], which enables the ultra-high quality factors observed in silica WGM resonators. Therefore, the $n_2 Q^2/V$-ratio of ultra-high Q silica WGM microresonators ranks among the highest that can be realized, making them ideal candidates for all-optical switching applications at ultra-low powers. In a silica bottle microresonator with a quality factor of $Q_{\mathrm{crit}} = 1.8 \times 10^8$ and a mode volume of 1000 $\mu\mathrm{m}^3$, the required power for all-optical switching is expected to be as low as $P_{\mathrm{thr}} = 16$ μW. Figure 4.7 shows the diameter dependency of Q_{crit}^2/V in order to identify the optimal bottle resonator diameter for all-optical switching experiments.

Limitations in switching speed. The trade-off in resonator-based switching schemes is a limited speed at which the switch can be operated. The exponential build-up and decay of the intracavity intensity with the time constant τ_{load} results in a -3 dB bandwidth B given by

$$B = \frac{1}{2\pi\tau_{\mathrm{load}}} = \Delta\nu_{\mathrm{load}} \ . \tag{4.21}$$

That means that for a modulation of P_{in} the energy build-up inside the resonator and thus the nonlinear resonance frequency shift drops by a factor of two at a modulation frequency corresponding to the bandwidth.
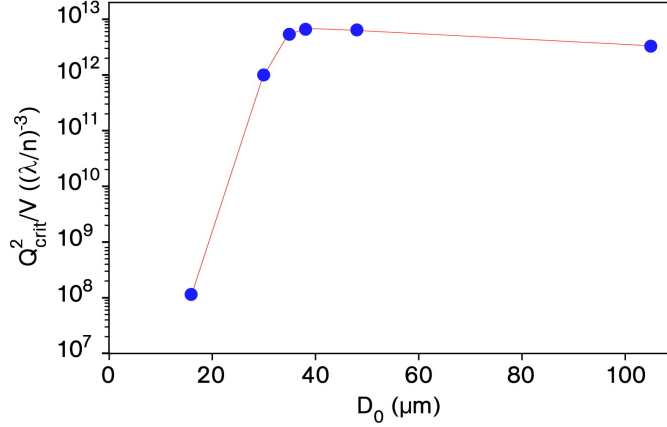
Figure 4.7: The ratio Q_{crit}^2/V for bottle microresonators of various diameter D_0. This graph is based on the data from Fig. 3.18. The optimal ratio is obtained for resonators of diameters around 40 μm.

4.2.2 Model – Kerr bistability in bottle microresonators

In order to model the Kerr bistability in a bottle microresonator in add-drop configuration, a term that describes the shift in the resonance frequency $\Delta\omega_0(I)$ depending on the intracavity intensity $I(t)$ is added to Eq. (4.1)

$$\frac{d}{dt}a(t) = i(\omega_0 + \Delta\omega_0(I) - \omega)a(t) - \frac{1}{2}\left(\tau_0^{-1} + \tau_{\text{bus}}^{-1} + \tau_{\text{drop}}^{-1}\right)a(t) + \tau_{\text{bus}}^{-1/2}s(t) . \quad (4.22)$$

In the following, the intracavity intensity is modelled as a boxcar function of the radial coordinate within the FWHM radii r_1 and r_2 of the normalized radial intensity distribution $I(r)/I_{\text{max}}$ of the fundamental mode in an 35–μm diameter resonator. Using Eq. (3.19) for the peak value of the intracavity intensity yields

$$I(t) = \frac{|a(t)|^2 c\, n^2}{V_{m,q}} \cdot \frac{\int_{r_1}^{r_2} I(r)/I_{\text{max}} \cdot r dr}{\int_{r_1}^{r_2} r dr} = 0.81\frac{|a(t)|^2 cn^2}{V_{m,q}} . \quad (4.23)$$

The nonlinear resonance frequency shift can thus be written as

$$\Delta\omega_0(t) = -\omega_0\frac{n_2 I(t)}{n} = -\frac{1.62 \cdot \pi n \cdot n_2 c^2}{\lambda_0 V_{m,q}}|a(t)|^2 \equiv -c_{\text{Kerr}}|a(t)|^2 , \quad (4.24)$$

assuming a nonlinear refractive index of $n_2 = 2.5 \times 10^{-20}$ W/m^2 at a wavelength of $\lambda_0 = 852$ nm. For a given "cold" laser–resonator detuning $\delta_0^\omega = \omega - \omega_0$, i.e., the laser–resonator detuning for vanishing input powers, one obtains

$$\frac{d}{dt}a(t) = -i(c_{\text{Kerr}}|a(t)|^2 + \delta_0^\omega)a(t) - \frac{1}{2}\left(\tau_0^{-1} + \tau_{\text{bus}}^{-1} + \tau_{\text{drop}}^{-1}\right)a(t) + \tau_{\text{bus}}^{-1/2}s(t) . \quad (4.25)$$

In order to investigate the bistable behavior, the input wave amplitude is modelled as

$$\begin{aligned}
s(t) &= \sqrt{1/2 \cdot P_{\text{max}}\left(1 - \cos\left(2\pi t/T\right)\right)} , &&\text{for } 0 \leq t \leq T \text{ and} \\
s(t) &= 0 , &&\text{for } t > T \text{ and } t < 0 .
\end{aligned} \quad (4.26)$$

P_{in} thus corresponds to a $\sin^2$-shaped pulse with a FWHM pulse duration of $\tau_{\text{pulse}} = T/2$. For critical coupling, i.e., $\tau_{\text{bus}}^{-1} = \tau_0^{-1} + \tau_{\text{drop}}^{-1}$, the time constants can be expressed using the loaded quality factor, $Q_{\text{load}}^{-1} = 1/(\omega_0\tau_0) + 1/(\omega_0\tau_{\text{bus}}) + 1/(\omega_0\tau_{\text{drop}})$, and the intrinsic quality factor Q_0

$$
\begin{aligned}
\tau_0^{-1} &= \frac{\omega_0}{Q_0} \ , \\
\tau_{\text{drop}}^{-1} &= \frac{\omega_0}{2Q_{\text{load}}} - \frac{\omega_0}{Q_0} \ , \\
\tau_{\text{bus}}^{-1} &= \frac{\omega_0}{2Q_{\text{load}}} \ .
\end{aligned}
\tag{4.27}
$$

Equation (4.25) is then numerically solved for $a(t)$ with $0 \leq t \leq T$ using the boundary condition $a(0) = 0$. The relevant quantities are inferred from

$$
\begin{aligned}
P_{\text{in}}(t) &= |s(t)|^2 \ , \\
P_{\text{out}}^{\text{bus}}(t) &= |-s(t) + \tau_{\text{bus}}^{-1/2}a(t)|^2 \ , \\
P_{\text{out}}^{\text{drop}}(t) &= \tau_{\text{drop}}^{-1}|a(t)|^2 \ , \\
\delta^\omega(t) &= \delta_0^\omega + c_{\text{Kerr}}|a(t)|^2 \ .
\end{aligned}
\tag{4.28}
$$

Here, $\delta^\omega = \delta_0^\omega - \Delta\omega_0$ is the instantaneous laser–resonator detuning when the pulse is applied. Note that $P_{\text{out}}^{\text{drop}}$ is proportional to the intracavity energy. Figure 4.8 shows the result of the numerical calculation for a bottle mode with a mode volume of $V = 1000 \ \mu\text{m}^3$. Its intrinsic quality factor of $Q_0 = 1.8 \times 10^8$ is assumed to be reduced to $Q_{\text{load}} = 1.7 \times 10^7$ due to the coupling to both ultra-thin fibers. Moreover, a cold resonator–laser detuning of one linewidth $\delta_0^\omega = -\Delta\omega_{\text{crit}}$, a pulse duration of $\tau_{\text{pulse}} = 1.25 \ \mu\text{s}$ and a peak power $P_{\text{max}} = 0.51$ mW is assumed. For the given parameters, the value of P_{max} was chosen by trial and error. It was stepwise increased until δ^ω reached positive near-zero values in the central region of the pulse of P_{in}. In order to reveal the bistable behavior, $P_{\text{out}}^{\text{bus}}$ and $P_{\text{out}}^{\text{drop}}$ are plotted as a function of P_{in}. The result is shown in Fig. 4.9
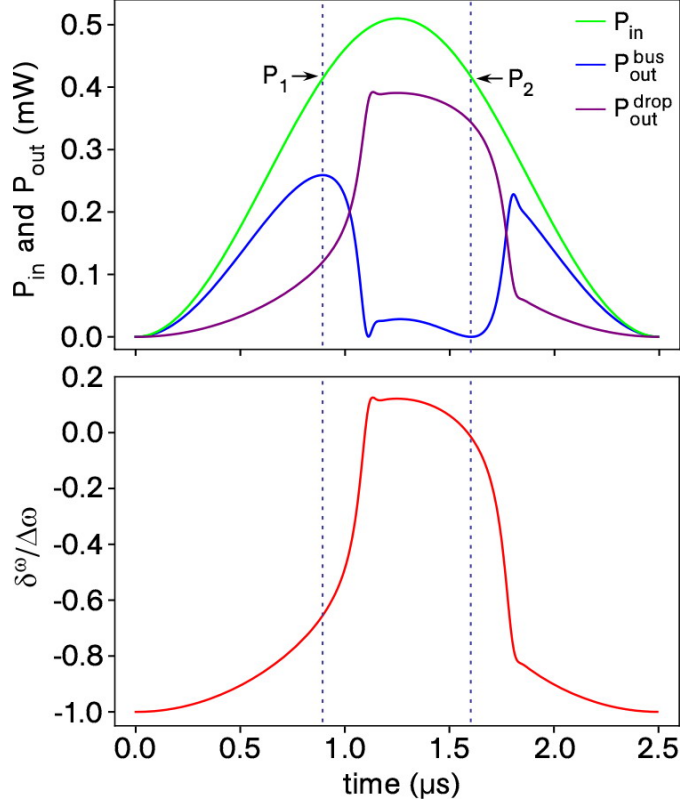
Figure 4.8: (a) $P_{\text{out}}^{\text{bus}}$ and $P_{\text{out}}^{\text{drop}}$ modelled for a $\sin^2$-shaped pulse of the input power P_{in}. A resonator with parameters $Q_0 = 1.8 \times 10^8$, $Q_{\text{load}} = 1.7 \times 10^7$ and $V = 1000~\mu\text{m}^3$ is assumed. (b) Evolution of the laser–resonator detuning δ^ω. The cold laser–resonator detuning at $t = 0$ has a value of $\delta_0^\omega = -\Delta\omega_{\text{crit}}$. When P_{in} exceeds a threshold P_1, $d\delta^\omega/dP_{\text{in}}$ reaches a critical value and the Kerr effect "pulls" the resonator mode into resonance with the laser frequency. At the peak value of P_{in}, the detuning reaches positive values. When P_{in} decreases again, at a power P_2, the intracavity intensity ($\propto P_{\text{out}}^{\text{drop}}$) has sufficiently decreased to reach zero detuning. From this point onward, the resonator rapidly returns to the initial situation. The exact values of the threshold powers are defined by $dP_{\text{out}}^{\text{bus}}/dP_{\text{in}} = 0$. Between the two switching events, the transmission through the bus fiber is strongly reduced due to critical coupling. At the same time, due to the near-zero values of δ^ω, the intracavity power is high and a large fraction of P_{in} is transferred to the drop fiber output.
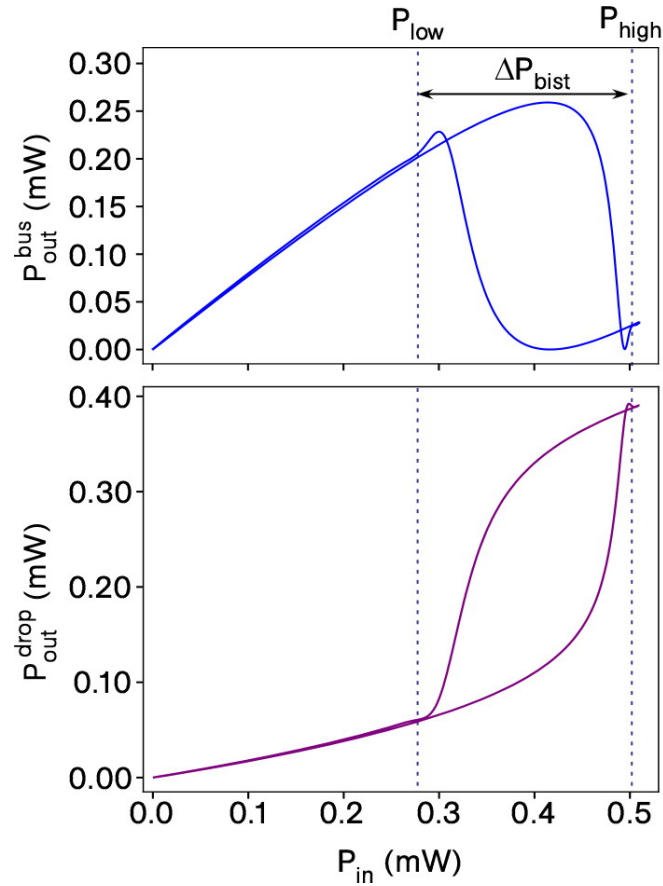
Figure 4.9: (a) P_out^bus and (b)P_out^drop as a function of P_in. The system shows a pronounced hysteretic behavior and, for a certain range of P_in, exhibits two stable states. The bistable regime is defined as the region between the powers P_low and P_high, where both, P_out^bus and (b)P_out^drop, show different values depending on the sign of dP_in/dt. Note that the threshold powers, P_1 and P_2, do not coincide with the borders of the bistable region.

4.2.3 State of the art – optical switching at ultra-low powers

In the following, an overview of the performance of state-of-the-art all-optical switches, based on various microresonator designs, in terms of their switching threshold is given. Not all experiments cited here, are aimed at achieving lowest possible values for the switching threshold P_1. Often, a compromise between the switching threshold and the bandwidth is chosen. Given the Q_{load}^{-2} dependency of P_1 and the Q_{load}^{-1} dependency of the bandwidth B, I will consider the constant ratio P_1/B^2 as a figure of merit, thus ensuring a fair comparison between different systems. The lowest bistable switching thresholds were reported for photonic crystal cavities using the thermo-optic effect [Not05, Wei07]. The lowest measured value of $P_1 = 6.5$ μW was observed in a photonic crystal micro-resonator made of GaAs [Wei07]. The bandwidth of such a thermo-optical switch is, however, only on the order of 1 MHz because the thermal relaxation times in photonic crystal cavities amount to at least 100 ns [Not05, Har09]. These switches thus offer a the lowest switching threshold but are fundamentally limited in their switching speed and yield a value of $P_1/B^2 = 6.5$ μW/MHz^2. Moreover, to my knowledge, no add-drop functionality has been experimentally realized with photonic crystal cavities so far. This limits their use in all-optical signal processing to "ON-OFF" switching of the power in one channel while switching of signals between two channels is not possible. Thermo-optical bistability has also been observed in silicon ring-resonators at a switching threshold of 1.3 mW [Alm04a]. Here, the bandwidth was found to be 500 kHz, which results in a P_1/B^2-ratio of 5200 μW/MHz^2 that is three orders of magnitude worse than for photonic crystals. Optical switching can also be achieved using free carrier nonlinearities induced by one- or two-photon absorption in semiconductors. Many of the corresponding experiments rely on the above-mentioned two-wavelength pump-probe optical switching schemes [Van02, Ibr03, Alm04b] and will not be discussed here further. However, free carrier nonlinearities were also employed to realize single-wavelength optical switching in bistable semiconductor etalons, see [Pey85] and references therein. In these devices, typical switching threshold powers exceed 1 mW while the bandwidth ranges around 100 MHz, limited by the carrier recombination time and/or diffusion speed. For example, values of $P_1 = 8$ mW and $B = 160$ MHz or $P_1 = 2$ mW and $B = 80$ MHz were reported in [Pey85] and [He93], respectively. In both cases, this yields the same value of $P_1/B^2 = 0.3$ μW/MHz^2. However, due to their relatively high intrinsic losses, the bistable etalons are not suited for operation in transmission. Operation in reflection mode therefore limits their use in all-optical signal processing to ON-OFF switching. Moreover, the physical mechanism leading to the nonlinearity is strongly wavelength-dependent. The devices therefore have to be optimized for operation at a particular wavelength. The Kerr effect, on the other hand, prevails over a much larger spectral range.
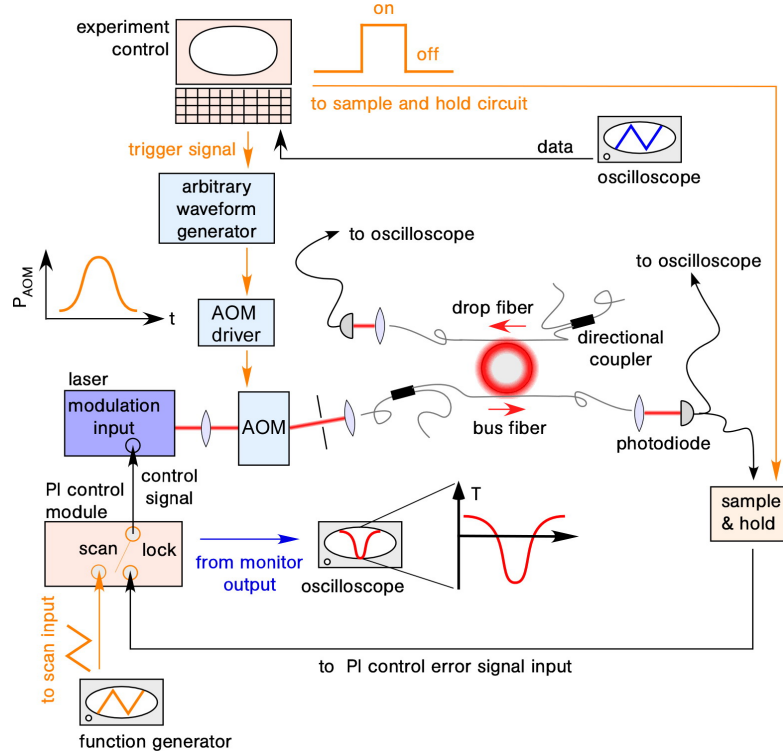
4.2.4 Experimental Setup

Figure 4.10: Measuring the nonlinear response in the transmission properties through two ultra-thin fibers coupled to a bottle mode in add-drop configuration, induced by a modulation of the input power P_{in}. An arbitrary waveform generator, triggered by the experiment control, sends an $\sin^2$-shaped pulse to the modulation input of the AOM's driver unit which controls the power of the radiofrequency signal P_{AOM} that is sent to the AOM. The initial cold laser–resonator detuning δ_0^{ν} is set using a side-of-fringe power lock technique, where the signal transmitted through the bus fiber is fed back to the current modulation input of the laser using a PI control loop. In the "scan mode" the laser frequency is constantly swept over the resonance. A monitor output of the PI control module allows one to choose a "set point". In the "lock mode", the PI control module controls the laser diode current in order to keep the error signal at this set-point. Its value is chosen corresponding to the desired value of the laser–resonator detuning. The PI control module allows one to change the sign of δ_0^{ν} by inverting the input signal. A sample-and-hold circuit "freezes" the lock during the pulse. A directional coupler at the inputs of both ultra-thin fibers allows one to measure the losses in the fiber tapers in order to obtain the power levels P_{in} and P_{out} in the ultra-thin fiber waists.

In the following, the bistable behavior of the transmission properties of the bottle microresonator caused by the nonlinearity of the resonator material, as predicted by the model, is investigated. The mechanical and optical components of the setup used here are identical to the setup for the characterization of the add-drop filter in the previous section. $P_{\text{out}}^{\text{bus}}$ and $P_{\text{out}}^{\text{drop}}$ are measured as a function of P_{in} at a fixed cold

laser–resonator detuning $\delta_0^\nu = \delta_0^\omega/(2\pi)$. As in the model, the input power is pulsed with a $\sin^2$-shaped envelope using an acousto-optic modulator. A peak power of up to a few milliwatts and pulse durations ranging from $\tau_{\text{pulse}} = 30$ ns – 10 ms were employed. The crucial point of this measurement is to set an initial laser–resonator detuning, before the pulse is applied and to let the system evolve freely during the pulse in order to monitor the nonlinear resonance frequency shift via a change in the bus and drop fiber transmission. The principle of the measurement is schematically illustrated in Fig. 4.10. Before the input power is modulated using an AOM (Crystal Technology, 3200-121, 200 MHz), whose driver unit is controlled by an arbitrary waveform generator (Agilent Technologies, 33250A), δ_0^ν is set to a predetermined value using a side-of-fringe power lock technique [Car05]. The output signal of the photodiode measuring the power transmitted through the bus fiber ("error signal") is fed back to the current modulation input of the laser via a PI control loop. The -3 dB bandwidth limit of the control loop is 10 kHz, limited by the bandwidth of the current modulation of the laser controller. The photodiode signal is fed through a so-called sample-and-hold circuit (custom made, denotation: SHC), which "freezes" the feedback signal at its instantaneous value while the pulse is applied in order to visualize the nonlinear shift in the resonance frequency. In the "sample mode" it constantly acquires the photodiode signal. In the "hold mode", which is activated by a TTL pulse, the last measured value before the arrival of the pulse is maintained at its output.

4.2.5 Experimental observation of optical bistability and switching in bottle microresonators

In order to verify the findings from the above model, a $q = 2$ mode with an intrinsic quality factor of 1.8×10^8 is used in add-drop configuration. The gap between the resonator and the drop fiber is chosen to yield a loaded quality factor of $Q_{\text{load}} = 1.7 \times 10^7$ at critical coupling. The set-point of the lock corresponds to a negative detuning of $\delta_0^\nu = \nu_{\text{probe}} - \nu_0 = -1.2 \times \Delta\nu_{\text{crit}}$. This corresponds to a 15% reduction of the optical power transmitted through the bus fiber. In order to obtain an error signal with a sufficient signal-to-noise ratio, input powers of 2–10 μW are used when locking the laser frequency to the resonance frequency of the bottle microresonator. Figure 4.11 (a) shows the powers at the bus and drop fiber waists for a $\sin^2$-shaped modulation of P_{in} with a FWHM pulse duration of $\tau_{\text{pulse}} = 1.25$ μs. Between the two switching events 84% of P_{in} is transferred to the drop fiber. Figure 4.11 (b) shows the hysteretic behavior in $P_{\text{out}}^{\text{bus}}$ and $P_{\text{out}}^{\text{drop}}$ as a function of P_{in}.

Note that the model presented in section 4.2.2 only allows one to numerically solve the differential equation that describes the bottle microresonators detuning $\delta^\omega(t)$ and its mode amplitude $a(t)$ from which the powers $P_{\text{out}}^{\text{bus}}(t)$ and $P_{\text{out}}^{\text{drop}}(t)$ are calculated. Analytical expressions for $P_{\text{out}}^{\text{bus}}(t)$ and $P_{\text{out}}^{\text{drop}}(t)$ for a given variation in the input power are therefore not known. Consequently, experiment and model can only be compared qualitatively. Nevertheless, the results are in close agreement with the predictions from the model, both in terms of the threshold power P_1 and the characteristic evolution of the bus and drop fiber transmissions during the pulse, see Fig. 4.8 and Fig. 4.9. The
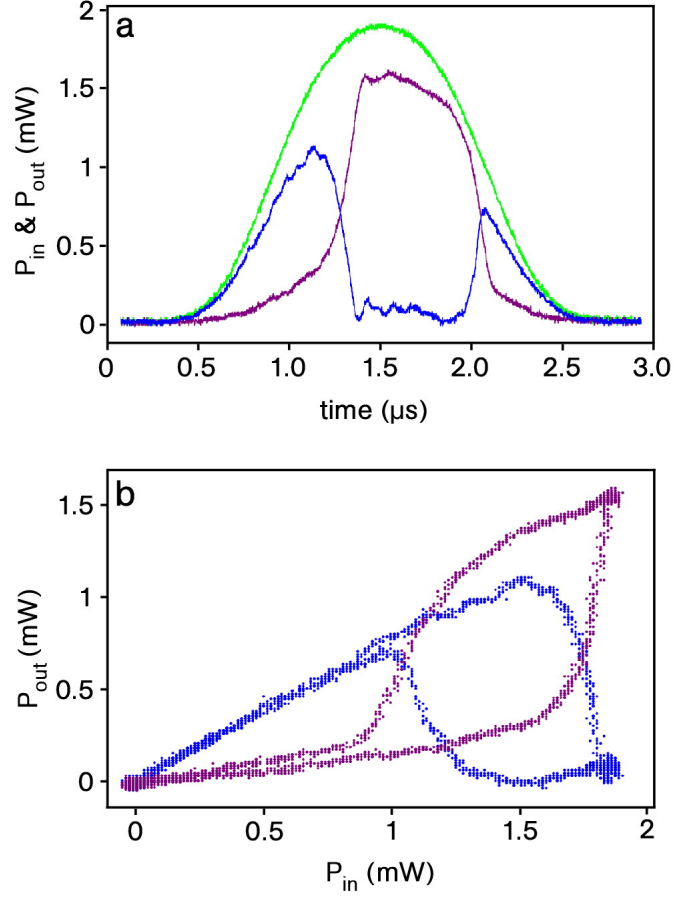
Figure 4.11: Optical bistability in a bottle microresonator. In order to characterize the bistable behavior of bottle modes, the input power is pulsed and the laser frequency is initially detuned from resonance by $\delta_0^\nu = -1.2 \times \Delta\nu_{\mathrm{crit}}$. (a) Response of the system to a $\sin^2$-shaped pulse with a FWHM duration of $\tau_{\mathrm{pulse}} = 1.25~\mu$s (green). The plot shows P_{in} (green), $P_{\mathrm{out}}^{\mathrm{bus}}$ (blue) and $P_{\mathrm{out}}^{\mathrm{drop}}$ (purple). As soon as P_{in} exceeds a certain threshold, the light is resonantly switched to the drop fiber via the Kerr effect. (b) By plotting $P_{\mathrm{out}}^{\mathrm{bus}}$ and $P_{\mathrm{out}}^{\mathrm{drop}}$ versus P_{in} for the data shown in Fig. 4.11 (a) (identical color coding), bistable behavior is apparent for P_{in} ranging from $P_{\mathrm{low}} \approx 1.0$ mW to $P_{\mathrm{high}} \approx 1.8$ mW.

modelled threshold power is only a factor of three smaller than the measured value. This deviation is attributed to the simple approximation of the intensity distribution of the bottle mode in Eq. (4.23).

4.2.6 Physical origin of the bistability

The close agreement of above measurements with the predictions from the model strongly suggests that that the Kerr effect is at the origin of the bistable behavior observed at the μs time scale. Nevertheless, in order to faithfully distinguish between switching due to the Kerr effect, that in principle exhibits a sub-picosecond response time, and the thermal-optic effect, additional measurements are necessary. First, the thermal relaxation time τ_{therm} of bottle modes is determined. Second, the dependency of the threshold power P_1 is measured as a function of τ_{pulse} in order to precisely identify the time scales at which the nonlinearity is exclusively due to the Kerr effect.

Measuring the thermal relaxation time.

The thermal relaxation time of a bottle mode is measured by tracing its resonance frequency shift over time after an abrupt change of the intracavity power. Figure 4.12 shows the setup used for this measurement. During the whole measurement the laser–resonator detuning $\delta\nu$ is kept constant by the side-of-fringe power lock technique. Using an AOM (Crystal Technology, 3200-121, 200 MHz), whose driver unit is controlled by an arbitrary waveform generator, P_{in} is modulated by applying a single 70 ms rectangular pulse. During this pulse P_{in} is abruptly changed from a level of a few mW, necessary to maintain the lock, to several tens of mW. Due to absorption, the resonator material heats up in the area where the bottle mode is located and the resonance frequency shifts. This shift can be traced via the "control signal" U_{PI} of the PI control module sent to the laser current modulation input in order keep $\delta\nu$ constant.

Simultaneously a second AOM modulates the laser power at the bus fiber output. The arbitrary waveform generator (AWG in the following) controlling the driver unit of this AOM (Crystal Technology, 3110-197, 110 MHz), generates a signal that is inverted with respect to the one applied to the AOM at the bus fiber input. In order to achieve synchronization between both AWGs, they are connected via their trigger in- and outputs. First, with the bus fiber, removed from the resonator, the time delay and amplitudes of both AWG outputs are adjusted in order to keep the power detected at the photodiode constant when the pulses are applied. This ensures that the photodiode signal, that serves as the "error signal" for the PI control loop, only changes when the transmission through the ultra-thin waist of the bus fiber, $T = P_{\mathrm{out}}(t)^{\mathrm{bus}}/P_{\mathrm{in}}(t)$, changes due to a variation in $\delta\nu$. Next, the bus fiber is critically coupled to the bottle mode under investigation and ν_{probe} is locked to the resonance with an appropriately chosen detuning $\delta\nu$. The pulse is again applied and the control signal is monitored. Using the reference cavity, the laser frequency shift $d\nu_{\mathrm{probe}}$ for a given change in the control signal dU_{PI} is calibrated. This calibration yields $d\nu_{\mathrm{probe}}/dU_{\mathrm{PI}} = (-6 \pm 0.3)$ MHz/mV for the given setup. Since the resonator is only heated in a small area close to its sur-
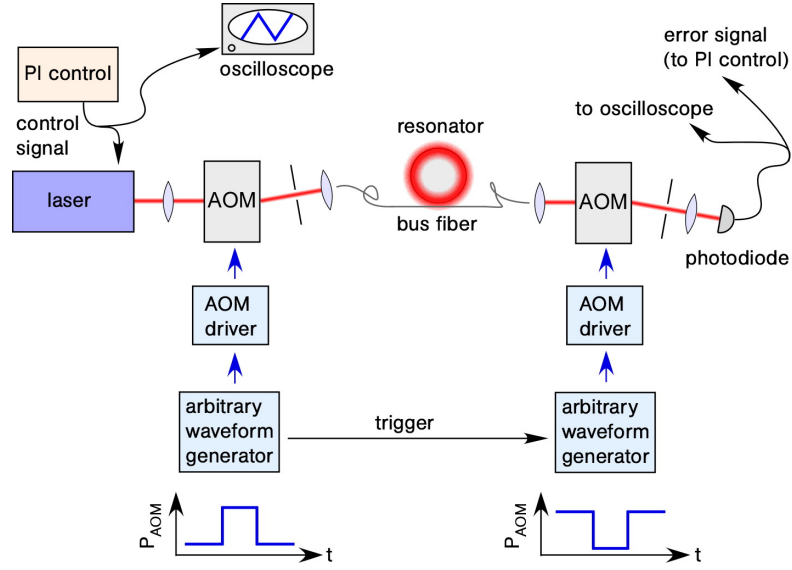
Figure 4.12: Setup for measuring the thermal relaxation time of a bottle mode. During the measurement, a sudden step in P_{in} is applied using an arbitrary waveform generator that controls the power modulation input of the AOM's driver unit (P_{AOM} denotes the power of the radiofrequency signal sent to the AOM). During the modulation of P_{in}, the laser–resonator detuning δ^{ν} is kept constant by the side-of-fringe power lock technique described in section 4.2.4. The control signal sent from the PI control module to the laser current modulation input is then proportional to the resonance frequency shift and the change in the temperature of the mode volume induced by the sudden increase in the intracavity intensity. Due to the variation in P_{in}, the power measured directly behind the bus fiber output is no longer a suitable error signal for the lock because it not exclusively depends on δ^{ν}. Therefore, the step in P_{in} is compensated using a second AOM in front of the photodiode. This ensures that the signal detected at the photodiode is proportional to the transmission through the ultra-thin waist of the bus fiber $U_{\mathrm{PD}} \propto P_{\mathrm{out}}^{\mathrm{bus}}(t)/P_{\mathrm{in}}(t)$.

face, the shift of its resonance frequency $\Delta\nu_0$ is exclusively due to the thermo-optic effect. Using Eq. (3.39) for the resonance frequency shift induced by a change in the refractive index, the thermo-optic coefficient $\partial n/\partial T$ and assuming $d\nu_{\mathrm{probe}} = d\nu_0$ one obtains $dT_{\mathrm{mode}}/d\nu_{\mathrm{probe}} = -n/v_0\,(\partial n/\partial T)^{-1} = -3.2 \cdot 10^{-10}$ K/Hz. Figure 4.13 shows the relative temperature of the mode volume T_{mode}, calculated from the control signal of the PI control loop, together with the transmission through the bus fiber, calculated from the signal detected at the photodiode U_{PD} for the same $q = 2$ mode used for the measurement presented above and a detuning of $\delta^{\nu} = \Delta\nu_{\mathrm{crit}}$. This measurement yields a thermal relaxation time of $\tau_{\mathrm{therm}} = 13 - 15$ ms, consistent with results obtained for the thermal relaxation time in microspheres [Tap02].
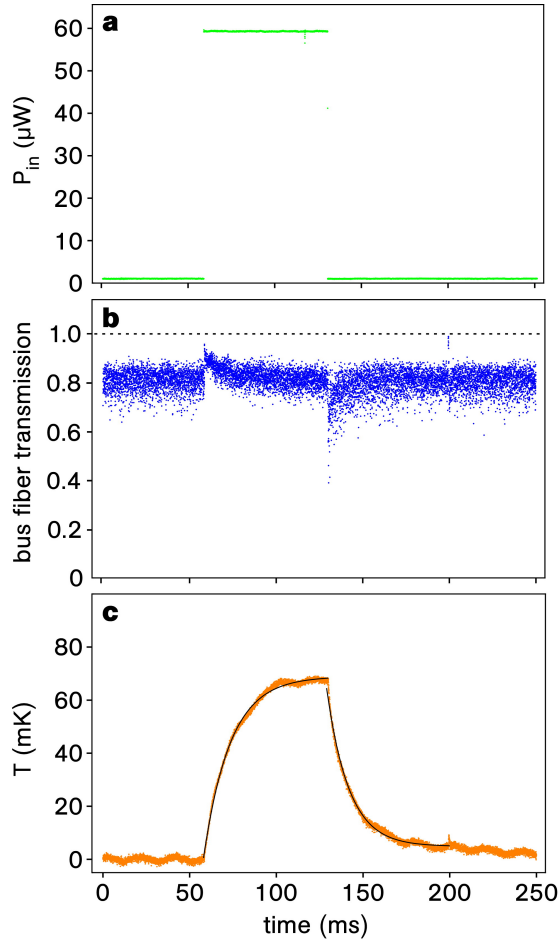
Figure 4.13: Measuring the thermal relaxation time of the mode volume of a $q = 2$ bottle mode with a linewidth of $\Delta\nu_{\mathrm{crit}} = 6.5$ MHz. (a) A rectangular 70 ms pulse in P_{in} heats the mode volume of the bottle mode. This pulse is compensated using a second AOM behind the bus fiber output, so that the photodiode signal detected behind this AOM is proportional to the transmission $T = P_{\mathrm{out}}^{\mathrm{bus}}(t)/P_{\mathrm{in}}(t)$ through the ultra-thin bus fiber waist. This signal is used as the error signal for the PI control loop that keeps the resonator–laser detuning constant. (b) Bus fiber transmission during the measurement calculated from the photodiode signal. In order to obtain the bus fiber transmission, the signal is normalized to its value measured with the bus fiber pulled away from the resonator and the lock disabled. The set point of the lock corresponds to $\delta^{\nu} = \Delta\nu_{\mathrm{crit}}$ and $T = 0.8$. The maximum and minimum values of $T = 0.95$ and $T = 0.4$ observed reveal, that the PI control loop maintains a laser–resonator detuning between $\delta^{\nu} = 2.2 \times \Delta\nu_{\mathrm{crit}}$ and $\delta^{\nu} = 0.4 \times \Delta\nu_{\mathrm{crit}}$ during the measurement. (c) The temperature of the mode volume, T_{mode}, as calculated from the control signal fed from the PI control loop to the laser current modulation input. Exponential fits (black curves) yield relaxation time constants of $\tau = (15.40 \pm 0.04)$ ms for the heating of the mode volume, when the pulse is applied, and of $\tau = (12.78 \pm 0.05)$ ms for its cooling, after the pulse. The maximum relative temperature change of approximately 70 mK corresponds to a shift in ν_0 of $34 \times \Delta\nu_{\mathrm{crit}}$.
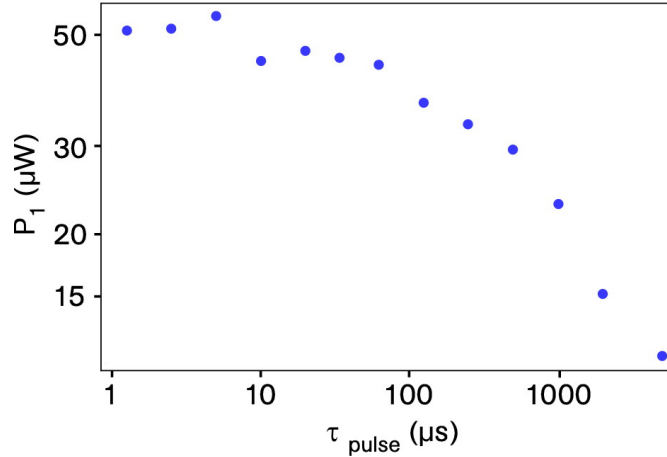
Figure 4.14: Dependency of the threshold power for optical bistability on the FWHM duration of the input pulses. This measurement is taken without the drop fiber. For pulse durations shorter than 100 μs, the quasi-instantaneous Kerr effect dominates the thermo-optical effect due to the finite thermal relaxation time ($\tau_{\mathrm{therm}} \sim 15$ ms) of the resonator mode. ON-OFF switching of the transmission through the bus fiber via the Kerr effect is achieved at a threshold power of 50 μW.

Identifying the Kerr regime

Again using the setup show in Fig. 4.10, the threshold P_1 as a function of τ_{pulse} is measured. For simplicity, the drop fiber is omitted in this measurement. The measurement results are shown in Fig. 4.14. For short pulse durations below 50 μs, the threshold power at the resonator fiber coupling junction has a constant value of about $P_1 = 50$ μW. For longer pulses, a strong decrease of the threshold power is observed. This is attributed to the onset of thermal effects which are known to dominate over the Kerr effect for pulse durations that are longer than the thermal relaxation time of the resonator mode [Rok05]. The fact that P_1 does not depend on the pulse duration for short pulses is a strong indication that the quasi-instantaneous Kerr effect is the prevailing non-linear mechanism and that thermal effects can be neglected for high switching speeds. For pulse durations $\tau_{\mathrm{pulse}} \ll \tau_{\mathrm{therm}}$, switching is therefore exclusively due to the Kerr effect. For pulse durations $\tau_{\mathrm{pulse}} \gg \tau_{\mathrm{therm}}$, one expects a second plateau of P_1. However, such pulse durations are inaccessible in this experiment because the drift of the laser–microresonator detuning in the absence of active stabilization is too large at these time scales. The threshold of $P_1 = 50$ μW, measured here, is consistent with powers for which Kerr bistability was previously observed in microspheres with comparable quality factors at cryogenic temperatures via deformation of the line shape [Tre98] and with the threshold power estimated using Eq. (4.19).
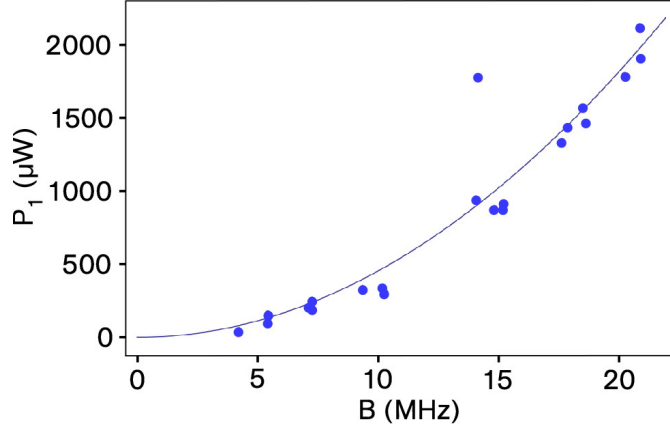
Figure 4.15: Variation of the switching threshold as a function of the resonator bandwidth. The solid line is a square-law fit ($P_1 = a_0 B^2$) to the experimental data, confirming the quadratic dependency. This means that P_1/B^2 is constant at a value of $a_0 = (4.75 \pm 0.20) \ \mu\text{W/MHz}^2$.

4.2.7 Switching speed

In principle, the Kerr effect allows one to realize extremely high switching speeds, corresponding to bandwidth in the THz regime, due to its sub-picosecond response time [Liu05]. In resonator-based switching schemes, however, the speed is limited by the -3 dB bandwidth of the resonator, given by $B = \Delta\nu_{\text{load}} = \nu_0/Q_{\text{load}}$. This means that the switching speed can be raised at the expense of reducing Q_{load} which will in turn increase the switching threshold, $P_1 \sim Q_{\text{load}}^{-2}$. The set-up used here, allows one to investigate this mechanism. By changing the gap between the resonator and the drop fiber while simultaneously adjusting the bus fiber gap to maintain critical coupling, Q_{load} can be varied over a wide range. Figure 4.15 shows the dependency of P_1 on B. As expected, the ratio of P_1/B^2 is constant at a value of $(4.75 \pm 0.20) \ \mu\text{W/MHz}^2$. All-optical signal processing is thus possible within the rage of bandwidth accessible with this method, albeit at higher threshold powers. For example, a switch with a bandwidth of 1 GHz will require a threshold power of around 4.75 W.

4.2.8 Discussion

The threshold power for all-optical ON-OFF switching of $P_1 = 50 \ \mu\text{W}$ inferred from the measurement in Fig. 4.14, is to the best of my knowledge, the smallest value ever reported for single-wavelength switching via the Kerr effect. Moreover, the figure of merit for resonator-based switching schemes $P_1/B^2 = 4.75 \ \mu\text{W/MHz}^2$ of the bottle microresonator aligns with the systems discussed in section 4.2.3 and is only around one order of magnitude higher than the lowest value stated there. However, as demonstrated in section 4.2.5, the bottle microresonator can also be employed for switching between two fiber outputs, albeit at higher threshold powers. In contrast, for the systems with comparable P_1/B^2-ratios discussed above, only ON-OFF switching of the transmission

through a single waveguide was demonstrated. Switching signals between two fiber outputs is an essential prerequisite for all-optical signal processing, as will be demonstrated next.

4.3 All-optical signal processing in bottle microresonators

In the following, all-optical signal processing functionalities are realized using the system characterized above, together with the setup depicted in Fig. 4.10. Routing of the signal beam is achieved by setting P_{in} to a value either below or above the bistable regime. Moreover, for a value of P_{in}, chosen within the bistable regime, two stable states at the outputs are possible. The actual state only depends on the history of the system. This enables the realization of an optical memory.

In the experiments that will be presented next, the system is operated at switching rates around 1 MHz. At the end of this section, the possibility of extending this all-optical signal processing functionalities to GHz rates while maintaining moderate input powers is discussed. It is shown that coating the bottle microresonator with a nonlinear polymer presents a promising route towards high-bandwidth all-optical signal processing.

4.3.1 State of the art – optical routing and memories

All-optical routing

As pointed out above, all previous bistable single-wavelength schemes only demonstrated ON-OFF switching. Single-wavelength all-optical routing of a pulsed signal was demonstrated in an interferometric switch incorporating a microring resonator [Hee04]. Intense laser pulses, corresponding to peak powers of 40 W, were necessary to operate this device.

Optical memory

Single-wavelength optical memories have so far been realized with microring resonators using thermally induced bistability [Alm04a] and with etalons using free carrier nonlinearities [He93]. In both cases, only ON-OFF functionality was demonstrated since no drop channel was implemented.

4.3.2 All-optical routing and optical memory in bottle microresonators

First, routing of a continuous wave signal between two output channels using a single-wavelength scheme is demonstrated. The loaded quality factor is chosen to be $Q_{\text{load}} = 1.5 \times 10^7$ at critical coupling, which corresponds to a reduction in the intrinsic quality factor of $Q_0/Q_{\text{load}} = 12$, ensuring a reasonably high power transfer efficiency of $E = 0.83$. The laser frequency is initially locked to the mode with a detuning of $\delta_0^{\nu} = -1.2 \times \Delta\nu_{\text{crit}}$ from resonance. The desired temporal profile of P_{in} is stored in the memory of the computer controlled arbitrary waveform generator and is applied together with a pulse sent to the sample-and-hold circuit disabling the lock during the experiment. As already mentioned above, in order to characterize the performance of the system as a whole,
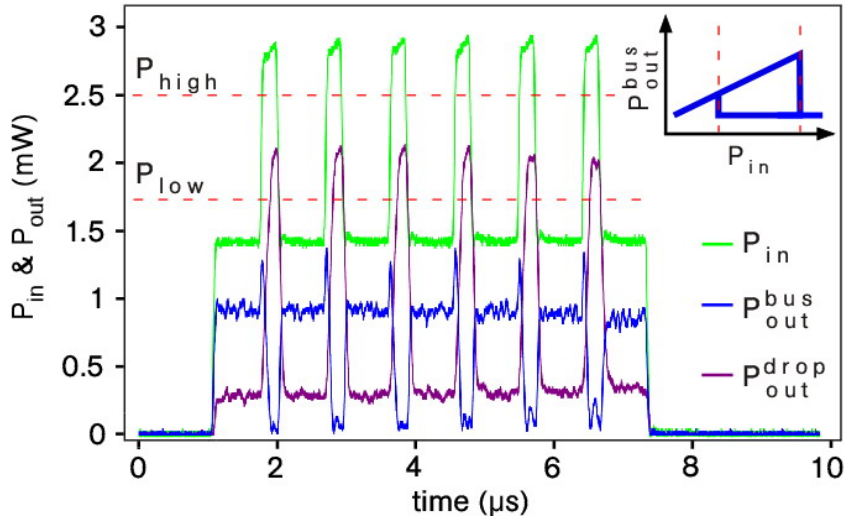
Figure 4.16: Demonstration of all-optical routing using the optical Kerr bistability in a bottle microresonator. P_{in} is varied between two levels which are located below and above the bistable regime, delimited by P_{low} and P_{high}, (schematically indicated by the dashed lines) as shown in the inset. At the same time, the power at the outputs of the bus fiber and the drop fiber is monitored. As soon as the input power exceeds P_{high}, 70% of the incident light is transferred to the output of the drop fiber. Lowering the input power below P_{low}, again reverses the situation at the outputs.

the powers quoted here refer to the values launched into the input of the bus fiber and detected at the outputs of the bus and the drop fibers. For simplicity, the notation used above is kept and these values are denoted by P_{in}, $P_{\text{out}}^{\text{bus}}$ and $P_{\text{out}}^{\text{drop}}$. Consequently, P_{low} and P_{high} also refer to values at the input of the bus fiber. Figure 4.16 shows the realization of all-optical routing, for which the signal beam is repeatedly switched between the bus and the drop fiber at a rate of 1 MHz. When abruptly changing P_{in} from a value below to a value above the bistable regime, about 70% of the power launched into the bus fiber exits the drop fiber. The modulation depth between the HIGH-state and the LOW-state power levels at both outputs is 9 dB. To the best of my knowledge, this is the first time that a continuous wave signal has been routed between two output channels using a single-wavelength scheme.

Due to its bistability, the system used here can also be operated as a so-called "optical memory". For this purpose, an operating power $P_{\text{in}} = P_{\text{bist}}$ of approximately 2 mW, which is centered in the bistable regime, is chosen, see Fig. 4.17. At this power, the system exhibits two stable output states. Changing P_{in} to a power higher than P_{high} or lower than P_{low} switches between these two states. When returning to P_{bist}, the system then stays in the chosen state. In contrast to the systems cited above, the optical memory realized here is a true add-drop device, meaning that it allows one to route a signal between its two output ports. Since the optical memory is operated in the bistable regime, it is quite sensitive to thermal fluctuations and drifts. Therefore,
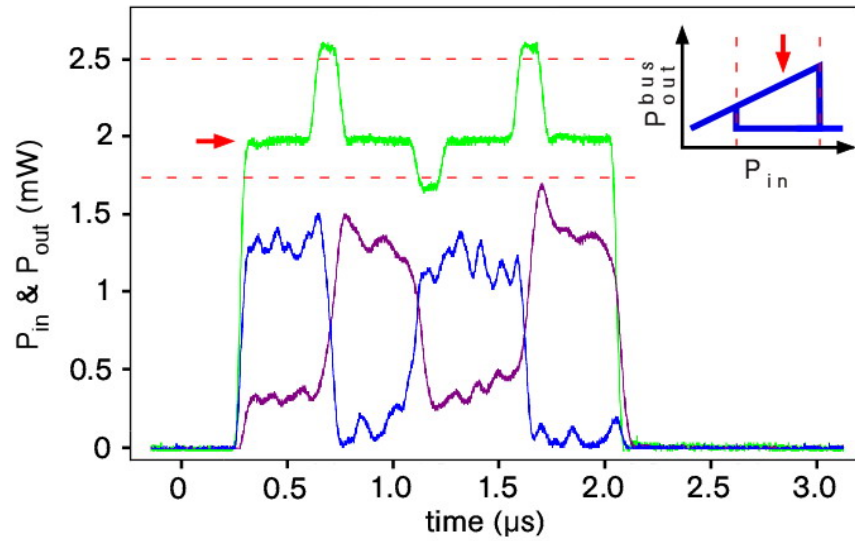
Figure 4.17: Demonstration of optical memory functionality in a bottle microresonator using the Kerr effect. For an input power level (green) in the bistable regime (as indicated by the arrow) the power at the outputs of the bus fiber (blue) and of the drop fiber (purple) exhibits two stable states. The output state is chosen by temporarily lowering (raising) P_{in} below (above) the bistable regime, which is schematically indicated by the dashed lines.

the residual absorption of the signal light field currently limits the storage time of this optical memory to the sub-microsecond range. A similar limiting effect has also been reported for optical memory based on etalons using free carrier nonlinearities [He93].

4.3.3 Towards high-bandwidth all-optical signal processing using coated bottle microresonators

As pointed out above, the bandwidth of the bottle microresonator can in principle be increased to the GHz range, making it an interesting device for applications in telecommunication. However, in order to do so, the quality factor has to be reduced by several orders of magnitude, meaning that the favorable ratio of α^2/n_2 of silica that is responsible for the ultra-low switching powers observed above, is no longer beneficial. Therefore, in high-bandwidth applications, a higher value of n_2, even when accompanied by a higher absorption, can improve the performance of the switch in terms of the P_1/B^2-ratio. In the following, a silica bottle microresonator coated with the nonlinear polymer MEH-PPV, whose properties are given in Tab. 4.2, will be investigated under this aspect.

Estimating the performance of a MEH-PPV coated bottle microresonators

First, the radial intensity distribution at the caustics of a bottle microresonator with caustic radius $R_s = 17.5$ μm and a polymer coating of thickness d is calculated by solving the radial wave equation at the caustics. From the intensity distribution of the modes it is possible to infer the enhancement of the nonlinear refraction with respect to an uncoated silica resonator ($d = 0$). The discussion is limited to TM modes, because in waveguides of MEH-PPV, n_2 is found to be higher if the light is polarized parallel with respect to the substrate carrying the polymer [Koy06]. Moreover, the calculation is performed for a wavelength of 1080 nm, for which n_2 of MEH-PPV is maximal. The overall radius of the coated resoantor is denoted by $R_p = R_s + d$. The refractive indices are given by $n_s = 1.467$ and $n_p = 1.65$ [Koy06] in both materials. The radial wave function in silica and in the surrounding air are identical to that of an uncoated system. In the polymer, the general solution of the radial wave equation, given by Eq. (2.12), has to be considered

$$E_z \propto A \cdot J_m\left(k_s \cdot r\right) \ , \hspace{2cm} \text{for } r \leq R_s \ . \hspace{1cm} (4.29)$$

$$E_z \propto B \cdot J_m\left(k_p \cdot r\right) + C \cdot Y_m\left(k_p \cdot r\right) \ , \hspace{1cm} \text{for } R_s \leq r \leq R_p \ . \hspace{1cm} (4.30)$$

$$E_z \propto D \cdot Y_m\left(k_0 \cdot r\right) \ , \hspace{2cm} \text{for } r \geq R_p. \hspace{1cm} (4.31)$$

The wave numbers in the different media are given by $k_s = n_s k_0$ and $k_p = n_p k_0$. For the following calculation, the coefficient B in the second of the above equations is set to unity. In order to solve for the wavelength for which the resonance condition is fulfilled, one again uses the continuity of E_z and its derivative $H_\phi = -i/(\mu\omega)\partial_r E_z$ at both interfaces. In analogy to Eq. (2.22) for an uncoated resonator, one obtains a set of two equations

$$F_1(\lambda, C) = \frac{n_s J'_m\left(k_s R_s\right)}{J_m\left(k_s R_s\right)} - \frac{n_p\left(J'_m\left(k_p R_s\right) + C Y'_m\left(k_p R_s\right)\right)}{J_m\left(k_p R_s\right) + C Y_m\left(k_p R_s\right)} = 0 \ , \hspace{1cm} (4.32)$$

$$F_2(\lambda, C) = \frac{Y'_m\left(k_0 R_p\right)}{Y_m\left(k_0 R_p\right)} - \frac{n_p\left(J'_m\left(k_p R_p\right) + C Y'_m\left(k_p R_p\right)\right)}{J_m\left(k_p R_p\right) + C Y_m\left(k_p R_p\right)} = 0 \ . \hspace{1cm} (4.33)$$

The solutions are given by the intersection of $F_1(\lambda, C)=0$ and $F_2(\lambda, C)=0$ in the two-dimensional parameter space (λ, C). A counter plot of $F_1(\lambda, C)=0$ and $F_2(\lambda, C)=0$ helps to identify the lowest order radial modes. Both equations are then numerically solved with properly chosen start values for λ and C. Next, the amplitudes A and D can be derived from the continuity of E_z at the interfaces. In order to allow one to compare between the solution for different film thickness d for a constant value of P_{in}, the intensity distributions are normalized

$$I_{\text{norm}}(r, d) = \frac{|E_z(r, d)|^2}{\int_0^{R_{\text{rad}}} |E_z(r, d)|^2 r dr} \ . \hspace{1cm} (4.34)$$

For each thickness d, the enhancement of the nonlinear refraction with respect to an uncoated resonator ($d = 0$) can be calculated by

$$f = \frac{\int_0^{R_{\text{rad}}} n_2(r) I_{\text{norm}}(r, d) r dr}{\int_0^{R_{\text{rad}}} n_2(r) I_{\text{norm}}(r, 0) r dr} \ . \hspace{1cm} (4.35)$$
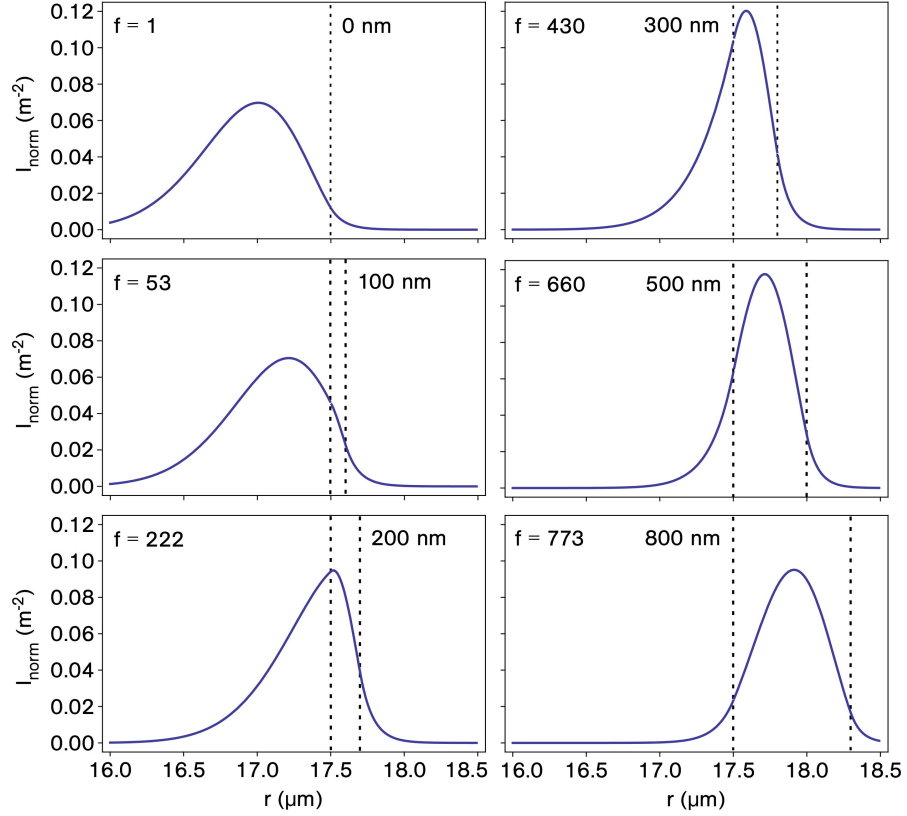
Figure 4.18: Normalized intensity distribution of the fundamental radial modes at wavelengths around 1080 nm in a 35-μm silica WGM resonator coated with a polymer exhibiting a nonlinear refractive index that is 815 times higher than that of the resonator material. The nonlinear refraction is enhanced by a factor f with respect to the uncoated silica resonator.

Figure 4.18 shows the radial intensity distribution calculated for different thicknesses of the polymer coating ranging from $d = 0$ to $d = 800$ nm for wavelengths around 1080 nm. Note the "radial compression" of the mode and the enhanced relative peak intensity which is maximal for the plots with $d = 300$ nm and $d = 500$ nm. Finally, the performance of a bottle microresonator coated with a 800 nm thick polymer film at a wavelength of 1080 nm is estimated. Assuming an absorption limited intrinsic quality factor of $Q_0 = 8 \times 10^5$ for the polymer (Tab. 4.2), which, according to Eq. (4.7), would reduce to $Q_{\text{load}} = 4 \times 10^4$ in an add-drop filter with transfer efficiency of 90%, results in a bandwidth of $B = 7$ GHz. For the uncoated 36–μm diameter silica resonator for which $P_1/B^2 = 4.75~\mu$W/MHz^2 was measured, the same bandwidth requires a threshold power of $P_1 = 233$ W. Using Eq. (4.19), the corresponding switching threshold for a resonator with a 800 nm thick MEH-PPV coating would then reduce to $P_1 = 268$ mW, resulting in $P_1/B^2 = 5.3$ nW/MHz^2.

First experimental results in fabrication of MEH-PPV coated bottle microresonators

The polymer coated bottle microresonators used in this work were fabricated using a dip coating technique. The resonator fiber is vertically immersed into a solution of MEH-PPV in toluol or chloroform with concentrations of 5–10 weight percent. After a time t_{im}, the fiber is pulled out of the solution at a defined speed v_w of several mm/s. By variation of the solvent, the polymer concentration, t_{im} and v_w, coatings with a maximal thickness of 140 nm are realized. The film thickness is measured by scratching the film with a needle and scanning the surface perpendicular to the scratch with a surface profiler (KLA Tencor, P-16+).

The spectral properties of the coated resonators are investigated with the DFB laser at a wavelength of 850 nm. In a resonator with a coating of $d = (95 \pm 5)$ nm thickness, typical quality factors of 3×10^5 to 5×10^5 are observed for TM polarization. From a loss coefficient of 200 m^{-1}, measured in MEH-PPV waveguides at the given wavelength [Koy02], an absorption limited quality factor of 6×10^4 is calculated. The measured quality factors are significantly higher than this value. Assuming the radial intensity distribution of the fundamental mode for $d = 95$ nm, see Fig. 4.19 (a), this can be explained by its small spatial overlap with the polymer film. If the modes under investigation are higher order radial modes, the actual overlap between the radial intensity distribution, see Fig 4.19 (b), and the polymer, as well as the intensity at the resonator surface would even be smaller. This would lead to relatively high quality factors even for high surface roughness. In turn, this higher order modes would not show a significant enhancement of the nonlinear refraction. Unfortunately, the available powers of few mW are not sufficient to investigate the threshold power for optical bistability
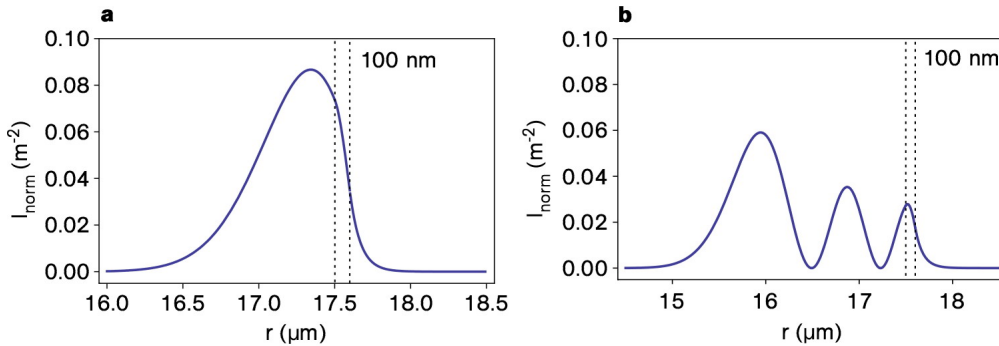

Figure 4.19: (a) Normalized radial intensity distribution of the fundamental radial mode for a wavelength around 850 nm in a silica WGM resonator with a diameter of 35 μm and a polymer coating of thickness $d = 100$ nm. At this wavelength the overlap of the radial intensity distribution with the polymer film is larger than for the same coating thickness and $\lambda = 1080$ nm (Fig. 4.18). (b) Higher order radial mode in the same resonator. The overlap of the radial intensity distribution with the polymer film is much smaller than for the fundamental radial mode. This results in both, less absorption and a smaller enhancement of the nonlinear refraction. Moreover, the intensity at the surface is about a factor of two smaller than for the fundamental mode.

for the measured quality factors. Such a measurement would be necessary in order to ensure that the modes under investigation are indeed fundamental radial modes with an intensity distribution that significantly overlaps with the polymer.

4.4 Conclusion

In this chapter, I investigated optical add-drop filters and all-optical switches which are based on bottle microresonators, evanescently coupled to two sub-micron diameter fibers. The ultra-thin fiber coupling method introduces only very small losses and allows one to adjust the fiber-resonator coupling at will by varying the fiber-resonator gap. This enabled a systematic study of the power transfer efficiency of the add-drop filter as a function of its linewidth or, equivalently, its quality factor. Close agreement between the data and the theoretical prediction was found and a power transfer efficiency of up to 93% was realized for a filter linewidth of only 49 MHz, corresponding to a loaded quality factor as high as 7.2×10^6.

The favorable ratio of absorption losses to nonlinear refractive index of silica, enabled the observation of optical bistability due to the Kerr effect at a record low threshold of 50 μW. Single-wavelength all-optical switching of light between two standard optical single mode fibers with an overall efficiency of 70% was demonstrated at rates of up to 1 MHz. This bandwidth depends on the loaded quality factor of the resonator and increases when this quality factor decreases. However, the increased bandwidth comes at the expense of an increased switching threshold. The corresponding dependency was investigated, yielding a close agreement with the predicted square law. Moreover, it was shown that the bottle microresonator coupled to two fibers can also be operated as an optical memory that allows switching between its two bistable states with a single-wavelength signal which was accordingly routed to one of the two output ports. Finally I proposed the possibility to apply this all-optical signal processing functionalities to GHz rates used in modern telecommunication devices, while at the same time maintaining moderate threshold powers.

5 Outlook – bottle microresonators in cavity quantum electrodynamics

The field of cavity quantum electrodynamics (CQED) was initiated in 1946 when E.M. Purcell suggested that by coupling a system exhibiting a magnetic transition at radio frequencies to a resonant electrical circuit the rate of spontaneous emission can be significantly enhanced [Pur46]. In modern CQED experiments, single atoms interact with optical cavity modes in the regime of strong coupling, in which the atom-cavity interaction is much larger than the dissipative mechanisms given by the cavity field decay rate and the atomic dipole decay rate. Possible future applications of optical CQED systems include the realization of quantum networks [Kim08] and quantum computation [Dua04]. In this chapter, first a brief overview of the theoretical description of the interaction of a single atom with a single cavity mode as described by the Jaynes-Cummings model is given. The spectral characteristics of a real atom-cavity system in the presence of dissipation, probed by a weak light field can be derived using the density matrix formalism. The coupling rate between a cesium (Cs) atom and a bottle mode is calculated based on the wave functions and mode volumes derived in chapter 2. It is shown, that in conjunction with the quality factors demonstrated in chapter 3, light matter interaction deep within the strong coupling regime should be possible. The bottle microresonator in add-drop configuration, according to the findings from chapter 4, compares favorably to state-of-the-art CQED systems based on Fabry-Pérot resonators or microtoroidal resonators. In particular, it offers a unique combination of excellent CQED parameters, tunability, frequency stability and advantageous coupling characteristics to external light fields. Finally, nonlinearities at the single-photon level in a strongly-coupled cavity–atom system are discussed.

5.1 Strong coupling between one atom and a bottle mode

5.1.1 Jaynes-Cummings model

The interaction between a single two-level atom and a cavity mode is described by the Jaynes-Cummings model [Coh92, Ber94, Dot07]. The Hamiltonian for an atom coupled to a cavity mode consists of three terms, that describe the cavity, the atom and their interaction

$$H = H_{\text{atom}} + H_{\text{cavity}} + H_{\text{int}} . \tag{5.1}$$

The eigenstates of the atom are denoted by $|g\rangle$ (ground state) and $|e\rangle$ (excited state). Both states are energetically separated by $\hbar\omega_a = h\nu_a$, where ν_a is the optical resonance frequency of the atom. The atomic raising and lowering operators $\sigma^\dagger = |e\rangle\langle g|$ and

$\sigma = |g\rangle \langle e|$ describe the excitation and de-excitation of the atom. The cavity mode is described by the photon number states $|n\rangle$. The energy spacing between adjacent states is determined by the optical resonance frequency of the cavity, ν_c, via $h\nu_c = \hbar\omega_c$. The energy of the cavity field can be derived form $H_{\text{cavity}} = \hbar\omega_c \left(a^\dagger a + 1/2\right)$, where the photon number operator is the product of the field creation and annihilation operators $a^\dagger$ and a. The dipole interaction between the electric field of the cavity mode and the atomic dipole moment, $\vec{d}$, is described by the coupling rate g. It is a function of the position $\vec{r}_{\text{at}}$ of the atom with respect to the cavity field that is given by $\vec{E}(\vec{r}) = E_0\vec{\Psi}(\vec{r})$, where E_0 is the peak cavity field strength and $\vec{\Psi}$ is the spatial mode function, which is normalized to unity. The peak value of the coupling rate as well as its spatial variation is then given by

$$g_0 = \frac{E_0 d}{2\hbar} \qquad \text{and} \qquad g(\vec{r}) = g_0|\vec{\Psi}(\vec{r})| \; . \tag{5.2}$$

Using the rotating wave approximation, the Hamiltonian can then be written as

$$H = \hbar\omega_a\sigma^\dagger\sigma + \hbar\omega_c \left(a^\dagger a + 1/2\right) + \hbar g \left(\sigma^\dagger a + \sigma a^\dagger\right) \; . \tag{5.3}$$

Diagonalizing H yields the new eigenstates and energy eigenvalues of the coupled system on resonance $(\omega_c = \omega_a = \omega)$

$$|\pm, n\rangle = (|g\rangle |n\rangle \pm |e\rangle |n-1\rangle) / \sqrt{2} \; , \tag{5.4}$$

$$E_{\pm,n} = n\hbar\omega \pm \sqrt{n}\hbar g \; . \tag{5.5}$$

In the absence of the dipole interaction, the states $|g\rangle |n\rangle$ and $|e\rangle |n-1\rangle$ have identical energies $n\hbar\omega$. As is apparent from Eq. (5.5), the interaction lifts this degeneracy and shifts the energy of the new eigenstates. Their energy splitting $2\hbar\sqrt{n}g$ is called Rabi splitting. The Rabi frequency $\Omega_n = 2\sqrt{n}g$ describes the coherent transfer of energy between the cavity and the atom.

5.1.2 Density matrix formalism

In a real cavity-atom system that is not isolated from the environment, energy is dissipated due to the leakage of photons from the cavity and spontaneous emission from the atom to propagating modes. Intuitively, it is clear that the properties of the isolated cavity-atom system described above are experimentally only observable when the rate of energy transfer between the atom and the cavity, described by g, is much larger than the cavity field decay rate $\kappa = 1/(2\tau_{\text{crit}}) = \omega_c/2Q_{\text{crit}}$, and the transverse atomic dipole decay rate $\gamma_\perp$. Note that the cavity field decay rate and the transverse atomic dipole decay rate only show half the value of the energy decay rates τ_{crit}^{-1} and $\Gamma = 2\gamma_\perp$, which determine the linewidth of the cavity mode and of the atomic transition. Quantitatively, the so-called regime of strong coupling between an atom and the cavity mode is defined via $g^2/(\kappa\gamma) \gg 1$. In a simple picture, in this regime a photon can be exchanged between the cavity and the atom many times before it is lost due spontaneous emission

or its finite lifetime in the cavity. Rigorously, the coupled system in the presence of dissipation and a weak driving laser field $\varepsilon(t) = \varepsilon_0 \exp\left(i\omega_{\text{probe}}t\right)$ with angular frequency $\omega_{\text{probe}} = 2\pi\nu_{\text{probe}}$, used to probe the spectral properties of the system, is described by the density matrix formalism [Coh92,Ber94,Dot07]. The Jaynes-Cummings Hamiltonian now includes driving of the cavity by the probe laser and its from in a frame rotating at ω_{probe} is given by

$$H = \hbar\left(\omega_a - \omega_{\text{probe}}\right)\sigma^\dagger\sigma + \hbar\left(\omega_c - \omega_{\text{probe}}\right)a^\dagger a + \hbar g\left(a^\dagger\sigma + a\sigma^\dagger\right) + \hbar\varepsilon_0(a + a^\dagger) \ . \quad (5.6)$$

The dissipation is considered using the collapse operator $\hat{C} = \sqrt{2\gamma_\perp}\sigma + \sqrt{2\kappa}a$. The time evolution of the system is described by the equation

$$\frac{d\rho}{dt} = \mathcal{L}\rho \ , \quad (5.7)$$

using the atom–cavity density operator ρ and the Liouvillian $\mathcal{L}$, which is given by

$$\mathcal{L}\rho = -\frac{i}{\hbar}\left[H, \rho\right] + \hat{C}\rho\hat{C}^\dagger - \frac{1}{2}\hat{C}^\dagger\hat{C}\rho - \frac{1}{2}\rho\hat{C}^\dagger\hat{C} \ . \quad (5.8)$$

In general, a steady-state solution for $\rho(g, \kappa, \gamma_\perp)$ is computed numerically. The expectation value of a given operator $\hat{O}$ is then obtained from $\langle\hat{O}\rangle = \text{Tr}(\rho\hat{O})$. The following discussion will be restricted to the case of resonance between the cavity and the atom. The steady-state solution of Eq. (5.7) can then be derived analytically for the case of a weak driving field [Ros03]. The probability of finding a photon in the cavity and the population of the excited state of the atom is given by ρ_{11} and ρ_{22}, respectively. The solution is only valid for a weak driving field, where ρ_{11}, $\rho_{22} \ll 1$. For the following discussion, ρ_{11} is of special interest. In the case of $\omega_c = \omega_a = \omega$ and using the notation $\Delta\omega_{\text{probe}} = \omega_{\text{probe}} - \omega$, it is given by

$$\rho_{11} = \frac{\varepsilon_0^2\left(\gamma_\perp^2 + \Delta\omega_{\text{probe}}^2\right)}{\Delta\omega_{\text{probe}}^4 + \left(\kappa^2 + \gamma_\perp^2 - 2g^2\right)\Delta\omega_{\text{probe}}^2 + \left(\kappa\gamma_\perp + g^2\right)^2} \ . \quad (5.9)$$

5.1.3 Calculating the coupling rate

Next, the spectral characteristics of a system consisting of a single atom and a bottle mode will be investigated. In CQED experiments, it is common to use alkali atoms due to their simple energetic structure which makes them behave similar to a single-electron system. This can be intuitively understood by the simple shell model. Alkali metals have only one electron in the outer shell, which only weakly interacts with the electrons from the fully occupied inner shells. In the following, the D2 ($6^2S_{1/2} \to 6^2P_{3/2}$) transition in ^{133}Cs is considered. It exhibits a resonant wavelength of $\lambda_0 \approx 852.35$ nm and a transverse dipole decay rate of $\gamma_\perp = 2\pi \cdot 2.61$ MHz. The corresponding transition dipole matrix element is $\langle J = 1/2|\, er\, |J' = 3/2\rangle = 3.80 \cdot 10^{-29}$ Cm. The hyperfine structure of the $6^2S_{1/2}$ state and the $6^2P_{3/2}$ state gives rise to σ transitions between states ($F, m_f \to$

$F', m'_f = m_f \pm 1$) driven by circularly polarized light fields and π transitions of the form $(F, m_f \to F', m'_f = m_f)$, driven by linearly polarized light fields. In both cases, the dipole selection rules require that $F' - F = 0, \pm 1$. Since the bottle microresonator exclusively supports linearly polarized modes only, the latter case is taken into account here. The transition $(F = 4, m_f = 0 \to F' = 4, m'_f = 0)$ exhibits the largest dipole moment of $d = \sqrt{5/18} \langle J = 1/2 | er | J' = 3/2 \rangle = 2.00 \cdot 10^{-29}$ Cm [Ste98]. For a realistic analysis, the 35–μm diameter resonator, whose TE polarized $q = 1$ mode exhibited $Q_{\text{crit}} = 1.8 \times 10^8$ in the measurements presented in section 3.4.3 is considered. The corresponding cavity decay rate is $\kappa = 2\pi \cdot 0.98$ MHz. The last missing parameter for calculating the spectrum of the coupled system is the coupling rate g. Thus, in the following, the coupling rate for the first excited state of a coupled atom–cavity system is calculated. The energy of a bottle mode containing one photon is given by

$$W = \hbar \omega_c . \tag{5.10}$$

Comparing this equation with the expression for the electric energy of a bottle mode, $W = 1/2 \epsilon_0 E_0^2 V_{m,q}$, derived in section 3.2.1 yields

$$E_0 = \sqrt{\frac{2 \hbar \omega_c}{\epsilon_0 V_{m,q}}} . \tag{5.11}$$

The peak value of the coupling rate, according to Eq. (5.2), is then calculated to be

$$g_0 = d \sqrt{\frac{2 \pi^2 c_0}{h \epsilon_0 \lambda_0 V_{m,q}}} . \tag{5.12}$$

This means that the maximum coupling rate is only affected by the mode volume of the resonator, $g_0 \propto V_{m,q}^{-1/2}$. The mode volumes $V_{180,1}$ for the TM and TE polarized bottle modes in a 35–μm diameter resonator are given in Tab. 2.1. Together with a dipole moment of $2.0 \cdot 10^{-29}$ Cm this yields

$$\text{TM:} \quad g_0 = 2\pi \cdot 104 \text{ MHz} \qquad \text{and} \qquad \text{TE:} \quad g_0 = 2\pi \cdot 101 \text{ MHz} . \tag{5.13}$$

Figure 5.1 shows the radial dependency of the coupling rate for both modes calculated from $g(r) = g_0 |\vec{\Psi}(r, z = z_{\text{max}})|$. The z coordinate is chosen to coincide with the maximum in the axial intensity distribution located at $z_{\text{max}} < z_c$, according to Fig. 2.5. For a bottle resonator an atom can not be placed at the peak of the electric field strength which is located inside the silica structure. Therefore, the coupling rate close to the surface of the resonator is the crucial value. At the surface, the coupling rates for both modes reduce to

$$\text{TM:} \quad g_{\text{surf}} = 2\pi \cdot 40.1 \text{ MHz} \qquad \text{and} \qquad \text{TE:} \quad g_{\text{surf}} = 2\pi \cdot 50.0 \text{ MHz} . \tag{5.14}$$

These values result in a ratio of $g^2/(\kappa \gamma_\perp)$ of 630 and 980, respectively, enabling light-matter interaction deep within the regime of strong coupling. The discontinuity in the
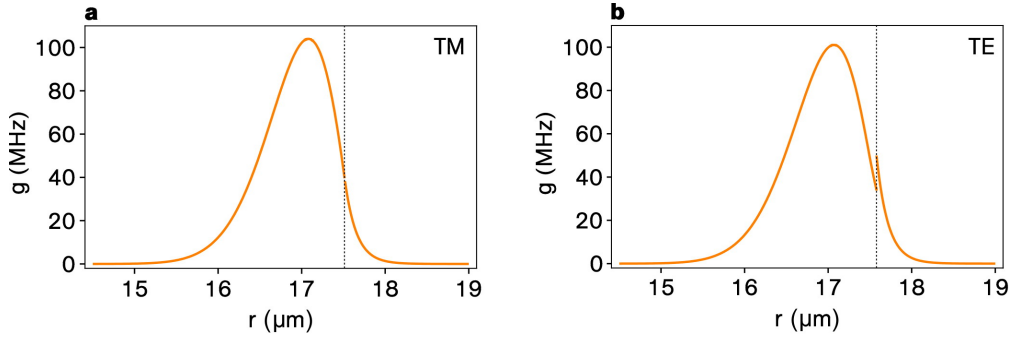
Figure 5.1: Calculated radial dependency of the coupling rate g for the fundamental TM (a) and TE (b) polarized $q = 1$ bottle modes in a 35–μm diameter resonator.
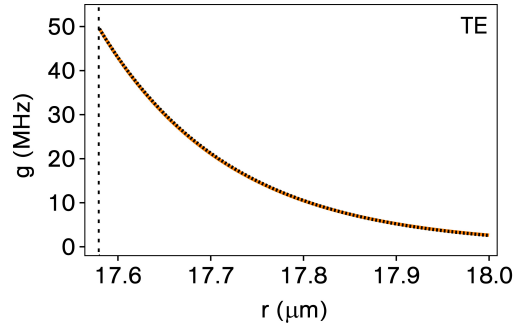

Figure 5.2: Spatial variation of the coupling rate close to the resonator surface for the TE polarized mode from Fig. 5.1 (b). At the surface, (vertical, dashed line) g has a maximum value of $g_{\text{surf}} = 2\pi \cdot 50.0$ MHz which decreases with the distance from the surface d. For the given parameters, an exponential decay, according to $g(d) = g_{\text{surf}} \cdot \exp\left(-d/d_0\right)$, with spatial decay length $d_0 = 142$ nm (dashed, black line) is a good approximation of the result of the rigorous calculation in the region of interest given by a Bessel function.

TE polarized electric field at the resonator surface leads to a enhancement of g close to the surface by a factor of 1.25, despite its slightly larger mode volume and therefore smaller value of g_0 as compared to the TM polarized bottle mode. Figure 5.2 shows the spatial variation of the coupling strength close to the resonator surface for the TE polarized mode. Unfortunately, an atom adsorbed on the resonator surface will show drastically altered spectral properties and strong coupling can only be obtained with a sufficiently large spacing between the atom and the resonator surface. For microtoroidal resonators it was found that the atom is strongly perturbed by the van der Waals (vdW) interaction for distances up to 45 nm from the surface [Aok06]. Thus, the exact value of the coupling rate for the given experimental spacing has to be calculated from g_{surf} and the spatial decay length d_0.

Figure 5.3 (a) shows ρ_{11} as a function of the probe laser detuning for a Cs atom coupled to the TE polarized mode with parameters as discussed above. Figure 5.3 (b) shows ρ_{11} for the equivalent mode, but with the quality factor reduced by a factor of
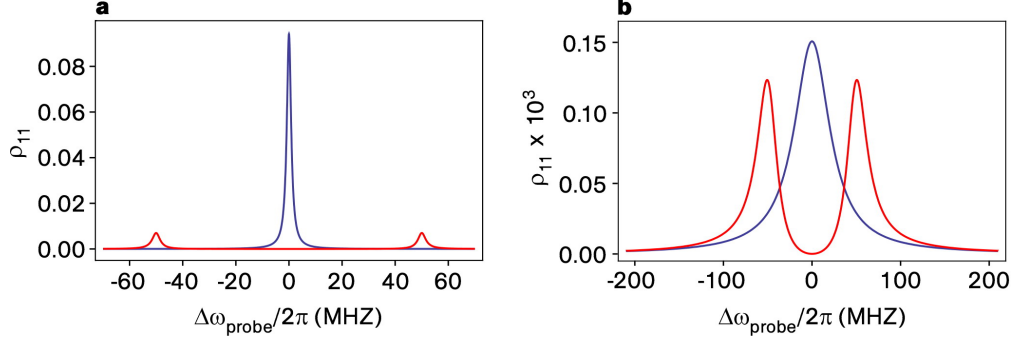
Figure 5.3: Probability of finding a photon in a bottle mode ρ_{11}, with ($g = 2\pi \cdot 50$ MHz, red line) and without ($g = 0$, blue line) interaction between the bottle mode and the atom. In (a) the parameters are set to $\varepsilon_0 = 2\pi \cdot 0.3$ MHz, $\kappa = 2\pi \cdot 0.98$ MHz, $\gamma_\perp = 2\pi \cdot 2.61$ MHz. In (b) $\kappa = 2\pi \cdot 24.4$ is increased according to $Q_{\mathrm{crit}} = 7.2 \times 10^6$ MHz which is a typical value for a bottle microresonator in add-drop configuration.

25 to $Q_{\mathrm{crit}} = 7.2 \times 10^6$ MHz. This reduction in the quality factor would yield a power transfer efficiency of $E \approx 0.96$ in add-drop configuration, while maintaining $\kappa = 2\pi \cdot 24.4$ and $g^2/\kappa\gamma_\perp \approx 40$. In the absence of an interaction between the atom and the bottle mode, ρ_{11}, which is proportional to the intracavity energy $|a|$, has a Lorentzian–shaped profile with a FWHM of $\Delta\omega = \tau_{\mathrm{crit}}^{-1} = 2\kappa$, consistent with the results obtained in section 3.2.1. In the presence of the atom, the spectrum consists of two peaks separated by an angular frequency of $2g$. The ratio between the maximum values of ρ_{11} with and without interaction is given by $(\kappa/(\kappa+\gamma_\perp))^2$. Assuming a spectral linewidth of the weak probe light field of around 1 MHz and $\Delta\omega_{\mathrm{probe}} = 0$, the contrast between the intracavity energy with and without interaction is larger than $\rho_{11}(g = 2\pi \cdot 50 \text{ MHz})/\rho_{11}(0) = 1/1000$, for both cases observed in Fig. 5.3.

5.2 Comparing bottle microresonators with state-of-the-art CQED systems

Cavity quantum electrodynamics with single atoms has been intensively studied using Fabry-Pérot microresonators. Dielectric cavity mirrors with reflectivity on the order of 99.9997% [Khu08], allow one to enter the strong coupling regime for waist sizes on the order of few tens of micrometers and mirror separations on the same length scale. The modular design of an FP resonator enables free tunability over a longitudinal free spectral range and therefore ensures matching of a appropriate cavity mode with the atomic transition frequency. The cavity field is easily accessible and atoms can be placed and trapped within it by using, e.g., optical dipole traps. However, these system also suffer from a number of drawbacks. The losses of the dielectric mirror coatings are on the order of their transmission and, therefore, the coupling of light into and out of the cavity is inefficient. Dielectric mirror coatings with the required reflectivity are cutting-edge technology and very costly. Moreover, the modular design, which eases

tunability, requires active stabilization of the mirror separation on a sub-picometer length scale [Khu08].

In the following, bottle microresonators are compared with resonators optimized for single atom CQED experiments, i.e., FP resonators and microtoroidal resonators.

5.2.1 Placing and trapping atoms within the mode volume

The mode of an FP resonator, which is located in free space between both mirrors, is easily accessible. In early experiments, transits of atoms dropped from a MOT located above the cavity through the mode volume were observed by altered transmission properties of a weak probe beam resonant with the cavity mode and the atomic transition [Mab96] caused by the Rabi splitting. In [Boc04], a single atom was trapped in an FP microresonator using an intracavity dipole trap created by an auxiliary cavity mode far detuned from the atomic resonance frequency. Due to the standing wave structure of the intracavity field, such a dipole trap forms several potential wells along the cavity axis. A Raman scheme was used in order to further cool the atomic motion and thus to prevent variation in the coupling strength $g(r)$ along the cavity axis. The cooling beams were shone in at an angle of $90°$ with respect to the cavity axis. Using this method, the axial position was stabilized to $\Delta z = 33$ nm while the transverse localization was $\Delta \rho = 5.5$ μm. For this system, it was possible to measure the Rabi splitting for a single atom placed in the cavity in a single sweep of the probe laser frequency over the systems resonance. Another approach for controlled insertion of atoms into an FP cavity is to use an external standing wave dipole trap, perpendicularly oriented to the cavity axis. For this purpose two counter-propagating laser beams are tightly focused into the cavities mode volume. The potential wells of the resulting standing wave can be shifted in space by detuning the relative frequency of the counter-propagating beams. The trapped atoms are moved along with the potential wells and thus can be inserted and retrieved from the cavity [Hij07, For07, Khu08]. In [Hij07] the coupled atom–cavity system was used as a triggered single-photon source. A single atom was available for single-photon production for 8 seconds on average.

In contrast, for whispering-gallery mode resonators, the peak value of the electric field is located inside the resonator material. Coupling of an atom to the microresonator mode is only possible via the evanescent field. The spatial decay of the coupling strength outside the resonator takes place on a length scale of few hundred nanometers. This is much smaller than the accuracy with which a single atom can be positioned by conventional optical methods. Therefore, up to now, only transits of atoms through the evanescent field were observed for WGM microresonators. In [Aok06], strong coupling between the mode of a microtoroidal resonator and a single Cs atom was observed. The transmission of a weak probe beam, critically coupled to the microresonator using an ultra-thin fiber coupler and resonant with the atomic transition, was monitored while releasing a cloud of 10^6 atoms from a MOT placed 10 mm above the resonator. Single atom transits through the evanescent field of the microtoroidal resonator showed up as a recovery of the probe transmission through the ultra-thin fiber. Atom transit times on the order of few microseconds have been observed. In [Ver97] a scheme of confining an

atom to a circular orbit in close proximity to a microsphere by using two modes, oppositely detuned from the atomic resonance frequency, is proposed. The red detuned light field creates an attractive potential, whereas the blue detuned light field compensates the vdW attraction close to the surface. Another promising method for placing an atom at a sufficiently small distance from the resonator surface is offered by ultra-thin fiber based dipole traps [Vet10]. In these devices, atoms are trapped in the evanescent field surrounding the fiber waist created by two pairs of counter-propagating beams, again oppositely detuned from the atomic resonance. The strong exponential spatial decay of the evanescent field which impedes the coupling of atoms to the light field of the microresonator, allows one to control the radial position of the atoms with outstanding accuracy in the case of the trap. Moreover, this trap is fully compatible with the bottle microresonator concept. The ultra-thin waist of the trapping fiber can be placed at one caustic of the resonator and can in addition be used to couple light into and out of the bottle mode used for the CQED experiment.

5.2.2 Coupling strength

The CQED parameters for bottle modes, as calculated above, align with FP microresonators and microtoroidal resonators. The performance of FP resonators is discussed exemplary for two cavities. In both works, the D2 transition of Cs was used. In [Hoo00] a cavity with a finesse of $\mathcal{F} = 4.8 \times 10^5$, corresponding to $Q = 1.2 \times 10^7$, and a length of 10.9 μm yields $(g_0, \kappa, \gamma_\perp) = 2\pi\cdot(110, 14.2, 2.6)$ MHz corresponding to $g^2/(\kappa\gamma_\perp) = 330$. For the cavity used in [Khu08] a finesse of $\mathcal{F} = 1 \times 10^6$, corresponding to $Q = 3.8 \times 10^8$, and a cavity length of 160 μm, result in parameters $(g_0, \kappa, \gamma_\perp) = 2\pi\cdot(13, 0.4, 2.6)$ MHz and $g^2/(\kappa\gamma_\perp) = 160$.

The microtoroidal resonator for which strong coupling was observed in the experiment described above had a diameter of 44 μm and a quality factor of $Q_{\mathrm{crit}} = 1.9 \times 10^7$ [Aok06]. The observed coupling parameters are $(g, \kappa, \gamma_\perp) = 2\pi\cdot(50\pm12, 17.9, 2.6)$ MHz, corresponding to $g^2/(\kappa\gamma_\perp) = 54$.

5.2.3 Tunability and frequency stability

As mentioned above, the modular design of FP resonators enables full tunability. The FP microresonator from [Khu08] consists of two mirrors separated by 160 μm. Changing the mirror separation by 0.5 μm using a piezoelectric actuator, results in a resonance frequency shift of 1.2 FSRs (1.1 THz). On the other hand, once the cavity is tuned to the atomic transition, the mirror separation has to be actively stabilized using the Pound-Drever-Hall (PDH) technique. Due to the high finesse of $\mathcal{F} = 1 \times 10^6$, the cavity length has to be controlled better than $\delta L = \lambda/(2\mathcal{F}) = 0.4$ pm in order to stabilize the cavities resonance frequency within its linewidth of 0.9 MHz ($Q = 3.8 \times 10^8$). In contrast, due to their monolithic design, WGM resonators exhibit an excellent passive frequency stability, but limited tunability. For the experiments with microtoroidal resonators in [Aok06], stabilization of the laser frequency by manually changing the resonator temperature using a Peltier element was sufficient in order to observe strong coupling of Cs atoms and

a mode with $\kappa = 2\pi \cdot 17.9$ MHz ($Q_{\mathrm{crit}} = 9.7 \times 10^6$). However, temperature tuning of the resonance frequency was only possible within a fraction of the FSR. Therefore, tuning of an UHQ mode to the atomic transition is not guaranteed. A resonator exhibiting an UHQ mode that lies close enough to the atomic transition has to be fabricated by trial and error. In contrast, for the bottle microresonator, it is possible to tune an UHQ mode to a predetermined frequency for every resonator fabricated using the tuning scheme presented in section 3.5.3. In fact, stabilization of a bottle mode with an ultra-high quality factor of $Q_{\mathrm{crit}} = 1 \times 10^8$ to the D2 transition of ^{85}Rb has already been demonstrated in our group [Osh10].

5.2.4 Coupling characteristics between the cavity and an external light field

A severe disadvantage of FP resonators is the poor efficiency with which light is coupled into and out of the cavity mode. Typical mirror transmissions t and absorption/scattering losses a are ($t = 4.5$ ppm, $a = 2$ ppm) [Hoo00] or ($t = 1.3$ ppm, $a = 1.8$ ppm) [Khu08]. This results in transmissions $T = t^2/(t + a)^2$ of $T = 0.48$ and $T = 0.18$. In contrast, the bottle microresonator can be operated in a regime in which the characteristic time constants for energy transfer between the coupling fibers are much smaller than the intracavity energy decay. In conjunction with the negligible losses introduced by the resonator–fiber coupling junction, this enables very efficient energy transfer between the bottle mode and the in- and output ports of the tapered fibers. The coupling between the input light field and the resonator mode (set to a fixed value by the mirror transmission t in the case of an FP) can flexibly be varied by adjusting the resonator fiber gap. At the critical coupling point, a complete transfer of the incident optical power to the resonator is possible. As demonstrated in chapter 4, the bottle microresonator in add-drop configuration is a four-port device with single-mode fiber in- and outputs. A power transfer efficiency of $E_{\mathrm{tot}} = 90\%$ between the input port of the bus fiber and the output port of drop fiber (including losses at the taper transitions) was demonstrated. At the same time, the loaded quality factor of $Q_{\mathrm{crit}} = 7.2 \times 10^6$ is high enough to maintain $g^2/\kappa\gamma_\perp \approx 40$.

5.3 CQED experiments using bottle microresonators – two examples

In order to complete this discussion, I want to point out two possible applications for the bottle microresonator in CQED experiments. In a so-called "single-atom beamsplitter", photons are routed between the output ports of a bottle microresonator in add-drop configuration, depending on the energy state of an atom located in its evanescent field. In another experiment, the anharmonicity of the ladder of eigenstates, as predicted by the Jaynes-Cummings model, is employed to generate nonlinearities at the single-photon level, which can be used to control the flow of light in a so-called "photon turnstile" device.
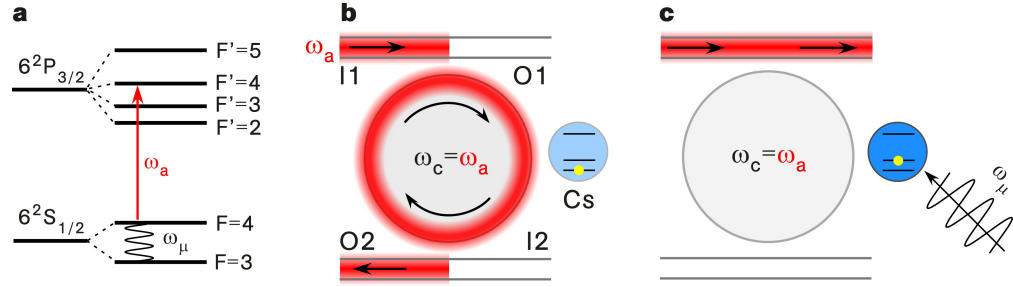
Figure 5.4: Schematic of the "single-atom beamsplitter". (a) Simplified energy level scheme of ^{133}Cs. The cesium atom can be switched between the $F = 3$ and $F = 4$ hyperfine ground states using microwave radiation at a frequency of $\omega_\mu = 2\pi \times 9.2$ GHz. Exposure of the atom, originally in the $F = 3$ state, to a resonant microwave π pulse, transfers the atom into the $F = 4$ state which then couples to a light field (red arrow) with frequency ω_a, resonant with the $(F = 4 \rightarrow F' = 4)$ transition. (b-c) A weak light field with frequency ω_a is coupled into one of the input ports (I1) of the bottle microresonator in add-drop configuration. The resonance frequency ω_c of the bottle mode is also stabilized to the frequency of the atomic transition ω_a. The possibility of on- and off-switching of the interaction between the bottle mode and the atom by a microwave pulse enables routing of the input light field between both fiber outputs (O1 and O2). (b) If the atom is in the $F = 3$ state, the coupling rate between the atom and the resonator mode is zero. In this case, the input light field is resonantly coupled to the resonator mode and is thus transferred to output O2. (c) As soon as the atom is excited to the $F = 4$ state, it strongly couples to the bottle mode. The resonance frequencies of the eigenmodes of the strongly coupled atom–cavity system are now detuned from ω_a, see Fig. 5.3 (b). The input light field can no longer enter the cavity and is transmitted through the bus fiber.

5.3.1 A single-atom beamsplitter

In Fig. 5.4, a single-atom beamsplitter is schematically shown. It consists of a single cesium atom, located in the evanescent field of a bottle microresonator in add-drop configuration. Its resonance frequency ω_c as well as the frequency of the fiber-guided light to be processed are locked to the atomic $(F = 4 \rightarrow F' = 4)$ transition. The atom-cavity coupling can be switched on and off by switching the atom between the $F = 3$ and the $F = 4$ hyperfine ground states using microwave pulses. This routes the photons between both output ports of the add-drop device. Applying a microwave $\pi/2$ pulse, the atom can be prepared in a superposition $1/\sqrt{2}(|F = 3\rangle + i\,|F = 4\rangle)$ of both states. This enables generation of entangled states, in which the atomic state and the propagation of a single photon are correlated. The same scheme will also work for weak coherent light pulses with Poissonian photon statistics, i.e., classical light fields. It should therefore be possible to generate entangled states in which the internal atomic state is correlated with the propagation of a classical light field. Such an entangled state in which a classical and a quantum mechanical parameter are correlated is of fundamental interests in the field of physics. According to the famous gedankenexperiment by Erwin Schrödinger these states are called Schrödinger cat states.
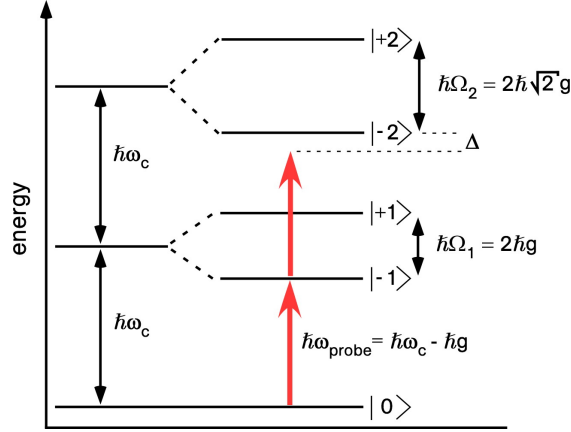
Figure 5.5: Ladder of eigenstates of a strongly coupled atom–cavity system, as predicted by the Jaynes-Cummings model in the case of $\omega_c = \omega_a = \omega$. The ground state corresponds to the bare atom-cavity system. By absorbing one/two photons the system is transferred to the first/second excited state. The Rabi splitting $\hbar\Omega_n = 2\hbar\sqrt{n}g$ of the excited states depends on the photon number n. In contrast to a bare cavity with a constant energy spacing of $\hbar\omega_c$ between adjacent modes, the energy levels of the coupled system exhibit distinct spacings, giving rise to single-photon nonlinearities. For a probe beam with frequency $\omega_{\text{probe}} = \omega_c - g$, absorption of one photon leads to a detuning of Δ from the next resonance of the coupled atom-cavity system.

5.3.2 Nonlinearities at the single-photon level

Finally, I want to come back to the field of nonlinear light-light interaction. In the case of strong coupling between the cavity and a single atom, it is possible to observe nonlinearities at the single-photon level. The nonlinearity in such a system is caused by the anharmonicity of the ladder of eigenstates as predicted by the Jaynes-Cummings model according to Eq. (5.5). This is illustrated in Fig. 5.5 for $\omega_c = \omega_a$. The equidistant spacing of the energy levels of the bare cavity is lifted in the case of strong coupling. The absorption of one photon, with energy $\hbar\omega_{\text{probe}} = \hbar\omega_c - \hbar g$, then results in a detuning of the systems resonance frequency with respect to ω_{probe}. This leads to a situation known as "photon blockade" [Bir05], in which a second photon can not enter the cavity. Such a system can be employed as a photon turnstile device. The flow of photons is regulated, because they can only pass the system one by one. In [Bir05], a light field of frequency $\omega_{\text{probe}} = \omega_c - g$ exhibiting Poissonian photon statistics was coupled to a Fabry-Pérot microresonator resonant with a single Cs atom. Sub-Poissonian photon statistics with pronounced anti-bunching were observed for the light field transmitted through the cavity. In [Day08] a similar change in the photon statistics of the light transmitted through an ultra-thin fiber, coupled to a microtoroidal resonator was observed during single-atom transits through the evanescent field of the resonator. In the case of a whispering-gallery mode resonator one has to take into account that the atom couples to both counter-propagating modes of the resonator. A full description of a single atom interacting with a fiber-coupled whispering-gallery mode resonator containing two

counter-propagating light fields is given in the Supplementary Information of [Aok06] and [Day08]. The bottle microresonators combines light-matter interaction in the strong coupling regime with operation in a highly efficient add-drop configuration and therefore offers is an interesting system to study the effects described above.

Bibliography

[Ada77] A. W. Adamson, *Physical chemistry of surfaces* (Wiley, New York, 1977).

[Arm03] D. K. Armani, T. J. Kippenberg, S. M. Spillane, and K. J. Vahala, "Ultra-high-Q toroid microcavity on a chip," Nature **421,** 925 (2003).

[Arm07] A. M. Armani, R. P. Kulkarni, S. E. Fraser, R. C. Flagan, and K. J. Vahala, "Label-free, single-molecule detection with optical microcavities," Science **317**, 783 (2007).

[Arm04] D. Armani, B. Min, A. Martin, and K. J. Vahala, "Electrical thermo-optic tuning of ultrahigh-Q microtoroid resonators," Appl. Phys. Lett. **85**, 5439 (2004).

[Asa06] T. Asano, B. S. Song, Y. Akahane, and S. Noda, "Ultrahigh-Q nanocavities in two-dimensional photonic crystal slabs," IEEE J. Sel. Top. Quantum Electron. **12,** 1123 (2006).

[Alm04a] V. R. Almeida and M. Lipson, "Optical bistability on a silicon chip," Opt. Lett. **29,** 2387 (2004).

[Alm04b] V. R. Almeida, C. A. Barrios, R. R. Panepucci and M. Lipson, "All-optical control of light on a silicon chip," Nature **431,** 1081 (2004).

[Aok06] T. Aoki, B. Dayan, E. Wilcut, W. P. Bowen, A. S. Parkins, T. J. Kippenberg, K. J. Vahala, and H. J. Kimble, "Observation of strong coupling between one atom and a monolithic microresonator," Nature **443,** 671 (2006).

[Ber94] P. R. Berman, *Cavity quantum electrodynamics* (Academic Press, Boston, 1994).

[Ber08] P. Bermel, A. Rodriguez, S. G. Johnson, J. D. Joannopoulos, and M. Soljačić, "Single-photon all-optical switching using waveguide-cavity quantum electrodynamics," Phys. Rev. A **74,** 043818 (2006).

[Bir92] T. A. Birks and Y. W. Li, "The shape of fiber tapers," J. Lightwave Technol. **10**, 432 (1992).

[Bir05] K. M. Birnbaum, A. Boca, R. Miller, A. D. Boozer, T. E. Northup, and H. J. Kimble, "Photon blockade in an optical cavity with one trapped atom," Nature **436,** 87 (2005).

[Boo07] A. D. Boozer, A. Boca, R. Miller, T. E. Northup, and H. J. Kimble, "Reversible state transfer between light and a single trapped atom," Phys. Rev. Lett. **98**, 193601 (2007).

Bibliography

[Boc04] A. Boca, R. Miller, K. M. Birnbaum, A. D. Boozer, J. McKeever, and H. J. Kimble, "Observation of the vacuum rabi spectrum for one trapped atom," Phys. Rev. Lett. **93,** 233603 (2004).

[Buc03] J. R. Buck and H. J. Kimble, "Optimal sizes of dielectric microspheres for cavity QED with strong coupling," Phys. Rev. A **67,** 033806 (2003).

[Bur90] T. M. Burkat, D. P. Dobychin, and L. G. Paltiel, Sov. Phys. Dokl. **310,** 376 (1990).

[Bra89] V. B. Braginsky, M. L. Gorodetsky, and V. S. Ilchenko, "Quality-factor and nonlinear properties of optical whispering-gallery modes," Phys. Lett. A **137,** 393 (1989).

[Bra04] G. Brambilla, V. Finazzi, and D. Richardson, "Ultra-low-loss optical fiber nanotapers," Opt. Express **12,** 2258 (2004).

[Cai00a] M. Cai, O. Painter, K. J. Vahala, and P. C. Sercel, "Fiber-coupled microsphere laser," Opt. Lett. **25,** 1430 (2000).

[Cai00b] M. Cai, O. Painter, and K. J. Vahala, "Observation of critical coupling in a fiber taper to a silica-microsphere whispering-gallery mode system," Phys. Rev. Lett. **85,** 74 (2000).

[Cha07] D. E. Chang, A. S. Sorensen, E. A. Demler, and M. D. Lukin, "A single-photon transistor using nanoscale surface plasmons," Nature Physics **3,** 807 (2007).

[Chu99] S. T. Chu, B. E. Little, W. Pan, T. Kaneko, S. Sato, and Y. Kokubun, "An eight-channel add-drop filter using vertically coupled microring resonators over a cross grid," IEEE Phot. Technol. Lett. **11,** 691 (1999).

[Car07] T. Carmon and K. J. Vahala, "Visible continuous emission from a silica microphotonic device by third-harmonic generation," Nature Physics **3,** 430 (2007).

[Car05] T. Carmon, T. Kippenberg, L. Yang, H. Rokhsari, S. Spillane, and K. Vahala, "Feedback control of ultra-high-Q microcavities: application to micro-Raman lasers and microparametric oscillators," Opt. Express **13,** 3558 (2005).

[Clo05] A. M. Clohessy, N. Healy, D. F. Murphy, and C. D. Hussey, "Short low-loss nanowire tapers on singlemode fibres," Electron. Lett. **41,** 954 (2005).

[Coh92] C. Cohen-Tannoudji, J. Dupont-Roc, and G. Grynberg, *Atom-photon interactions: Basic processes and applications* (Wiley, New York, 1992).

[Day08] B. Dayan, A. S. Parkins, T. Aoki, E. P. Ostby, K. J. Vahala, and H. J. Kimble, "A photon turnstile dynamically regulated by one atom," Science **319,** 1062 (2008).

[Dat92] V.V. Datsyuk,"Some characteristics of resonant electromagnetic modes in a dielectric sphere," Appl. Phys. B: Photophys. Laser Chem. **54,** 184 (1992).

108

[Djo02] K. Djordjev, S. J. Choi, and P. D. Dapkus, "Microdisk tunable resonant filters and switches," IEEE Phot. Technol. Lett. **14**, 828 (2002).

[Dot07] I. Dotsenko, "Single atoms on demand for cavity QED experiments," PhD thesis, Rheinische Friedrich-Wilhelms Universität, Bonn (2007).

[Dua04] L.-M. Duan and H. J. Kimble, "Scalable photonic quantum computation through cavity-assisted interactions," Phys. Rev. Lett. **92,** 127902 (2004).

[Dub95] N. Dubreuil, J. C. Knight, D. K. Leventhal, V. Sandoghdar, J. Hare, and V. Lefèvre, "Eroded monomode optical fiber for whispering-gallery mode excitation in fused-silica microspheres," Opt. Lett. **20,** 813 (1995).

[For07] K. M. Fortier, S. Y. Kim, M. J. Gibbons, P. Ahmadi and M. S. Chapman, "Deterministic loading of individual atoms to a high-finesse optical cavity," Phys. Rev. Lett. **98,** 233601 (2007).

[Ger98] J. M. Gérard, B. Sermage, B. Gayral, B. Legrand, E. Costard, and V. Thierry-Mieg, "Enhanced spontaneous emission by quantum boxes in a monolithic optical microcavity," Phys. Rev. Lett. **81,** 1110 (1998).

[Gor00] M. L. Gorodetsky, A. D. Pryamikov, and V. S. Ilchenko, "Rayleigh scattering in high-Q microspheres," J. Opt. Soc. Am. B **17,** 1051 (2000).

[Gor96] M. L. Gorodetsky, A. A. Savchenkov, and V. S. Ilchenko, "Ultimate Q of optical microsphere resonators," Opt. Lett. **21,** 453 (1996).

[Gla91] G. S. Glaesmann and D. J. Walther, "Method for obtaining long-length strength distributions for reliability prediction," Opt. Eng. **30**, 746 (1991).

[Hau84] H.A. Haus, *Waves and fields in optoelectronics* (Prentice-Hall, Englewood Cliffs, New Jersey, 1984).

[Har09] L.-D. Haret, T. Tanabe, E. Kuramochi, and M. Notomi, "Extremely low power optical bistability in silicon demonstrated using 1D photonic crystal nanocavity," Opt. Express **17,** 21108 (2009).

[Hay07] P. Del'Haye, A. Schliesser, O. Arcizet, T. Wilken, R. Holzwarth, and T. J. Kippenberg, "Optical frequency comb generation from a monolithic microresonator," Nature **450,** 1214 (2007).

[Hec89] E. Hecht, *Optik* (Addison-Wesley, Bonn, 1989).

[Hee08] J. Heebner, R.Grover and T. A. Ibrahim, *Optical microresonators: theory, fabrication, and applications* (Springer, New York, 2008).

[He93] J. He, M. Cada, M.-A. Dupertuis, D. Martin, F. Morier-Genoud, C. Rolland, and A. J. Spring-Thorpe, "All-optical bistable switching and signal regeneration in a semiconductor layered distributed-feedback/Fabry-Perot structure," Appl. Phys. Lett. **63,** 866 (1993).

Bibliography

[Hee04] J. E. Heebner, N. N. Lepeshkin, A. Schweinsberg, G. W. Wicks, R. W. Boyd, R. Grover, and P.-T. Ho,"Enhanced linear and nonlinear optical phase response of AlGaAs microring resonators," Opt. Lett. **29,** 769 (2004).

[Hij07] M. Hijlkema, B. Weber, H. P. Specht, S. C. Webster, A. Kuhn, and G. Rempe, "A single-photon server with just one atom," Nature Physics **3**, 253 (2007).

[Hoo00] C. J. Hood, T. W. Lynn, A. C. Doherty, A. S. Parkins, and H. J. Kimble, "The atom-cavity microscope: Single atoms bound in orbit by single photons," Science **287,** 1447 (2000).

[Ibr02] T. A. Ibrahim, V. Van, and P.-T. Ho, "All-optical time-division demultiplexing and spatial pulserouting with a GaAs/AlGaAs microring resonator," Opt. Lett. **27,** 803 (2002).

[Ibr03] T. A. Ibrahim, W. Cao, Y. Kim, J. Li, J. Goldhar, P.-T. Ho, and C. H. Lee, "All-optical switching in a laterally coupled microring resonator by carrier injection," IEEE Photonics Technol. Lett. **15,** 36 (2003).

[Ill92] V. S. Il'chenko, M. L. Gorodetskii, "Thermal nonlinear effects in optical whispering gallery microresonators," Laser Phys. **2,** 1004 (1992).

[Ill06] V. S. Ilchenko and A. B. Matsko, "Optical resonators with whispering-gallery-modes – part II: Applications," IEEE J. Sel. Top. Quantum Electron. **12,** 15 (2006).

[Kak01] G. Kakarantzas, T. E. Dimmick, T. A. Birks, R. Le Roux, and P. St. J. Russell, "Miniature all-fiber devices based on CO_2 laser microstructuring of tapered fibers," Opt. Lett. **26**, 1137 (2001).

[Kim93] D. Y. Kim, M. Sundheimer, A. Otomo, G. Stegeman, W. H. G. Horsthuis, and G. R. Mohlmann, "Third order nonlinearity of 4-dialkylamino-4'-nitro-stilbene waveguides at 1319 nm" Appl. Phys. Lett. **63,** 290 (1993).

[Kim08] H. J. Kimble, "The quantum internet," Nature **453,** 1023 (2008).

[Kip02] T. J. Kippenberg, S. M. Spillane, and K. J. Vahala, "Modal coupling in traveling-wave resonators," Opt. Lett. **27,** 1669 (2002).

[Kip04a] T. J. Kippenberg, S. M. Spillane, and K. J. Vahala, "Demonstration of ultra-high-Q small mode volume toroid microcavities on a chip," Appl. Phys. Lett. **85,** 6113 (2004).

[Kip04b] T. J. Kippenberg, "Nonlinear optics in ultra-high-Q whispering-gallery optical microcavities," PhD thesis, California Institute of Technology, Pasadena, California (2004).

[Kli00] W. Klitzing, E. Jahier, R. Long, F. Lissillour, V. Lefèvre-Seguin, J. Hare, J. M. Raimond, and S. Haroche, "Very low threshold green lasing in microspheres by up-conversion of IR photons," J. Opt. B: Quantum Semiclass. Opt. **2,** 204 (2000).

[Kli01] W. von Klitzing, R. Long, V. S. Ilchenko, J. Hare, and V. Lefèvre-Seguin, "Frequency tuning of the whispering-gallery modes of silica microspheres for cavity quantum electrodynamics and spectroscopy," Opt. Lett. **26**, 166 (2001).

[Kni97] J. C. Knight, G. Cheung, F. Jacques, and T. A. Birks, "Phase-matched excitation of whispering-gallery-mode resonances by a fiber taper," Opt. Lett. **22,** 1129 (1997).

[Bor68] N. F. Borrelli and R. A. Miller, "Determination of the individual strain-optic coefficients of glass by an ultrasonic technique," Applied Optics **7**, 745 (1968)

[Koy06] K. Koynov, A. Bahtiar, T. Ahn, R. M. Cordeiro, H. H. Hörhold, and C. Bubeck, "Molecular weight dependence of chain orientation and optical constants of thin films of the conjugated polymer MEH-PPV," Macromolecules **39,** 8692 (2006).

[Koy02] K. Koynov, N. Goutev, F. Fitrilawati, A. Bahtiar, A. Best, C. Bubeck, and H.-H. Hörhold, "Nonlinear prism coupling of waveguides of the conjugated polymer MEH-PPV and their figures of merit for all-optical switching," Opt. Soc. Am. B **19,** 895 (2002).

[Khu08] M. Khudaverdyan, W. Alt, I. Dotsenko, T. Kampschulte, K. Lenhard, A. Rauschenbeutel, S. Reick, K. Schörner, A. Widera, and D. Meschede, "Controlled insertion and retrieval of atoms coupled to a high-finesse optical resonator," New J. Phys. **10,** 073023 (2008).

[Lee02] K. S. Lee, *Polymers for photonics applictions* (Springer, New York, 2002).

[Len00] G. Lenz, J. Zimmermann, T. Katsufuji, M. E. Lines, H. Y. Hwang, S. Spälter, R. E. Slusher, S.-W. Cheong, J. S. Sanghera, and I. D. Aggarwal, "Large Kerr effect in bulk Se-based chalcogenide glasses," Opt. Lett. **25,** 254 (2000).

[Leo04] S. Leon-Saval, T. Birks, W. Wadsworth, and P. Russell, "Supercontinuum generation in submicron fibre waveguides," Opt. Express **12,** 2864 (2004).

[Lin91] C. Lin, *Handbook of microwave and optical components* (Wiley, New York, 1991).

[Lin10] G. Lin, B. Qian, F. Oručević, Y. Candela, J. B. Jager, Z. Cai, V.Lefèvre-Seguin, and J. Hare, "Excitation mapping of whispering gallery modes in silica microcavities," Opt. Lett. **35,** 583 (2010).

[Liu05] Q. Liu, X. Zhao, F. Gana, J. Mib and S. Qianb, "Ultrafast optical Kerr effect in amorphous $Ge_{10}As_{40}S_{30}Se_{20}$ film induced by ultrashort laser pulses," J. Optoelectron. Adv. Mater. **7,** 1323 (2005).

[Lov86] J. D. Love and W. M. Henry, "Quantifying loss minimisation in singlemode fibre tapers," Electron. Lett. **22,** 912 (1986).

[Lon03] R. Long, *Couplage d'une microsphère accordable et d'une "puce à atomes"*, PhD thesis, Université Paris VI (2003).

Bibliography

[Lou05] Y. Louyer, D. Meschede, and A. Rauschenbeutel, "Tunable whispering-gallery-mode resonators for cavity quantum electrodynamics," Phys. Rev. A **72,** 031801(R) (2005).

[McK04] J. McKeever, A. Boca, A. D. Boozer, R. Miller, J. R. Buck, A. Kuzmich, and H. J. Kimble, "Deterministic generation of single photons from one atom trapped in a cavity," Science **303**, 1992 (2004).

[Mab96] H. Mabuchi, Q. A. Turchette, M. S. Chapman, and H. J. Kimble, "Real-time detection of individual atoms falling through a high-finesse optical cavity," Opt. Lett. **21,** 1393 (1996).

[Mat06] A. B. Matsko and V. S. Ilchenko, "Optical resonators with whispering-gallery modes – part I: Basics," IEEE J. Sel. Top. Quant. **12**, 3 (2006).

[Mes04] D. Meschede, *Optics, Light and Lasers* (Wiley-VCH, Weinheim, 2004).

[Mic00] P. Michler, A. Kiraz, C. Becher, W. V. Schoenfeld, P. M. Petroff, L. Zhang, E. Hu, and A. Imamoglu, "A quantum dot single-photon turnstile device," Science **290**, 2282 (2000).

[Mur09] G. S. Murugan, J. S. Wilkinson, and M. N. Zervas, "Selective excitation of whispering gallery modes in a novel bottle microresonator," Opt. Express **17,** 11916 (2009).

[Not05] M. Notomi, A. Shinya, S. Mitsugi, G. Kira, E. Kuramochi, and T. Tanabe, "Optical bistable switching action of Si high-Q photonic-crystal nanocavities," Opt. Express **13,** 2678 (2005).

[Osh10] D. O'Shea, A. Rettenmaier, and A. Rauschenbeutel, "Active frequency stabilization of an ultra-high Q whispering-gallery-mode microresonator," Appl. Phys. B **99,** 623 (2010).

[Pai99] O. Painter, R. K. Lee, A. Scherer, A. Yariv, J. D. O'Brien, P. D. Dapkus, and I. Kim, "Two-dimensional photonic band-gap defect mode laser," Science **284,** 1819 (1999).

[Pel02] M. Pelton, C. Santori, J. Vucković, B. Zhang, G. S. Solomon, J. Plant, and Y. Yamamoto, "Efficient source of single photons: A single quantum dot in a micropost microcavity," Phys. Rev. Lett. **89,** 233602 (2002).

[Pey85] N. Peychambarian and H. M. Gibbs, "Optical nonlinearity, bistability, and signal processing in semiconductors," J. Opt. Soc. Am. B **2,** 1215 (1985).

[Poe06] M. Pöllinger, "Herstellung und spektrale Charakterisierung von abstimmbaren glasfaserbasierten Mikroresonatoren," Diplomarbeit, Rheinische Friedrich-Wilhelms Universität, Bonn (2006).

[Poe09] M. Pöllinger, D. O'Shea, F. Warken, and A. Rauschenbeutel, "Ultrahigh-Q tunable whispering-gallery-mode microresonator," Phys. Rev. Lett. **103,** 053901 (2009).

[Pur46] E. M. Purcell, "Spontaneous transition probabilities in radio-frequency spectroscopy," Phys. Rev. **69,** 681 (1946).

[Rem95] G. Rempe, "One-atom in an optical cavity - spatial-resolution beyond the standard diffraction limit," Appl. Phys. B **60,** 233 (1995).

[Ric04] R. E. Slusher, G. Lenz, J. Hodelin, J. Sanghera, L. B. Shaw, and I. D. Aggarwal, "Large Raman gain and nonlinear phase shifts in high-purity As_2Se_3 chalcogenide fibers," J. Opt. Soc. Am. B **21,** 1146 (2004).

[Rok04] H. Rokhsari and K.J. Vahala, "Ultralow loss, high Q, four port resonant couplers for quantum optics and photonics," Phys. Rev. Lett. **92,** 253905 (2004).

[Rok05] H. Rokhsari and K. J. Vahala, "Observation of Kerr nonlinearity in microcavities at room temperature," Opt. Lett. **30,** 427 (2005).

[Ros03] W. Rosenfeld, "A high finesse optical resonator for cavity QED experiments," Diplomarbeit, Rheinische Friedrich-Wilhelms Universität, Bonn (2003).

[San96] V. Sandoghdar, F. Treussart, J. Hare, V. Lefèvre-Seguin, J. M. Raimond, and S. Haroche, "Very low threshold whispering-gallery-mode microsphere laser," Phys. Rev. A **54,** R1777 (1996).

[Spi03] S. M. Spillane, T. J. Kippenberg, O. J. Painter, and K. J. Vahala, "Ideality in a fiber-taper-coupled microresonator system for application to cavity quantum electrodynamics," Phys. Rev. Lett. **91,** 043902 (2003).

[Spi05] S. M. Spillane, T. J. Kippenberg, K. J. Vahala, K. W. Goh, E. Wilcut, and H. J. Kimble, "Ultrahigh-Q toroidal microresonators for cavity quantum electrodynamics," Phys. Rev. A **71,** 013817 (2005).

[Sti09] A. Stiebeiner, O. Rehband, R. Garcia Fernandez, and A. Rauschenbeutel, "Ultrasensitive fluorescence spectroscopy of isolated surface-adsorbed molecules using an optical nanofiber," Opt. Express **17,** 21704 (2009).

[Ste98] D. A. Steck, "Cesium D line data," available online at http://steck.us/alkalidata (Los Alamos National Laboratory, Los Alamos, 1998).

[Str08] C. Strelow, H. Rehberg, C. M. Schultz, H. Welsch, C. Heyn, D. Heitmann, and T. Kipp, "Optical microcavities formed by semiconductor microtubes using a bottlelike geometry," Phys. Rev. Lett. **101**, 127403 (2008).

[Sum04] M. Sumetsky, "Whispering-gallery-bottle microcavities: The three-dimensional etalon," Opt. Lett. **29,** 8 (2004).

Bibliography

[Sum10b] M. Sumetsky, Y. Dulashko, and R. S. Windeler, "Super free spectral range tunable optical microbubble resonator," Opt. Lett. **35,** 1866 (2010),

[Sum10a] M. Sumetsky, Y. Dulashko, and R. S. Windeler, "Optical microbubble resonator," Opt. Lett. **35,** 898 (2010).

[Tan07] T. Tanabe, M. Notomi, E. Kuramochi, A. Shinya, and H. Taniyama, "Trapping and delaying photons for one nanosecond in an ultrasmall high-Q photonic-crystal nanocavity," Nature Photonics **1,** 49 (2007).

[Tap02] H. C. Tapalian, J.-P. Laine, and P. A. Lane, "Thermooptical switches using coated microsphere resonators," IEEE Photonics Technol. Lett. **14,** 1118 (2002).

[Tay96] A. J. Taylor, G. Rodriguez, and T. S. Clement , "Determination of n_2 by direct measurement of the optical phase," Opt. Lett. **21,** 1812 (1996).

[Ton03] L. Tong, R. R. Gattass, J. B. Ashcom, S. He, J.Lou, M. Shen, I. Maxwell, and E. Mazur, "Subwavelength-diameter silica wires for low-loss optical wave guiding," Nature **426,** 816 (2003).

[Tre98] F. Treussart, V. S. Ilchenko, J.-F. Roch, J. Hare, V. Lefèvre-Seguin, J.-M. Raimond, and S. Haroche, "Evidence for intrinsic Kerr bistability of high-Q microsphere resonators in superfluid helium," Eur. Phys. J. D **1,** 235 (1998).

[Vah03] K. J. Vahala, "Optical microcavities," Nature **424,** 839 (2003).

[Vah04] K. Vahala, *Optical microcavities* (World Scientific, Singapore, 2004).

[Van02] V. Van, T. A. Ibrahim, K. Ritter, P. P. Absil, F. G. Johnson, R. Grover, J. Goldhar, and P.-T. Ho, "All-optical nonlinear switching in GaAs-AlGaAs microring resonators," IEEE Photonics Technol. Lett. **14,** 74 (2002).

[Vet10] E. Vetsch, D. Reitz, G. Sagué, R. Schmidt, S. T. Dawkins, and A. Rauschenbeutel, "Optical interface created by laser-cooled atoms trapped in the evanescent field surrounding an optical nanofiber," Phys. Rev. Lett. **104,** 203603 (2010).

[Ver98a] D. W. Vernooy, V. S. Ilchenko, H. Mabuchi, E. W. Streed, and H. J. Kimble, "High-Q measurements of fused-silica microspheres in the near infrared," Opt. Lett. **23,** 247 (1998).

[Ver98b] D. W. Vernooy, A. Furusawa, N. Ph. Georgiades, V. S. Ilchenko, and H. J. Kimble, "Cavity QED with high-Q whispering gallery modes,"Phys. Rev. A **57,** R2293 (1998).

[Ver97] D. W. Vernooy and H. J. Kimble, "Quantum structure and dynamics for atom galleries," Phys. Rev. A **55,** 1239 (1997).

[War06] J. M. Ward, D. G. O'Shea, B. J. Shortt, M. J. Morrissey, K. Deasy, and S. G. Nic Chormaic, "Heat-and-pull rig for fiber taper fabrication," Rev. Sci. Inst. **77**, 083105 (2006).

[War07] F. Warken, "Ultradünne Glasfasern als Werkzeug zur Kopplung von Licht und Materie," PhD thesis, Rheinische Friedrich-Wilhelms Universität, Bonn (2007).

[War08] F. Warken, A. Rauschenbeutel, and T. Bartholomäus, "Fiber pulling profits from precise positioning," Photonics Spectra **42**, 3, 73 (2008).

[Wei07] E. Weidner, S. Combrié, A. de Rossi, N. Tran, and S. Cassette, "Nonlinear and bistable behavior of an ultrahigh-Q GaAs photonic crystal nanocavity," Appl. Phys. Lett. **90,** 101118 (2007).

[Wei06] E. Weidner, and S. Combrié, A. De Rossi, J. Nagle, S. Cassette, A. Talneau, and H. Benisty, "Achievement of ultrahigh quality factors in GaAs photonic crystal membrane nanocavity," Appl. Phys. Lett. **89,** 221104 (2006).

[Wil07] T. Wilk, S. C. Webster, A. Kuhn and G. Rempe, "Single-atom single-photon quantum interface," Science **317**, 488 (2007).

[Yar91] A. Yariv, *Optical electronics* (Saunders College Publishing, Philadelphia, 1991).

[Yos04] T. Yoshie, A. Scherer, J. Hendrickson, G. Khitrova, H. M. Gibbs, G. Rupper, C. Ell, O. B. Shchekin, and D. G. Deppe, "Vacuum Rabi splitting with a single quantum dot in a photonic crystal nanocavity," Nature (London) **432,** 200 (2004).